ACTIVE AND NONLINEAR NANOPHOTONICS FACILITATED BY HOT-CARRIER DYNAMICS

A Dissertation
Presented to
The Academic Faculty

by

Mohammad Taghinejad

In Partial Fulfillment
of the Requirements for the Degree
Doctor of Philosophy in the
School of Electrical and Computer Engineering

Georgia Institute of Technology
December 2020

ACTIVE AND NONLINEAR NANOPHOTONICS FACILITATED BY HOT-CARRIER DYNAMICS

Approved by:

Dr. Wenshan Cai, Advisor
School of Electrical & Computer Engineering
Georgia Institute of Technology

Dr. Tianquan Lian
Department of Chemistry
Emory University

Dr. Ali Adibi
School of Electrical & Computer Engineering
Georgia Institute of Technology

Dr. Benjamin D. B. Klein
School of Electrical & Computer Engineering
Georgia Institute of Technology

Dr. Eric M. Vogel
School of Materials Science & Engineering
Georgia Institute of Technology

Date Approved: August 18, 2020

To my Mom and Dad, the true heroes of my life,

and my lovely Siblings, my amazing best friends.

ACKNOWLEDGEMENTS

First of all, I would like to thank my advisor Prof. Wenshan Cai for his great support and guidance throughout my PhD study at Georgia Tech. I am grateful to him for giving me the freedom to pursue a line of research that best fits my interests, and being patient at the early stages of my PhD program while we were trying to establish basics of ultrafast nonlinear optics that was, at the time, a new field to all of us. His continued trust in my research, persistence in sharing his vast knowledge of optics with me, and valuable guidance gave me the strength and courage to invest my PhD on a high-risk and challenging research path. For that I am deeply thankful. The nice memories of many technical and nontechnical discussions that we had in his office and in the lab will always remain with me. Many thanks to my thesis committee members Dr. Ali Adibi, Dr. Eric M. Vogel, Dr. Benjamin D. B. Klein, and Dr. Tianquan Lian. I have been fortunate to have long lasting, fruitful, and productive collaborations with Dr. Adibi's group and have had the opportunity to engage in their exciting projects on the opto-electronic applications of 2D heterostructures based on transition metals dichalcogenides. In addition, I would like to specially thank Dr. Lian for generously accommodating my ultrafast optical measurements in his lab at Emory University. During our productive collaborations, I had the privilege of having many fruitful discussions with Dr. Lian and had the opportunity to closely work with talented researchers in his team, particularly with my friend Dr. Zihao Xu. Zihao is talented expert in optical measurements.

I am very grateful of the support and assistance from my past and present groupmates Kyutae Lee, Dr. Sean P. Rodrigues, and Dr. Shoufeng Lan. I am very

impressed by and grateful for the multipotentiality and diverse engineering skills of Kyutae who always come up with a solution to tackle issues that unexpectedly pop up during measurements. The help and friendship of all my groupmates made it possible for me to go through the difficulties I faced during my PhD. I also wish all the best for a successful PhD career to my other groupmates Andrew Kim, Zhaocheng Liu, Lakshmi Raju, and Dayu Zhu. My special thanks to Dr. Hesam Moradinejad who shared with me his valuable fabrication knowledge and offered his unique skills to help me in my research and beyond that guiding me to quickly adopt myself with the new life environment. Looking back at my time at Georgia Tech, I feel fortunate to meet and interact with Dr. Reza Eftekhar. He is without any doubt one of the smartest and most capable scientists I have met in person. I very much enjoyed my friendship with Dr. Amir Darabi, Dr. Amirabbas Pirouz, Dr. Amir Hossein Hosseinnia, Sajjad Abdollahramezani, and Omid Hemmatyar during my PhD life in Atlanta. I would like to specially thank the members of the institute for electronics and nanotechnology (IEN) and material characterization facilities (MFC) here at Georgia Tech. I received a great support from the fantastic engineers and scientists who managed to prepare a vibrant research environment for the fabrication and characterization of my devices. I would like to especially thank Mr. Gary Spinner and Mr. Walter Henderson whose leaderships have turned IEN and MCF into outstanding places for conducting state-of-the art research. Many thanks to Eric Woods who helped me a lot in the MCF center. I would also like to thank the supports of Devin K. Brown, Todd Walters, Chris Yang, Charlie Suh, Charlie Turgeon, Dean C. Sutter, Scott Fowler, Alex Gallmon, Tran-Vinh Nguyen, Rebhadevi Monikandan, Mikkel Thomas, Andrew Watkins, Brian Doles, and Richard Shafer. I am genuinely impressed by the level of knowledge and skills that this

amazing group of experts put together to enable cutting-edge research on the Georgia Tech campus.

It has been 2294 days since the last time I met my Family until this very moment that I am writing these last, most difficult, and most precious lines of my PhD thesis. Ever since, not even a single day has passed by me without missing them. All these years I have been asking myself whether I made a right decision to leave them, but I still do not know the answer; I even do not know what kind of a personal or professional achievement would convince me that my decision was at least not wrong. I guess I will have to think a few more years to find a convincing answer, if there is any at all! I consider *not knowing* the answer as a gift that gives me a strong motivation to make myself a man of more value in the years to come. The outmost level of gratitude goes to my Family, for their unconditional love and support, for their countless sacrifices, and above all, for being the best Family I could ever ask for. My Parents are the dearest and nearest to my heart and I owe them everything I have, big or small. Finally, my very especial thanks to my first and best friend, classmate, colleague, mentor, advisor, competitor, and Brother Dr. Hossein Taghinejad. We have walked through our lives together each and every single step, throughout the happy and sad moments. We grew together, fought our challenges together, and we will achieve our great goals together. Hossein is the smartest and most talented person I have ever seen. Knowing that I have the unconditional support of such a great friend and scientist, has been the greatest privilege of my life. In my research and professional activities, I have always tried my best to achieve the bests, but I have never prayed for my success. I have the best Family, no matter whether I succeed or not, I am always happy. For that, I am always grateful and consider myself the luckiest man in the world.

TABLE OF CONTENTS

LIST OF FIGURES

LIST OF SYMBOLS AND ABBREVIATIONS

LPR	Localized Plasmon Resonance
AOI	Angle of Incidence
SEM	Scanning Electron Microscopy
NA	Numerical Aperture
IE	Intensity Enhancement
LC	Liquid Crystal
NIR	Near Infrared
SHG	Second-Harmonic Generation
TMD	Transition Metal Dichalcogenide
2D	Two-Dimensional
DOS	Density of State
DC	Direct Current
TPA	Two Photon Absorption
FOM	Figure of Merit
PhC	Photonic Crystal
ENZ	Epsilon Near Zero
TCO	Transparent Conductive Oxide
ITO	Indium Tin Oxide
PC	Plasmonic Crystal
FP	Fabry Perot
TM	Transverse Magnetic
TE	Transverse Electric

SUMMARY

The ever-increasing demand for bandwidth scalability and high-speed operation is the driving force for the discovery of ultrafast switches. As electronics approaches its intrinsic limitations, pursuing new computational paradigms for data processing is inevitable. In recent years, optical computing –replacing electrons with photons– has been introduced as a powerful alternative to boost computational capacities beyond that of solid-state electronics. Up to date, however, the primary role of optical technologies in data processors has been limited to the realization of communication links between electronic blocks, often through the incorporation of optical fibers and, more recently, photonic waveguides. Although "speed" is the biggest promise of optics, relying on electronic components to control light sources at input/output (I/O) end-facets is the major setback towards unlocking ultimate potentials of optical data processors. To extend the role of optics beyond ultrafast data transmission links, it is essential to implement optical switches within CMOS-integrable platforms. This goal is achievable through nonlinear optical effects. Indeed, by enabling active modulation of light waves and on-demand generation of new spectral components, nonlinear optics potentially has the capability to deliver advanced optical I/O segments with operation speeds well beyond the capabilities of electronic devices.

This PhD thesis is focused on the exploration of new techniques for the implementation of ultrafast all-optical switches. During my PhD program at Georgia Tech, I did my best to pursue this goal at two equally important levels: (*i*) material-design level; and (*ii*) device-design level. It comes without saying that understanding the properties of

active optical materials is a prerequisite of the device-level design too, as the intrinsic material properties obviously impact both linear and nonlinear responses of any photonic structure. In addition, empowered by the Maxwell's description of light-matter interactions, predicting the performance of a nanophotonic platform at a device level is theoretically manageable, and most often very close to our in-lab observations. In sharp contrast, predicting properties of materials, especially in their out-of-equilibrium states, is numerically a very challenging task. Therefore, my research primarily aimed at "experimental" study of material properties to gain deep insights on the transient behavior of charge carriers in optical media. I believe that such knowledge provides numerically out-of-reach information regarding the capabilities of optical materials, required for the design of all-optical switches. I have provided some critical discussion regarding the design of prototypical nanophotonic structures as well, to guide the readers of this document towards necessary steps that should be taken for the successful design of optical switches from a device-level perspective.

In the first half of this thesis, I propose and experimentally demonstrate that the semi-instantaneous transport of plasmonic hot electrons in hybrid metal/dielectric systems enables coherent control over the third-order nonlinear properties of noble metals. By relying on the ultrafast dynamic of hot-electron transport, we design prototypical plasmonic structures that can benefit from the inherently fast nature of the electron transport and therefore, facilitate the sub-picosecond all-optical switching of intensity, phase, and polarization of light. In the second half, we further expand the contribution of plasmonic hot carriers in the field of active and nonlinear nanophotonics and propose a fundamentally new paradigm for inducing optical nonlinearities of second-order type in

centrosymmetric materials upon the transport of hot electrons. Our proposed method, allows for optically breaking the inversion symmetry in a wide range of optical materials, expanding the portfolio of second-order nonlinear media that could be adopted for the realization of functional nanophotonic devices. I believe our demonstrations and experimental observations reveal significant potentials of plasmonic hot carriers in the field of nonlinear nanophotonics and at the same time introduces a new problem set for physicists at the crossroads of nonlinear optics, hot-carrier physics, and nanophotonics.

CHAPTER 1. INTRODUCTION

Optical modulation is one of the most fascinating directions in the modern photonics technology that offers a new paradigm for high-speed data processing, potentially beyond the limitations of electronics. The goal to modulate light can be primarily pursued by relying on the intrinsic response of active materials whose optical properties are tunable via external stimuli in an electrical, thermal, mechanical, or all-optical manner. In this context, tuning the complex index of refraction ($\tilde{n}$) plays a key role because $\tilde{n}$ significantly influences the intensity, phase, and polarization of light upon light-matter interactions. However, the achievable refractive index change ($\Delta\tilde{n}$) in most active materials usually does not show a linear relation with the strength of the external stimuli and is often limited to a small change that prevents the effective modulation of light properties. To tackle this issue, the incorporation of active materials in optical However, the achievable refractive index change ($\Delta\tilde{n}$) in most active materials usually does not show a linear relation with the strength of the external stimuli and is often limited to a small change that prevents the effective modulation of light properties. To tackle this issue, the incorporation of active materials in optical cavities is a promising approach that besides boosting the depth of modulation allows for the independent control over the intensity, phase, and polarization of light by designing the resonance properties of cavities. Therefore, in this perspective we limit the scope our discussion to cavity-based modulation schemes.

Cavity-based optical modulators are often comprised of two principal sections: (i) a resonator that controls the intensity, phase, or polarization of an information-carrying optical signal; and (ii) a control unit that modifies the resonant properties of the resonator

via inducing a reversible change in the refractive index of the cavity medium. As a representative example, Figure 1a schematically depicts the working principle of a transmissive intensity modulator when the input signal (at ω_s) is on resonance with the optical cavity mode (at ω_c). In this scheme, most of the input signal is trapped inside the resonant cavity, leading to a weak signal intensity at the output port of the modulator, a condition that we consider as the *off* state. An external stimulus from the control unit can induce a $\Delta\tilde{n}$ to disturb the resonance condition inside the cavity, leading to the buildup of the light intensity at the output port and eventually switching the modulator to the *on* state. The control unit usually applies optical, electrical, thermal, or mechanical signals to modify $\tilde{n}$ through modulating the carrier density, the stored thermal energy, or the length of interatomic bonds in designated elements inside the resonator. Based on this simplified description, we can readily conclude that the characteristics of employed cavities together with the intrinsic properties of incorporated materials define the performance of optical modulators. As the performance criteria, modulators are often characterized based on their modulation depth (i.e., *on*-to-*off* signal ratio), modulation speed (i.e., switching speed between the two states), and the power consumption per modulation events. Optimizing these parameters primarily requires a deep insight into the nature of physical effects that govern the tuning of the refractive index in various materials and a subsequent understanding of the interplay between these physical phenomena and resonant properties of optical cavities.

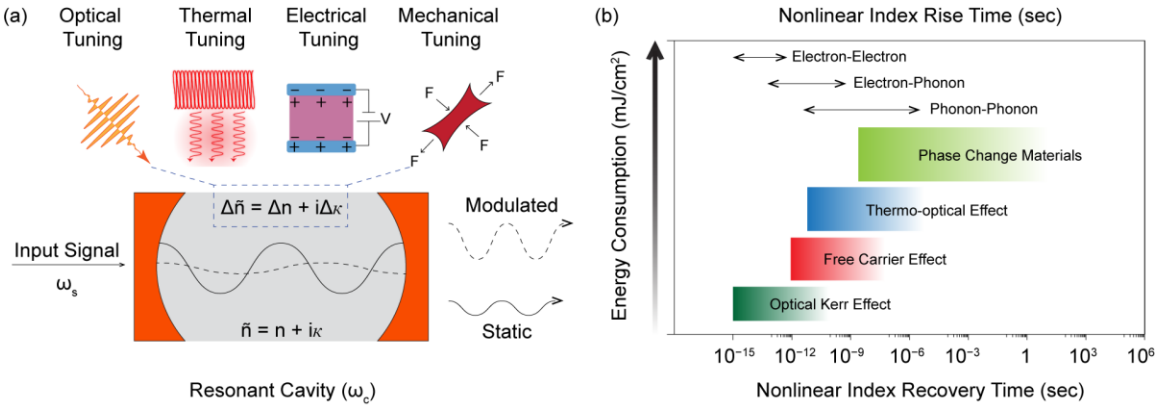

Figure 1: Operation mechanism of cavity-based optical modulators. (a) Schematic representation of a transmissive modulator when the information-containing input signal in on-resonance with the cavity mode. Before the application of a control signal, the input light is trapped inside the cavity which denotes the off-state at the output port of the modulator. Transitioning to the on-state occurs by altering the resonance lineshape of the cavity mode through the refractive index modulation upon the application of a control signal. (b) Characteristic timescale and required energy consumption for various optical effects that enable the tuning of refractive index.

As we stated above, optical modulation techniques rely on induced refractive-index changes in the constituting materials of resonant cavities. The strength and temporal duration (i.e., the relaxation time) of the induced $\Delta\tilde{n}$ are the most impactful material-dependent parameters that should be considered for the design and implementation of optical modulators. Indeed, the former is directly related to the modulation depth and the power consumption, and the latter primarily determines the modulation speed. Among various modulation schemes such as electro-optical,(1-3) thermo-optical,(4-6) mechano-optical,(7-9) and all-optical modulation, the last approach enables the fastest modulation speed and offers a large modulation depth for low-energy modulation needs. In terms of specifications, electro-optical modulators are the major opponent of all-optical modulators. Although electro-optical modulators are renowned for their notable modulation depth, they suffer from a fundamental tradeoff between speed and the *on*-to-*off* switching ratio. In fact,

in such structures to enhance the switching ratio it is necessary to increase the gating capacitance of the device while such an increase unfavorably lowers the modulation speed, as a universal weakness of capacitive active devices. The absence of this quasi-inherent tradeoff in all-optical modulators is the primary motive behind the current surge of research on the implementation of all-optical switches using micro- to nano-photonic platforms. However, the promising fast modulation speed in all-optical techniques should not be taken for granted. In fact, the optical excitation of the cavity medium simultaneously triggers multiple competing mechanisms with ultrafast, fast, and slow dynamics (Figure 1b), which makes the device performance very much dependent on the energy and wavelength of the stimulating control light as well as the inherent material properties of the cavity medium. In addition, the resonance properties of optical cavities such as the mode volume (V), the quality factor (Q), and the resonance wavelength (ω_c) directly influence the performance of modulators, independent of material responses (as will be discussed later). Therefore, understanding the temporal and spectral nature of optically excited processes in optical materials, inside and outside micro- and nano-scale cavities, seems to be necessary to unlock the ultimate potentials of all-optical modulators.

This chapter is organized to provide a microscopic insight on various light-induced transient effects that contribute to the modulation of the refractive index in dielectrics (including semiconductors), metals, and epsilon-near-zero solid media as major constituting materials for the realization of optical cavities. By contrasting their modulation characteristics and relaxation behaviors, we then focus on practical methods in which light-induced transient effects can enable the all-optical control of light properties in photonic and plasmonic cavities. Eventually, we will review the state-of-the-art demonstrations and

by describing existing challenges and shortcomings, we discuss possible future directions to advance this fast-evolving research area. In this perspective, we limit the scope of our discussions to the transient processes that enable fast tuning of the refractive index and can be enabled more efficiently under optical excitations. Therefore, for the details of processes such as free-carrier, thermo-optical, and material phase conversion effects we refer readers to more dedicated articles. (2, 10)

1.1 Background: Light-Matter Interactions

Under strong optical excitations, linear and nonlinear light-matter interactions contribute to the effective tuning of the refractive index. In isotropic media, such interactions are described using the relation between the induced dielectric polarization P and the optical electric field E_ω:

$$P = \varepsilon_0\left[\chi^{(1)}E_\omega + \chi^{(2)}E_\omega E_\omega + \chi^{(3)}E_\omega E_\omega E_\omega + \cdots\right] \qquad (1)$$

where ε_0 and $\chi^{(n)}$ are the vacuum permittivity and the nth-order dielectric susceptibility. The first term in *Eq. (1)* determines the index of refraction as $\tilde{n}_L^2 = (n_0 + i\kappa_0)^2 = 1 + \chi^{(1)}$, which governs linear processes typically involving single-photon interactions, whereas the higher-order terms describe nonlinear processes involving multi-photon interactions. An effective cavity-based modulation scheme often pursues the control of refractive index through either the linear term or those nonlinear terms that enable a notable $\Delta\tilde{n}$ at the spectral vicinity of ω_c. Indeed, optical processes that cause frequency conversion are often not effective because they fail to yield an additional contribution to the linear dielectric polarizability of materials, upon the interaction of multiple photons through

nonlinear susceptibilities. For instance, second-order optical nonlinearities only yield polarization components at zero or 2ω frequencies, unless we exploit a DC electric field to generate a component at ω and achieve refractive index modulation based on the electro-optic effect,(1-3) which is not compatible with all-optical techniques. In contrast, linear (i.e., $\chi^{(1)}$) and third-order (i.e., $\chi^{(3)}$) nonlinear processes facilitate the refractive index tuning in an all-optical fashion by preventing frequency conversion, as will be discussed throughout this Perspective. Moreover, it is important to notice that *Eq. (1)* in its general form imparts only a simplified macroscopic narration of light-matter interactions because the details of these interactions are mostly squeezed into effective dielectric susceptibilities. Thus, a microscopic description is also necessary to gain a comprehensive insight into the essence of such optical processes as well as the performance measures of all-optical modulators. For instance, the strength of the optically-induced $\Delta\tilde{n}$, which defines the modulation depth, can be primarily captured via dielectric susceptibilities of materials, but the modulation speed depends on the characteristic recovery time of the refractive-index change (Figure 1b), which needs to be examined, for instance, through the temporal evolution of electron states in active materials. Therefore, in next sections by introducing the basics of key physical and optical effects from macroscopic and microscopic points of view, we provide a succinct description of primary techniques for implementing all-optical modulation in photonics and plasmonic structures.

1.2 Dielectric Materials and Cavities

The promising optical functionalities that dielectric cavities have to offer, combined with the CMOS compatibility of many widely adopted dielectrics, as represented by

silicon, have triggered a surge of research on reversible processes in a broad spectrum of dielectric materials for the implementation of functional optical components.(2, 11-15) In dielectrics, two-photon absorption (TPA) is one of the predominant third-order nonlinear mechanisms through which refractive-index modulation is sufficiently strong. Figure 2a illustrates various types of TPA for the case of a representative indirect band gap dielectric such as silicon. In degenerate TPA as shown in Figure 2a (i), the phonon-assisted absorption of two photons of the signal light ($\hbar\omega_s$) enables the generation of electrons in the conduction band. The nonlinear transition of electrons induces a change in the imaginary part of the refractive index $\Delta\kappa = \beta_2 I_s = \frac{3\pi}{c\epsilon_0 n_0^2 \lambda} \mathrm{Im}\{\chi^{(3)}(\omega_s; \omega_s, -\omega_s, \omega_s)\} I_s$, which is proportional to the characteristic TPA coefficient (β_2) of the dielectric.(16-18) Based on the Kramer-Kronig relation, originating from the causality of physical systems, the induced $\Delta\kappa$ is always accompanied with a change in the real part of the refractive index $\Delta n = n_2 I_s = \frac{3}{4c\epsilon_0 n_0^2} \mathrm{Re}\{\chi^{(3)}(\omega_s; \omega_s, -\omega_s, \omega_s)\} I_s$, an effect associated with optical Kerr nonlinearity that is characterized using the Kerr coefficient n_2.(16-18) The overall complex index modulation $\Delta\tilde{n} = \left(n_2 + i\frac{\lambda}{4\pi}\beta_2\right) I_s$ is linearly dependent on the intensity of light and $\chi^{(3)}$ of the constituent materials of optical cavities. Figure 2b,c shows two representative demonstrations of all-optical modulation in silicon photonic devices such as waveguides and micro-resonators based on the Kerr and TPA effects.(19-22) In these structures, the intensity-dependent tuning of the refractive index modifies the spectral properties of resonance or guiding modes, and thusly facilitates the self-modulation of the light transmission through the designed structures by bringing the input signal in or out of resonance with photonic modes.(20, 22) The effective implementation of self-modulation

methods requires either employing a strong signal light or providing a long interaction footprint to sufficiently alter the interaction of light with photonic devices. However, when dealing with a weak information-carrying light, usually a strong control beam (ω_{co}) controls the index of refraction either in a degenerate fashion (Figure 2a-ii) or non-degenerately (Figure 2a-iii) via its nonlinear interaction with the input signal.(19, 23) The achievable index change through non-degenerate methods is twice as large as that of degenerate ones since in the non-degenerate approach we rely on the multiphoton interaction of two optical beams.

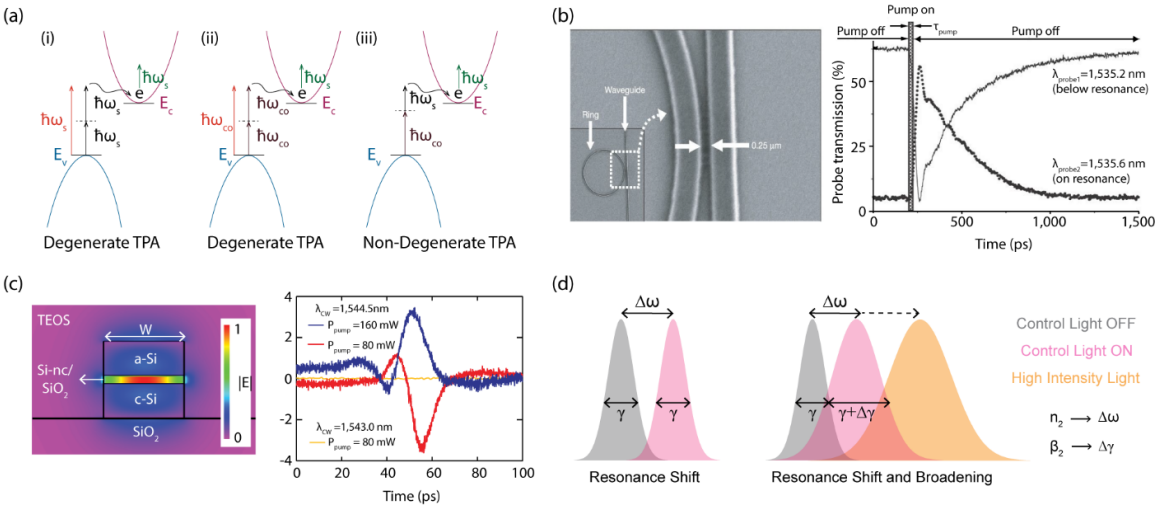

Figure 2: All-optical control of light in microscale photonic devices. (a) Schematic representation of various two-photon absorption processes in a representative indirect band gap dielectric. The green arrows show the intraband transition of free conduction electrons enabled by the absorption of signal photons. (b) All-optical modulation in a silicon micro-ring resonator at the telecommunication wavelength in a non-degenerate fashion, dominated by the TPA effect. (c) On-chip all-optical control of light propagation in a silicon slot waveguide, facilitated by the Kerr nonlinearity of silicon nanocrystals. Effects of Kerr and TPA on modulation properties. (d) An idea modulation scheme primarily relies on a resonance shift that originates from the Kerr effect (left panel). Since the TPA effect is usually entangled with the Kerr effect, the modulated resonance lineshape experiences a spectral broadening (right panel) that lowers the modulation depth.

Therefore, to achieve an envisioned modulation depth, a larger resonance shift is necessary by consuming more energy.

To obtain a notable on-to-off switching ratio upon the consumption of reasonably low energy, a compelling modulation scheme primarily relies on the resonance shift of cavity modes, as schematically shown in Figure 2d. However, in dielectric cavities this is usually not the case since the TPA effect acts to increase the light absorption so that the resonance shift, induced by the Kerr effect, is entangled with a spectral broadening effect and consequently a weakened switching ratio (Figure 2d). Therefore, to meet an envisioned switching ratio we need to spectrally shift the resonance mode further away from the steady state condition by consuming more energy, a fact that is not desired for highly demanded low-energy industrial needs. Moreover, the TPA effect enables free-carrier dispersion and absorption processes through the intraband transition of generated electrons in the conduction band, upon the absorption of the signal light (green arrows in Figure 2a). Such an unscheduled contribution of free carriers in the refractive index tuning, however, limits the modulation speed to the slow recombination rate of electron-hole pairs with a characteristic time scale that ranges from hundreds of picoseconds to several nanoseconds.(19, 23) Heat generation is another major drawback of the TPA involvement in the modulation of the refractive index.(16, 24) In fact, since the TPA effect enables real electronic transitions the electronic band (E_g), the absorbed energy of two photons will eventually turn into heat and consequently introduces another slowly decaying route to the refractive index manipulation.

Varieties of constraints that TPA imposes on the performance of all-optical modulators indicate the importance of device optimization through the right choice of

material as well as the operating wavelength, to diminish the unwanted side-effects of TPA in refractive index tuning. Along this venue, a figure-of-merit (FOM) defined as $n_2(\beta_2\lambda)^{-1}$ is often used to evaluate the relative strength and dispersion of nonlinear coefficients.(17, 23) Achieving a large FOM is indeed an indication of the minimized TPA impact on refractive index modulation. At the telecommunication wavelength of 1.55 μm, although silicon offers a significant Kerr nonlinearity, $n_2 \approx 4\times10^{-14}$ to 9×10^{-14} cm^2W^{-1},(25, 26) the existence of a strong TPA response, $\beta_2 \approx 5\times10^{-10}$ to 9×10^{-10} cmW^{-1},(27-30) leads to a low FOM of ~ 0.3 – 0.5. In silicon FOM can be improved by operating at a control wavelength beyond 1.55 μm, since the TPA effect starts to diminish beyond 2 μm, as we approach the $E_g/2$ threshold, and the Kerr coefficient peaks at ~ 1.8 – 1.9 μm.(17, 18) Such a dispersive behavior is observed in other dielectrics, however, the wavelength dependency needs to be modified according to their electronic band structures. Under the restriction of interband two-photon processes, numerical analyses suggest $n_2 \sim \left(n_0 E_g^4\right)^{-1}$ and $\beta_2 \sim \left(n_0^2 E_g^3\right)^{-1}$ as scaling rules based on which we can predict the qualitative variation of nonlinear coefficients among various dielectrics.(12, 31-34)

Minimizing the energy consumption in all-optical modulators expedites transitioning from the fundamental science to the practical realm. In cavity-based modulators, the required energy (U) to induce a significant resonance shift is inversely proportional to the ratio of the quality factor (Q) and mode volume (V) of the optical cavity, $U \sim (Q/V)^{-1}$. Indeed, maximizing Q/V in optical cavities is one of the important design criteria that has been sought after in various approaches. Photonic microcavities pursue this goal by increasing the device Q-factor (Figure 3a), an approach that simultaneously increases the required time to establish stable cavity oscillations (i.e., an increased cavity photon lifetime

τ_{cav}). For instance, in a micro-resonator with a Q-factor of 10^5, it takes about 80 picoseconds to re-stablish a steady cavity mode at 1.55 μm, a fact that limits the modulation speed despite the intrinsic temporal response of utilized materials. To circumvent this limitation, in an alternative approach it is possible to keep the Q-factor low and instead maximize Q/V by exerting spatial confinements on the mode volume through the design of nanocavities (Figure 3a). For this purpose, photonic crystals (PhCs), capable of providing a small volume, have been frequently exploited for the demonstration of low-power and fast optical modulators (Figure 3b), based on the Kerr and TPA effects.(35-37) More recently, by employing dielectrics with high indices of refraction (e.g., silicon and GaAs), nanocavities that support magnetic and electric Mie resonances with subwavelength mode volumes have been realized in a wide spectral range.(38-41) As depicted in Figure 3c, the initial surge of research on the Mie-based active devices made of silicon has revealed the significant impact of magnetic hot-spots on the enhancement of material nonlinearities as well as enabling the ultrafast (i.e., sub-picosecond) modulation regime based on dielectric materials.(38)

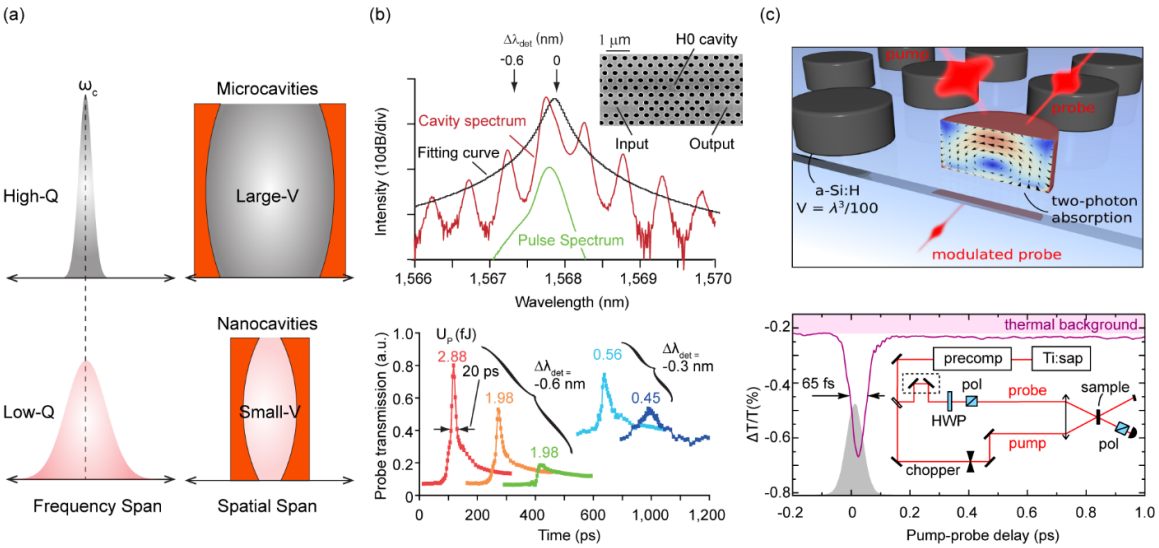

Figure 3: Ultrafast all-optical modulation in nanoscale photonic cavities. (a) Optimizing Q/V in micro- and nano-cavities. The enhancement of the Q-factor in microcavities and the suppression of the mode volume in nanocavities lead to enhanced Q/V ratio, thereby lowering the energy consumption. (b) Femtosecond modulation of light intensity in a photonic crystal nanoresonator at the telecommunication wavelength range. Spectral and transient responses of the device are shown in top and bottom panels, respectively. (c) Employing magnetic Mie resonance to manipulate light-mater interactions in nanoscale. Top and bottom panels depict the schematic of the utilized structure and the temporal response of the achieved intensity modulation. Panel (b) is reprinted with permission from reference (35). Panel (c) is reprinted with permission from reference (38), Copyright 2015 American Chemical Society.

Besides indirect bandgap dielectrics, primarily represented by silicon, the importance of direct bandgap semiconductors such as ZnSe, CdS, GaAs, and InGaAsP has steadily increased, since they offer stronger optical nonlinearities than their indirect-bandgap counterparts by about an order of magnitude.(35, 41-44) Direct bandgap materials allow releasing the constraint on the momentum conservation via the absorption or emission of phonons, and therefore enabling the effective enhancement of multiphoton electronic transitions to achieve stronger nonlinear responses. In addition, contrary to the indirect bandgap dielectrics that possess a positive Kerr coefficient across their transparent spectral

region (i.e., $\hbar\omega < E_g$),(31) in direct gap materials the zero-crossing of the Kerr coefficient happens at photon energies lower than their bandgap.(32) Therefore, beyond the zero-crossing point, the contributions of Kerr nonlinearity and free carrier effect on the index modulation are consolidated to enable an enhanced switching ratio at a lower power consumption. However, while the elimination of phonon-involvement in nonlinear electronic transition enhances optical nonlinearities, the involvement of real-electronic states in such transitions notably retards the relaxation rate of the refractive index change in direct band gap dielectrics compared to their indirect counterparts.

1.3 Noble Metals and Plasmonic Cavities

In noble metals, optical properties originate from bound and free electrons in the valance and conduction bands, respectively, as described by the Drude model of the dielectric response:

$$\varepsilon(\omega) = \varepsilon_b(\omega) + \varepsilon_f(\omega) = \varepsilon_b(\omega) - \frac{\omega_p^2}{\omega(\omega + i\Gamma)} \qquad (2)$$

where $\varepsilon_b(\omega)$ represents the contribution of bound electrons, $\varepsilon_f(\omega)$ represents the frequency-dependent contribution of free electrons, $\omega_p = \sqrt{n_e e^2/\varepsilon_0 m_e^*}$ is the bulk plasma frequency, n_e is free electron density, m_e^* is the electron effective mass, ε_0 is the free space permittivity, and Γ is the electron scattering rate.(45) Contrary to dielectrics, the lack of an electronic band gap in metals alleviates the free carrier speed limitation; however, on the flip side, the abundance of conduction electrons reduces the sensitivity of their dielectric behavior to the optical modification of electron density. Instead, the illumination of metals initiates a chain of transient processes that starts with the perturbation of the electrons

distribution in the k – space, as schematically depicted in Figure 4a for the case of gold under intraband illumination. Indeed, the optical excitation of metals enables the promotion of free electrons to higher energy states within the conduction band, making a portion of statically-occupied energy levels at the bottom of the conduction band accessible for the interband transition of valance electrons. Depending on the energy of the control (i.e., excitation) light ($\hbar\omega_{co}$), intraband transitions decrease (increase) the number of electrons in k – states that are within the $\hbar\omega_{co}$ energy range below (above) the Fermi level E_F, as qualitatively shown by the modulation of the electron occupation number $f(k)$ in Figure 4b. Such induced $\Delta f(k)$ profile reveals a temporary possibility of the enhancement (reduction) of electronic transitions involving final energy states below (above) E_F and therefore the modulation of $\mathrm{Im}(\varepsilon_b(\omega))$.(46-49) Such light induced permittivity changes are limited to the spectral vicinity of the optical bandgap of noble metals (e.g., $\sim$ 490 nm and $\sim$ 310 nm for gold and silver, respectively) and recover in a few tens of femtosecond through the recombination of electron-hole pairs.(46)

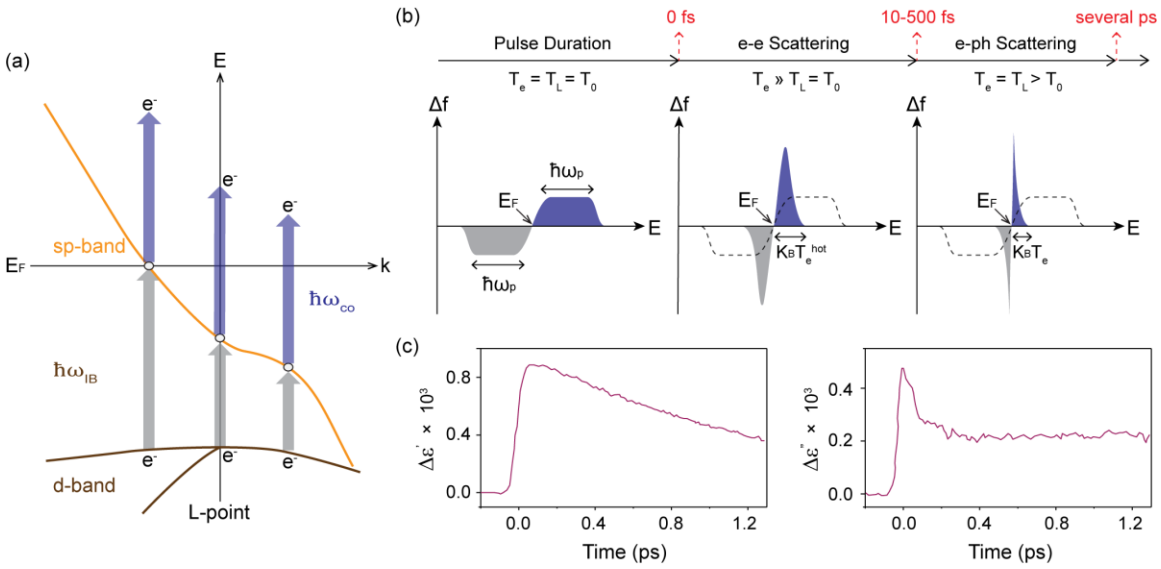

Figure 4: Modulation of the dielectric permittivity in metals. (a) Schematic band-structure of gold around the high-symmetry L-point, under an intraband optical excitation. The blue and gray arrows designate the intraband and interband electronic transition of conduction and valance band electrons, respectively. (b) The intraband optical excitations increases (decreases) the number of electrons in energy states above (below) the Fermi level as indicated by Δf (left panel). At the disappearance of the control light, the thermalization of the excited electrons above the Fermi energy begins via electron-electron scattering leading to the formation of a hot-electron system and therefore smearing of Δf to a $k_B T_e^{hot}$ energy range around the E_F (middle panel). Subsequently, the stored energy in the hot-electron system is transferred to the lattice via electron-phonon interactions and therefore the entire metal structure reaches to an equilibrium condition (right panel). The arrows on the top of panel (b) show the sequence of described transient events with their characteristic timescales. (c) Experimentally measured changes in the real and imaginary parts of the dielectric permittivity of gold.

The described excited-metal structure in the previous part hosts a nonthermal electron gas in its conduction band that is very short lived and can only induce a weak change in the overall dielectric permittivity. Its short lifetime stems from the quick thermalization of the excited electrons through the electron-electron scattering with a rate (Γ_{e-e}) that qualitatively is in the form of $\Gamma_{e-e} \propto (E - E_F)^2$, where E is the energy of an

excited electron.(46, 50) This qualitative relation indicates a higher scattering rate for the electrons at the high-energy tail of the nonthermal system compared to those close to E_F, a fact that assists fast thermalization of electrons. During the thermalization step, which takes place in a 100 fs – 1 ps timeframe,(46, 48, 51-53) the absorbed energy of the control light is redistributed among all conduction electrons yielding a hot-electron gas with a characteristic temperature T_e^{hot} much larger than the room temperature (T_0). The formation of hot-electron gas narrows down the extent of the perturbed energy zone around the Fermi level to a region defined by $k_B T_e^{hot}$, as illustrated in the middle panel of Figure 4b. At this time stage the induced interband electronic transitions play a minor role, and instead the modulation of $\Gamma_{e-e} \sim T_e^2$,(46, 48) due to the increased electron temperature represents the primary source of the permittivity tuning because the imaginary part of $\varepsilon_f(\omega)$ is proportional to Γ_{e-e}.(46, 48) The recovery of the permittivity then occurs through the energy transfer from hot electrons to the metal lattice via electron-phonon interactions (Γ_{e-ph}), a process that establishes the thermal equilibration of electrons and the lattice. Since the lattice heat capacity (C_l) is typically much larger than the electron heat capacity (C_e), under the equilibrium condition T_l and T_e are only slightly above the room temperature (i.e., $T_0 < T_e = T_l \ll T_e^{hot}$), concluding to the smearing of the electron distribution around the Fermi level (Figure 4b, the right panel). The dynamics of energy exchange between hot electrons and the lattice is described using two-temperature rate equations:

$$C_e(T_e)\frac{\partial T_e}{\partial t} = -G(T_e - T_l) \qquad (3)$$

$$C_l \frac{\partial T_l}{\partial t} = G(T_e - T_l)$$

where G represents the electron – phonon coupling coefficient. Assume that C_e is independent of T_e, *Eq. (3)* predicts a several-picosecond timescale after which a thermal equilibrium condition can be reached within the metal via electron-phonon interactions. The described transient mechanism for tuning the dielectric permittivity of metal has been experimentally verified for several noble metals.(48) As an example, Figure 4c shows the measured temporal evolution of $\Delta\varepsilon$ for a thin gold film for the case of a weak optical perturbation. As seen, the maximum $\Delta\varepsilon$ arrives 100 fs after the formation of nonthermal electrons, via electron-electron interactions, and then exponentially decays in a few picoseconds, consistent with the predicted electron-phonon interaction rate using *Eq. (3)*.

The critical influence of T_e^{hot} on the magnitude of the permittivity change substantiates the need for maximizing this parameter via optical illumination. To do so, exploiting metals with small C_e facilitates the creation a hot-electron population with a significantly elevated effective temperature. More importantly, enhancing light absorption provides more optical energy to be stored inside the conduction electrons. Contrary to dielectrics, the reflective nature of planar metal films, for photons with energies less than their optical bandgap, substantially lowers their photon-to-electron conversion efficiency. However, by limiting the geometrical boundaries of metals to nanoscale regimes, the absorption efficiency dramatically increases through the coupling of incident electromagnetic waves to the coherent oscillation of conduction electrons, known as plasmon resonances. In plasmonic structures, the mechanism for creating a nonthermal electron distribution is different in the sense that the illumination of the control light

initially excites associated plasmon modes and the subsequent transfer of plasmon energy packets to electrons (e.g., via Landau damping) enables electronic transitions (Figure 5a).(54-58) Capabilities of metals for optical modulation have been vastly explored by employing plasmonic cavities made of randomly dispersed metallic particles (Figure 5b),(52, 59-61) highly-ordered arrays of nanostructures (Figure 5c),(62-65) and propagating surface plasmon modes (Figure 5d).(66-69) Similar to dielectric cavities, the manipulation of dielectric permittivity of metals leads to the modulation of light transmission or reflection upon interaction with plasmonic structures.

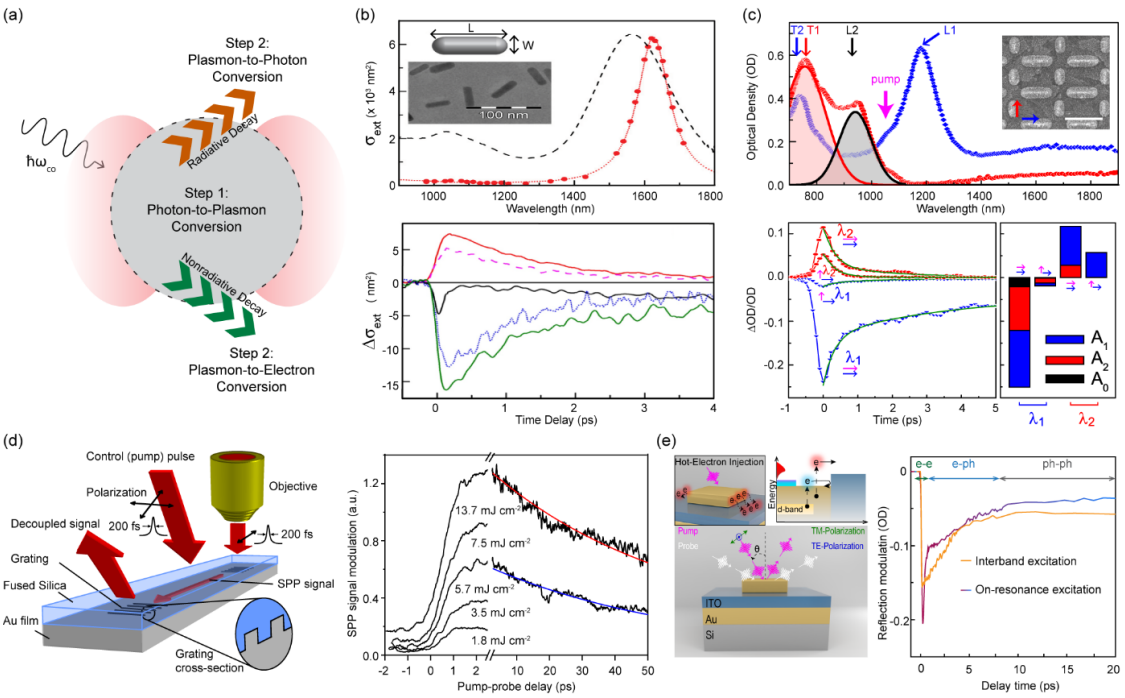

Figure 5: All-optical control of plasmons. (a) Generating nonthermal electrons in plasmonic cavities. The control light initially excites a plasmon oscillation and the subsequent nonradiative decay of plasmon elevates either the bound or free electrons to energy states above the Fermi level. (b) Controlling the plasmonic resonance of gold nanorods randomly dispersed in a solution. The top and bottom panels exhibit the linear and modulated response of the structure. (c) Modulating the light-matter interaction using highly ordered localized plasmon modes. The linear and modulation behaviors of the device are depicted in top and bottom panels, respectively. (d) All-

optical control of surface plasmon propagation. (e) Femtosecond all-optical modulation enabled by the hot-electron transfer, utilizing dark lattice plasmon modes. Through the excitation of dark plasmon modes, the hot-electron generation is maximized and the transfer of such energetic carriers to an adjacent electron-accepting material enables the femtosecond modulation of cavity modes.

One critical consideration in the design of plasmonic modulators is to utilize dark (i.e., subradiant) resonances to suppress the radiation loss and thusly secure the plasmon energy for the generation of hot electrons.(65, 70) Moreover, since dark plasmonic resonances such as lattice- and Fano-type modes often provide narrow spectral linewidths, even a small change in the dielectric permittivity potentially facilitates achieving a large on-to-off switching ratio for a low energy-consumption scheme.(65, 71) Although the achievable modulation speed in plasmonic modulators is generally faster than their dielectric counterparts, nonetheless, the need for maximizing $\Delta\varepsilon$ through T_e^{hot} impedes the realization of a large switching ratio along with a sub-picosecond timeframe. This limitation originates from the temperature dependency of electron heat capacity, $C_e \sim T_e$ under strong optical perturbations.(46) In fact, solutions to the rate equations in *Eq. (3)* suggest that $\Gamma_{e-ph} \approx GC_e(T_e)^{-1}$, therefore, by increasing the electron temperature, the rate of energy transfer from the electron gas to the lattice drops and the modulation speed stays limited to several picoseconds. One way to overcome this limit is to enable additional pathways for the electron relaxation. In a recent report (Figure 5e),(65) the extraction of electrons from plasmonic cavities by constructing a Schottky barrier has been proposed as a solution to this issue. In fact, the hot-electron transfer triggers a femtosecond electron-dominated relaxation channel that partially circumvents the contribution of phonons in the equilibration of optically excited plasmonic system.(65)

The experimental evaluation of the third-order susceptibility of metals, particularly around plasmonic resonances, requires careful consideration of optical field intensity. As we discussed before (Figure 4b), the intensity of control light is directly correlated to the hot-electron temperature, a parameter that affects the spectral width of the perturbed region around E_F. Consequently, the probability of two-photon electronic transitions, expressed based on $Im\{\chi^3(\omega)\}$ or β_2, cannot be measured independent of the incident light intensity, especially for the case of *d* – band electrons. Moreover, the enhanced linear excitation of bound electrons adds an intensity-dependent loss channel to the plasmonic cavity, leading to a diminished local field enhancement and further increasing the intensity-dependency of $\chi^3(\omega)$, with a generally decaying trend.(72) Although the local-field enhancement provided by plasmonic modes assists to boost the nonlinear response of metals, it also increases the level of complexity to the dispersive behavior of $\chi^3(\omega)$. Finally, the intrinsically fast dynamics of excited electrons in metals, raises serious concerns regarding the impact of time-domain accuracy of characterization tools, such as the laser pulse width, on the extraction of nonlinear coefficients. Because of these reasons, we are witnessing a large variation, more than one of magnitude, in the reported values of the third-order susceptibility of metals in the literature.

1.4 Epsilon-Near-Zero Materials and Structures

The basic rules of electromagnetics enforce the continuity of the normal components of electric displacement field at a charge free interface, once a time-harmonic wave passes through one medium to another. This requirement, in fact, results in the discontinuity of the normal electric field components across the interface between the two media with a

relative ratio scaled as $\frac{E_{1n}}{E_{2n}} = \frac{\varepsilon_2}{\varepsilon_1}$. Under a hypothetical condition, if ε_1 approaches zero, the electric field inside the less-refractive medium (e.g., medium 1) significantly skyrockets and therefore, the nonlinear interactions of light with medium 1 become substantially strong, as can be predicted by *Eq. 1*. Materials with such a fascinating behavior are called epsilon-near-zero (ENZ) media and recently have gained a great deal of attention in various areas of photonics.(73) Intuitively, the exotic ENZ behavior naturally occurs in Drude-like media with a high density of free electrons as we approach their bulk plasma frequency:

$$\varepsilon_D(\omega) = 1 - \frac{\omega_p^2}{\omega(\omega + i\Gamma)} \xrightarrow{\omega \gg \Gamma} 1 - \frac{\omega_p^2}{\omega^2} \xrightarrow{\omega \to \omega_p} 0 \quad (4)$$

The ENZ effect is intrinsically linked to the wavelength stretching, which dictates the electric field to display a near-static spatial distribution throughout the media, while sustaining its time-harmonic character, therefore, delocalizing the enormous field enhancement over a large area.(73-74) Besides field enhancement, nonlinear effects further benefit from ENZ materials as the slow nature of the group velocity around an ENZ frequency enables the expansion of the interaction time between optical fields and nonlinear media.(75-77) Among various materials, transparent conductive oxides (TCOs) such as indium tin oxide (ITO), aluminum- and gallium-doped zinc oxide, and indium-doped cadmium oxide,(78-81) are the most prominent members of this class of materials. The accurate control over their doping level enables TCOs to exhibit an ENZ response at a prescribed frequency from the near- to mid-infrared regime.

Motivated by unique features that ENZ concept has to offer, the third-order nonlinearity of TCOs has been studied (78, 82) and further exploited for all-optical control

of light (83-86) as illustrated in Figure 6. Around the ENZ frequency, TCO materials exhibit enormous Kerr and TPA responses that are several orders of magnitude larger than achievable values using dielectrics and noble metals.(78, 82) From a macroscopic perspective, this enhanced nonlinearity is not surprising once we consider that n_2 and β_2 are proportional to $\varepsilon(\omega)^{-1}$, revealing the superiority of the near-zero regime over other frequencies, regardless of the intrinsic material properties. From a microscopic point of view, the far lower electron density in conductive oxides and their relatively smaller electron heat capacity should be accounted for the observed large optical nonlinearities. The small C_e of TCOs allows to achieve hot-electron temperatures ($\sim$ 5000 °K) greatly exceeding that of noble metals ($\sim$ 2000 °K) by consuming equal energy and thusly modulating the electron scattering rate and the plasma frequency because of the non-parabolic nature of their perturbed conduction band (Figure 6b).(85, 87, 88) Moreover, as described by electron-energy-loss rate in *Eq. (3)*, the reduced heat capacity of electrons in conductive oxides expedites the energy exchange between the thermalized electron gas and the lattice with a characteristic sub-picosecond timescale (Figure 6b). Despite all these amenities, one major shortcoming in utilizing bulk ENZ materials for all-optical modulation is their spectral limitation to the near- and mid-infrared frequency range that is ultimately limited by their free electron density. This constraint can be relieved through the rational design of metamaterial structures –artificially stacked subwavelength layers and nanostructures made of both positive and negative permittivity materials– to develop ENZ behavior at a tailored frequency range, including the visible and near-infrared (Figure 6c).(89-92) ENZ structures can further invoke all benefits that metamaterial platforms have to offer, such as beam shaping and manipulation that are out of the reach by exploiting

conventional bulk counterparts.(93-95) However, since the use of metals are almost ubiquitous in metamaterial designs, particularly at the visible range, we usually loose the opportunity to obtain a femtosecond modulation speed in structured ENZ platforms.

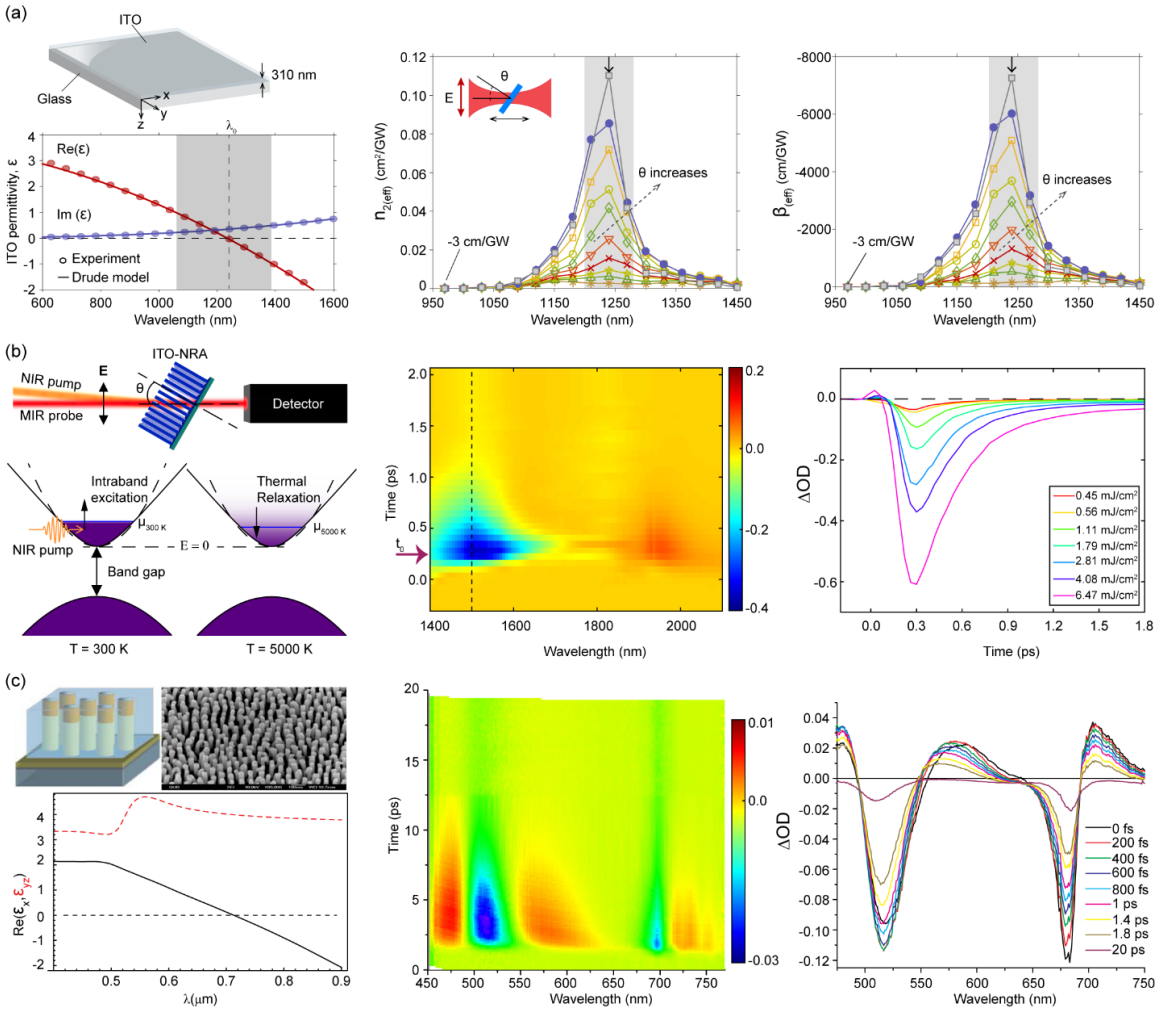

Figure 6: All-optical modulation utilizing ENZ materials and structures. (a) The intrinsic third-order nonlinearity of ITO as a representative TCO near its ENZ frequency. Several orders of magnitude enhancement in the Kerr and TPA coefficients have been observed. (b) An ITO-based device for ultrafast control of light intensity around the ENZ region. The low electron heat capacity of ITO allows achieving an ultrafast modulation speed. (c) Inducing ENZ response through the design of a metamaterial platform, made of gold and alumina, envisioned for all-optical modulation within the visible spectrum. By controlling the geometry of the device, ENZ frequency can be obtained at a prescribed frequency.

1.5 Other Material and Device Platforms

Majority of methods that we discussed above lead to a volatile change in the optical constant of active materials. However, Phase-change nanophotonics has recently garnered significant attention thanks to the unique features of phase-change chalcogenides enabling reconfigurable metasurface and integrated photonics platforms in a nonvolatile fashion (98, 99). Particularly, the intermediate phase transition of such non-volatile materials empowers metasurfaces to induce arbitrary transformations in the properties of the incident light, leading to reprogrammable pixelated multifunctional flat-optics (100-102). In addition, as the history of nanotechnology in various aspects of science such as nanobioscience (103-105) and nanophotonics (106-109) has proven, approaching the atomic scales unlocks new opportunities that bulk materials can not provide. In this regard, 2D materials have been proven to be great candidates to provide active optical media for reversible control of light-matter interactions. Approaching the length of atomic bonds is indeed the extreme case of miniaturization, which is primarily offered by the family of 2D materials. As the foremost member of this family, graphene has been vastly employed for optical switching in a variety of configurations, at the near- to midinfrared regime. Transition metal dichalcogenides (TMDs) are the semiconducting counterpart of graphene with a nonzero electronic bandgap ranging from 1 to 2.5 eV, enabling ultrafast modulation of light-matter interaction through the ultrafast photocarrier generation.

Inspired by the recent advancements in optical metasurfaces and metamaterials, metamaterials have also been extensively studied for mechanical waves for both discrete and continuous systems, with the potential applications in signal filtering, multiplexing/demultiplexing, and sound isolating. Recently, they have been explored to

design mechanical lenses and waveguides for elastic waves to focus the energy of the wave for a broad range of frequency (110-114), or to tailor the rigidity locally to achieve cloaking structures (111). In addition, discrete systems have been employed in the past few years to demonstrate non-reciprocity for phononic systems, which open a new window towards designing mechanical filters and diodes (114, 115). Finally, mechanical meta-surfaces have been investigated to exhibit topological behavior with both passive and active techniques (116-119). These topological insulators are fabricated by altering the material properties of the metasurface by using shunted piezoelectric disks. Such demonstrations reveal the importance of expanding the knowledge of active device platforms for the fast control of wave-matter interactions in a general scheme.

1.6 References

1. Liu, A.; Jones, R.; Liao, L.; Samara-Rubio, D.; Rubin, D.; Cohen, O.; Nicolaescu, R.; Paniccia, M. A high-speed silicon optical modulator based on a metal-oxide-semiconductor capacitor. *Nature* **2004**, 427, 615-618.
2. Reed, G. T.; Mashanovich, G.; Gardes, F. Y.; Thomson, D. J. Silicon optical modulators. *Nat. Photonics.* **2010**, 4, 518-526.
3. Ayata, M.; Fedoryshyn, Y.; Heni, W.; Baeuerle, B.; Josten, A.; Zahner, M.; Koch, U.; Salamin, Y.; Hoessbacher, C.; Haffner, C.; Elder, D. L.; Dalton, L. R.; Leuthold, J. High-speed plasmonic modulator in a single metal layer. *Science* **2017**, 358, 630-632.
4. Cocorullo, G.; Della Corte, F. G.; Rendina, I.; Sarro, P. M. Thermo-optic effect exploitation in silicon microstructures. *Sens. Actuators A.* **1998**, 71, 19-26.
5. Cocorullo, G.; Della Corte, F. G.; Rendina, I.; Rubino, A.; Terzini, E. Thermo-optical modulation at λ = 1.5 μm in an α-SiC-α-Si-α-SiC planar guided-wave structure. *IEEE Photon. Technol. Lett.* **1996**, 8, 900-902.
6. Taghinejad, H., Abdollahramezani, S., Eftekhar, A.A., Fan, T., Hosseinnia, A.H., Hemmatyar, O., Dorche, A.E., Gallmon, A. and Adibi, A., 2020. ITO-Based $\mu $-Heaters for Multi-Stage Switching of Phase-Change Materials: Towards Beyond-Binary Reconfigurable Integrated Photonics. arXiv preprint arXiv:2003.04097.
7. Fonjallaz, P. Y.; Limberger, H. G.; Salathe, R. P.; Cochet, F.; Leuenberger, B. Tension increase correlated to refractive-index change in fibers containing UV-written bragg gratings. *Opt. Lett.* **1995**, 20, 1346-1348.
8. Primak, W.; Post, D. Photoelastic constants of vitreous silica and its elastic coefficient of refractive index. *J. Appl. Phys.* **1959**, 30, 779-788.

9. Nagano, K.; Kawakami, S.; Nishida, S. Change of the refractive index in an optical fiber due to external forces. *Appl. Opt.* **1978**, 17, 2080-2085.
10. Abdollahramezani, S.; Hemmatyar, O.; Taghinejad, H.; Krasnok, A.; Kiarashinejad, Y.; Zandehshahvar, M.; Alu, A.; Adibi, A. Tunable nanophotonics enabled by chalcogenide phase-change materials. *Nanophotonics-Berlin* **9**, 1189-1241 (2020).
11. Adair, R.; Chase, L. L.; Payne, S. A. Nonlinear refractive-index of optical-crystals. *Phys. Rev. B* **1989**, 39, 3337-3350.
12. Van Stryland, E. W.; Woodall, M. A.; Vanherzeele, H.; Soileau, M. J. Energy band-gap dependence of two-photon absorption. *Opt. Lett.* **1985**, 10, 490-492.
13. Taghinejad, M.; Taghinejad, H.; Ganji, M.; Rostamian, A.; Mohajerzadeh, S.; Abdolahad, M.; Kolahdouz, M. Integration of Ni2Si/Si Nanograss Heterojunction on n-MOSFET to Realize High-Sensitivity Phototransistors. *IEEE Trans. Electron. Dev.* **2014**, 61, 3239.
14. Taghinejad, H.; Taghinejad, M.; Abdolahad, M.; Rajabali, S.; Rostamian, A.; Mohajerzadeh, S.; Hosseinian, E. The conformal silicon deposition on carbon nanotubes as enabled by hydrogenated carbon coatings for synthesis of carbon/silicon core/shell heterostructure photodiodes. Carbon 87, 299-308 (2015).
15. Lan, S. F.; Zhang, X. Y.; Taghinejad, M.; Rodrigues, S.; Lee, K. T.; Liu, Z. C.; Cai, W. S. Metasurfaces for Near-Eye Augmented Reality. *ACS Photonics* 6, 864-870 (2019).
16. Dekker, R.; Usechak, N.; Forst, M.; Driessen, A. Ultrafast nonlinear all-optical processes in silicon-on-insulator waveguides. *J. Phys. D* **2007**, 40, R249-R271.
17. Leuthold, J.; Koos, C.; Freude, W. Nonlinear silicon photonics. *Nat. Photonics.* **2010**, 4, 535-544.
18. Boyd, R. W. Nonlinear optics 3rd edn (Academic Press, **2008)**.
19. Almeida, V. R.; Barrios, C. A.; Panepucci, R. R.; Lipson, M. All-optical control of light on a silicon chip. *Nature* **2004**, 431, 1081-1084.
20. Tsang, H. K.; Wong, C. S.; Liang, T. K.; Day, I. E.; Roberts, S. W.; Harpin, A.; Drake, J.; Asghari, M. Optical dispersion, two-photon absorption and self-phase modulation in silicon waveguides at 1.5 μm wavelength. *Appl. Phys. Lett.* **2002**, 80, 416-418.
21. Martinez, A.; Blasco, J.; Sanchis, P.; Galan, J. V.; Garcia-Ruperez, J.; Jordana, E.; Gautier, P.; Lebour, Y.; Hernandez, S.; Spano, R.; Guider, R.; Daldosso, N.; Garrido, B.; Fedeli, J. M.; Pavesi, L.; Marti, J. Ultrafast all-optical switching in a silicon-nanocrystal-based silicon slot waveguide at telecom wavelengths. *Nano Lett.* **2010**, 10, 2288-2288.
22. Liu, Y.; Tsang, H. K. Time dependent density of free carriers generated by two photon absorption in silicon waveguides. *Appl. Phys. Lett.* **2007**, 90, 211105-3.
23. Pelc, J. S.; Rivoire, K.; Vo, S.; Santori, C.; Fattal, D. A.; Beausoleil, R. G. Picosecond all-optical switching in hydrogenated amorphous silicon microring resonators. *Opt. Express.* **2014**, 22, 3797-3810.
24. Johnson, T. J.; Borselli, M.; Painter, O. Self-induced optical modulation of the transmission through a high-Q silicon microdisk resonator. *Opt. Express.***2006**, 14, 817-831.
25. Fukuda, H.; Yamada, K.; Shoji, T.; Takahashi, M.; Tsuchizawa, T.; Watanabe, T.; Takahashi, J.; Itabashi, S. Four-wave mixing in silicon wire waveguides. *Opt. Express.* **2005**, 13, 4629-4637.
26. Dinu, M.; Quochi, F.; Garcia, H. Third-order nonlinearities in silicon at telecom wavelengths. *Appl. Phys. Lett.* **2003**, 82, 2954-2956.
27. Liu, A. S.; Rong, H. S.; Paniccia, M. Net optical gain in a low loss silicon-on-insulator waveguide by stimulated Raman scattering. *Opt. Express.* **2004**, 12, 4261-4268.

28. Claps, R.; Raghunathan, V.; Dimitropoulos, D.; Jalali, B. Influence of nonlinear absorption on Raman amplification in Silicon waveguides. *Opt. Express* **2004**, 12, 2774-2780.
29. Rong, H. S.; Liu, A. S.; Nicolaescu, R.; Paniccia, M.; Cohen, O.; Hak, D. Raman gain and nonlinear optical absorption measurements in a low-loss silicon waveguide. *Appl. Phys. Lett.* **2004**, 85, 2196-2198.
30. Liang, T. K.; Tsang, H. K. Nonlinear absorption and Raman scattering in silicon-on-insulator optical waveguides. *IEEE J. Sel. Topics Quantum Electron.* **2004**, 10, 1149-1153.
31. Dinu, M. Dispersion of phonon-assisted nonresonant third-order nonlinearities. *IEEE J. Quantum Electron.* **2003**, 39, 1498-1503.
32. Sheikbahae, M.; Hutchings, D. C.; Hagan, D. J.; Van Stryland, E. W. Dispersion of bound electronic nonlinear refraction in solids. *IEEE J. Quantum Electron.* **1991**, 27, 1296-1309.
33. Sheik-Bahae, M.; Hagan, D. J.; Van Stryland, E. W. Dispersion and band-gap scaling of the electronic Kerr effect in solids associated with two-photon absorption. *Phys. Rev. Lett.* **1990**, 65, 96-99.
34. Wherrett, B. S. Scaling rules for multiphoton interband absorption in semiconductors. *J. Opt. Soc. Am. B* **1984**, 1, 67-72.
35. Nozaki, K.; Tanabe, T.; Shinya, A.; Matsuo, S.; Sato, T.; Taniyama, H.; Notomi, M. Sub-femtojoule all-optical switching using a photonic-crystal nanocavity. *Nat. Photonics.* **2010**, 4, 477-483.
36. Tanabe, T.; Nishiguchi, K.; Shinya, A.; Kuramochi, E.; Inokawa, H.; Notomi, M.; Yamada, K.; Tsuchizawa, T.; Watanabe, T.; Fukuda, H.; Shinojima, H.; Itabashi, S. Fast all-optical switching using ion-implanted silicon photonic crystal nanocavities. *Appl. Phys. Lett.* **2007**, 90, 031115-3.
37. Tanabe, T.; Notomi, M.; Mitsugi, S.; Shinya, A.; Kuramochi, E. All-optical switches on a silicon chip realized using photonic crystal nanocavities. *Appl. Phys. Lett.* **2005**, 87, 151112-3.
38. Shcherbakov, M. R.; Vabishchevich, P. P.; Shorokhov, A. S.; Chong, K. E.; Choi, D. Y.; Staude, I.; Miroshnichenko, A. E.; Neshev, D. N.; Fedyanin, A. A.; Kivshar, Y. S. Ultrafast all-optical switching with magnetic resonances in nonlinear dielectric nanostructures. *Nano Lett.* **2015**, 15, 6985-6990.
39. Baranov, D. G.; Makarov, S. V.; Milichko, V. A.; Kudryashov, S. I.; Krasnok, A. E.; Belov, P. A. Nonlinear transient dynamics of photoexcited resonant silicon nanostructures. *ACS Photon.* **2016**, 3, 1546-1551.
40. Makarov, S.; Kudryashov, S.; Mukhin, I.; Mozharov, A.; Milichko, V.; Krasnok, A.; Belov, P. Tuning of magnetic optical response in a dielectric nanoparticle by ultrafast photoexcitation of dense electron-hole plasma. *Nano Lett.* **2015**, 15, 6187-6192.
41. Shcherbakov, M. R.; Liu, S.; Zubyuk, V. V.; Vaskin, A.; Vabishchevich, P. P.; Keeler, G.; Pertsch, T.; Dolgova, T. V.; Staude, I.; Brener, I.; Fedyanin, A. A. Ultrafast all-optical tuning of direct-gap semiconductor metasurfaces. *Nat. Commun.* **2017**, 8, 17.
42. Jin, R.; Chuang, C. L.; Gibbs, H. M.; Koch, S. W.; Polky, J. N.; Pubanz, G. A. Picosecond all-optical switching in single-mode GaAs/AlGaAs strip-loaded nonlinear directional-couplers. *Appl. Phys. Lett.* **1988**, 53, 1791-1793.
43. Harding, P. J.; Euser, T. G.; Nowicki-Bringuier, Y. R.; Gerard, J. M.; Vos, W. L. Dynamical ultrafast all-optical switching of planar GaAs/AlAs photonic microcavities. *Appl. Phys. Lett.* **2007**, 91,111103-3.

44. Husko, C.; De Rossi, A.; Combrie, S.; Tran, Q. V.; Raineri, F.; Wong, C. W. Ultrafast all-optical modulation in GaAs photonic crystal cavities. *Appl. Phys. Lett.* **2009**, 94, 021111-3.
45. Cai, W.; Shalaev, V. M. Optical metamaterials: Fundamentals and applications (Springer **2010**).
46. Voisin, C.; Del Fatti, N.; Christofilos, D.; Vallee, F. Ultrafast electron dynamics and optical nonlinearities in metal nanoparticles. *J. Phys. Chem. B* **2001**, 105, 2264-2280.
47. Park, S.; Pelton, M.; Liu, M.; Guyot-Sionnest, P.; Scherer, N. F. Ultrafast resonant dynamics of surface plasmons in gold nanorods. *J. Phys. Chem. C* **2007**, 111, 116-123.
48. Del Fatti, N.; Voisin, C.; Achermann, M.; Tzortzakis, S.; Christofilos, D.; Vallee, F. Nonequilibrium electron dynamics in noble metals. *Phys. Rev. B* **2000**, 61, 16956-16966.
49. Sun, C. K.; Vallee, F.; Acioli, L.; Ippen, E. P.; Fujimoto, J. G. Femtosecond investigation of electron thermalization in gold. *Phys. Rev. B* **1993**, 48, 12365-12368.
50. Sykes, M. E.; Stewart, J. W.; Akselrod, G. M.; Kong, X. T.; Wang, Z. M.; Gosztola, D. J.; Martinson, A. B. F.; Rosenmann, D.; Mikkelsen, M. H.; Govorov, A. O.; Wiederrecht, G. P. Enhanced generation and anisotropic Coulomb scattering of hot electrons in an ultra-broadband plasmonic nanopatch metasurface. *Nat. Commun.* **2017**, 8, 986.
51. Huang, W. Y.; Qian, W.; El-Sayed, M. A. The optically detected coherent lattice oscillations in silver and gold monolayer periodic nanoprism arrays: The effect of interparticle coupling. *J. Phys. Chem. B* **2005**, 109, 18881-18888.
52. Link, S.; El-Sayed, M. A. Spectral properties and relaxation dynamics of surface plasmon electronic oscillations in gold and silver nanodots and nanorods. *J. Phys. Chem. B* **1999**, 103, 8410-8426.
53. Del Fatti, N.; Vallee, F.; Flytzanis, C.; Hamanaka, Y.; Nakamura, A. Electron dynamics and surface plasmon resonance nonlinearities in metal nanoparticles. *Chem. Phys.* **2000**, 251, 215-226.
54. Govorov, A. O.; Richardson, H. H. Generating heat with metal nanoparticles. *Nano Today* **2007**, 2, 30-38.
55. Govorov, A. O.; Zhang, H.; Gun'ko, Y. K. Theory of photoinjection of hot plasmonic carriers from metal nanostructures into semiconductors and surface molecules. *J. Phys. Chem. C* **2013**, 117, 16616-16631.
56. Govorov, A. O.; Zhang, H.; Demir, H. V.; Gun'ko, Y. K. Photogeneration of hot plasmonic electrons with metal nanocrystals: Quantum description and potential applications. *Nano Today* **2014**, 9, 85-101.
57. Brongersma, M. L.; Halas, N. J.; Nordlander, P. Plasmon-induced hot carrier science and technology. *Nat. Nanotechnol.* **2015**, 10, 25-34.
58. Sundararaman, R.; Narang, P.; Jermyn, A. S.; Goddard, W. A; .Atwater, H. A. Theoretical predictions for hot-carrier generation from surface plasmon decay. *Nat. Commun.* **2014**, 5. 5788.
59. Baida, H.; Mongin, D.; Christofilos, D.; Bachelier, G.; Crut, A.; Maioli, P.; Del Fatti, N.; Vallee, F. Ultrafast nonlinear optical response of a single gold nanorod near its surface plasmon resonance. *Phys. Rev. Lett.* **2011**, 107, 057402-5.
60. Yu, K.; Polavarapu, L.; Xu, Q. H. Excitation wavelength and fluence dependent femtosecond transient absorption studies on electron dynamics of gold nanorods. *J. Phys. Chem. A* **2011**, 115, 3820-3826.

61. Wang, X. L.; Guillet, Y.; Selvakannan, P. R.; Remita, H.; Palpant, B. Broadband spectral signature of the ultrafast transient optical response of gold nanorods. *J. Phys. Chem. C* **2015**, 119, 7416-7427.
62. Abb, M.; Wang, Y. D.; de Groot, C. H.; Muskens, O. L. Hotspot-mediated ultrafast nonlinear control of multifrequency plasmonic nanoantennas. *Nat. Commun.* **2014**, 5, 4869.
63. Dintinger, J.; Robel, I.; Kamat, P. V.; Genet, C.; Ebbesen, T. W. Terahertz all-optical molecule-plasmon modulation. *Adv. Mater.* **2006**, 18, 1645-1648.
64. Dani, K. M.; Ku, Z. Y.; Upadhya, P. C.; Prasankumar, R. P.; Brueck, S. R. J.; Taylor, A. J. Subpicosecond optical switching with a negative index metamaterial. *Nano Lett.* **2009**, 9, 3565-3569.
65. Taghinejad, M.; Taghinejad, H.; Xu, Z.; Liu, Y.; Rodrigues, S. P.; Lee, K. T.; Lian, T.; Adibi, A.; Cai, W. S. Hot-electron-assisted femtosecond all-optical modulation in plasmonics. *Adv. Mater.* **2018**, 30, 1704915-1704915.
66. MacDonald, K. F.; Samson, Z. L.; Stockman, M. I.; Zheludev, N. I. Ultrafast active plasmonics. *Nat. Photonics.* **2009**, 3, 55-58.
67. Fu, Y.; Hu, X.; Lu, C.; Yue, S.; Yang, H.; Gong, Q. All-optical logic gates based on nanoscale plasmonic slot waveguides. *Nano Lett.* **2012**, 12, 5784-90.
68. Chen, J. J.; Li, Z.; Yue, S.; Gong, Q. H. Highly efficient all-optical control of surface-plasmon-polariton generation based on a compact asymmetric single slit. *Nano Lett*. **2011**, 11, 2933-2937.
69. Husko, C.; De Rossi, A.; Combrie, S.; Tran, Q. V.; Raineri, F.; Wong, C. W. Ultrafast all-optical modulation in GaAs photonic crystal cavities. *Appl. Phys. Lett.* **2009**, 94, 021111-3
70. Taghinejad, M.; Taghinejad, H.; Malak, S. T.; Moradinejad, H.; Woods, E. V.; Xu, Z.; Liu, Y.; Eftekhar, A. A.; Lian, T.; Tsukruk, V. V.; Adibi, A. Sharp and tunable crystal/Fano-type resonances enabled by out-of-plane dipolar coupling in plasmonic nanopatch arrays. *Ann. Phys. (Berlin)* **2018**, 530, 1700395-1700402.
71. Lan, S.; Rodrigues, S. P.; Taghinejad, M.; Cai, W. Dark plasmonic modes in diatomic gratings for plasmoelectronics. Laser & Photonics Reviews 11, (2017).
72. Hache, F.; Ricard, D.; Flytzanis, C.; Kreibig, U. The optical Kerr effect in small metal particles and metal colloids: The case of gold. *Appl. Phys. A* **1988**, 47, 347-357.
73. Liberal, I.; Engheta, N. Near-zero refractive index photonics. *Nat. Photonics* **2017**, 11, 264-264.
74. Edwards, B.; Alu, A.; Young, M. E.; Silveirinha, M.; Engheta, N. Experimental verification of epsilon-near-zero metamaterial coupling and energy squeezing using a microwave waveguide. *Phys. Rev. Lett.* **2008**, 100, 033903-4.
75. Liberal, I.; Engheta, N. Nonradiating and radiating modes excited by quantum emitters in open epsilon-near-zero cavities. *Sci. Adv.* **2016**, 2, e1600987-e1600993.
76. Ciattoni, A.; Marini, A.; Rizza, C.; Scalora, M.; Biancalana, F. Polariton excitation in epsilon-near-zero slabs: Transient trapping of slow light. *Phys. Rev. A* **2013**, 87, 053853-8.
77. Krauss, T. F. Why do we need slow light? *Nat. Photonics* **2008**, 2, 448-450.
78. Alam, M. Z.; De Leon, I.; Boyd, R. W. Large optical nonlinearity of indium tin oxide in its epsilon-near-zero region. *Science* **2016**, 352, 795-797.

79. Capretti, A.; Wang, Y.; Engheta, N.; Dal Negro, L. Enhanced third-harmonic generation in Si-compatible epsilon-near-zero indium tin oxide nanolayers. *Opt. Lett.* **2015**, 40, 1500-1503.
80. Naik, G. V.; Kim, J.; Boltasseva, A. Oxides and nitrides as alternative plasmonic materials in the optical range. *Opt. Mater. Express* **2011**, 1, 1090-1099.
81. Naik, G. V.; Shalaev, V. M.; Boltasseva, A. Alternative plasmonic materials: Beyond gold and silver. *Adv. Mater.* **2013**, 25, 3264-3294.
82. Caspani, L.; Kaipurath, R. P. M.; Clerici, M.; Ferrera, M.; Roger, T.; Kim, J.; Kinsey, N.; Pietrzyk, M.; Di Falco, A.; Shalaev, V. M.; Boltasseva, A.; Faccio, D. Enhanced nonlinear refractive index in epsilon-near-zero materials. *Phys. Rev. Lett.* **2016**, 116, 233901-5.
83. Kinsey, N.; DeVault, C.; Kim, J.; Ferrera, M.; Shalaev, V. M.; Boltasseva, A. Epsilon-near-zero Al-doped ZnO for ultrafast switching at telecom wavelengths. *Optica* **2015**, 2, 616-622.
84. Alam, M. Z.; Schulz, S. A.; Upham, J.; De Leon, I.; Boyd, R. W. Large optical nonlinearity of nanoantennas coupled to an epsilon-near-zero material. *Nat. Photonics* **2018**, 12, 79-84.
85. Guo, P. J.; Schaller, R. D.; Ketterson, J. B.; Chang, R. P. H. Ultrafast switching of tunable infrared plasmons in indium tin oxide nanorod arrays with large absolute amplitude. *Nat. Photonics* **2016**, 10, 267-274.
86. Guo, P. J.; Schaller, R. D.; Ocola, L. E.; Diroll, B. T.; Ketterson, J. B.; Chang, R. P. H. Large optical nonlinearity of ITO nanorods for sub-picosecond all-optical modulation of the full-visible spectrum. *Nat. Commun.* **2016**, 7, 12892.
87. Liu, X. G.; Park, J.; Kang, J. H.; Yuan, H. T.; Cui, Y.; Hwang, H. Y.; Brongersma, M. L. Quantification and impact of nonparabolicity of the conduction band of indium tin oxide on its plasmonic properties. *Appl. Phys. Lett*. **2014**, 105, 181117-5.
88. Pisarkiewicz, T.; Kolodziej, A. Nonparabolicity of the conduction-band structure in degenerate tin dioxide. *Phys. Status Solidi B* **1990**, 158, K5-K8.
89. Vesseur, E. J. R.; Coenen, T.; Caglayan, H.; Engheta, N.; Polman, A. Experimental verification of n=0 dtructures for visible light. *Phys. Rev. Lett.* **2013**, 110, 013902-5.
90. Pollard, R. J.; Murphy, A.; Hendren, W. R.; Evans, P. R.; Atkinson, R.; Wurtz, G. A.; Zayats, A. V.Podolskiy, V. A. Optical nonlocalities and sdditional waves in rpsilon-near-zero metamaterials. *Phys. Rev. Lett.* **2009**, 102, 127405-4.
91. Maas, R.; Parsons, J.; Engheta, N.; Polman, A. Experimental realization of an epsilon-near-zero metamaterial at visible wavelengths. *Nat. Photonics* **2013**, 7, 907-912.
92. Wurtz, G. A.; Pollard, R.; Hendren, W.; Wiederrecht, G. P.; Gosztola, D. J.; Podolskiy, V. A.; Zayats, A. V. Designed ultrafast optical nonlinearity in a plasmonic nanorod metamaterial enhanced by nonlocality. *Nat. Nanotechnol.* **2011**, 6, 106-110.
93. Darabi, A.; Zareei, A.; Alam, M. R.; Leamy, M. J. Experimental demonstration of an ultrabroadband nonlinear cloak for flexural waves. *Phys. Rev. Lett.* **2018**, 121, 174301-5.
94. Abdollahramezani, S.; Arik, K.; Farajollahi, S.; Khavasi, A.; Kavehvash, Z. Beam manipulating by gate-tunable graphene-based metasurfaces. *Opt. Lett.* **2015**, 40, 5383-5386.
95. Kang, L.; Rodrigues, S. P.; Taghinejad, M.; Lan, S. F.; Lee, K. T.; Liu, Y. M.; Werner, D. H.; Urbas, A.Cai, W. S. Preserving spin states upon reflection: Linear and nonlinear responses of a chiral meta-mirror. *Nano Lett.* **2017**, 17, 7102-7109.

96. Taghinejad, M.; Taghinejad, H.; Xu, Z.; Lee, K. T.; Rodrigues, S. P.; Yan, J. H.; Adibi, A.; Lian, T.; Cai, W. Ultrafast control of phase and polarization of light expedited by hot-electron transfer. *Nano Lett.* **2018**, 18, 5544-5551.
97. Yang, Y. M.; Kelley, K.; Sachet, E.; Campione, S.; Luk, T. S.; Maria, J. P.; Sinclair, M. B.; Brener, I. Femtosecond optical polarization switching using a cadmium oxide-based perfect absorber. *Nat. Photonics* **2017**, 11, 390-396.
98. Abdollahramezani, S., Hemmatyar, O., Taghinejad, H., Krasnok, A., Kiarashinejad, Y., Zandehshahvar, M., Alù, A., and Adibi, A. (2020). Tunable nanophotonics enabled by chalcogenide phase-change materials. Nanophotonics 9, 5, 1189-1241
99. Taghinejad, H., Abdollahramezani, S., Eftekhar, A.A., Fan, T., Hosseinnia, A.H., Hemmatyar, O., Dorche, A.E., Gallmon, A. and Adibi, A., 2020. ITO-Based $\mu $-Heaters for Multi-Stage Switching of Phase-Change Materials: Towards Beyond-Binary Reconfigurable Integrated Photonics. arXiv preprint arXiv:2003.04097.
100. Abdollahramezani, S., Hemmatyar, O., Taghinejad, M., Taghinejad, H., Kiarashinejad, Y., Zandehshahvar, M., Fan, T., Deshmukh, S., Eftekhar, A.A., Cai, W., Pop, E., El-Sayed, M., and Adibi, A., 2020. Dynamic hybrid metasurfaces. arXiv preprint arXiv:2008.03905.
101. Abdollahramezani, S., Taghinejad, H., Fan, T., Kiarashinejad, Y., Eftekhar, A.A. and Adibi, A., 2018. Reconfigurable multifunctional metasurfaces employing hybrid phase-change plasmonic architecture. arXiv preprint arXiv:1809.08907.
102. Hemmatyar, O., Abdollahramezani, S., Kiarashinejad, Y., Zandehshahvar, M. and Adibi, A., 2019. Full color generation with fano-type resonant HfO 2 nanopillars designed by a deep-learning approach. Nanoscale, 11(44), pp.21266-21274.
103. Abdolahad, M.; Taghinejad, H.; Saeidi, A.; Taghinejad, M.; Janmaleki, M.; Mohajerzadeh, S. Cell membrane electrical charge investigations by silicon nanowires incorporated field effect transistor (SiNWFET) suitable in cancer research. RSC Adv. 4, 7425-7431 (2014).
104. Abdolahad, M.; Mohajerzadeh, S.; Janmaleki, M.; Taghinejad, H.; Taghinejad, M. Evaluation of the shear force of single cancer cells by vertically aligned carbon nanotubes suitable for metastasis diagnosis. Integr. Biol. 5, 535–542 (2013).
105. Abdolahad, M.; Saeidi, A.; Janmaleki, M.; Mashinchian, O.; Taghinejad, M.; Taghinejad, H.; Azimi, S.; Mahmoudi, M.; Mohajerzadeh, S. A single-cell correlative nanoelectromechanosensing approach to detect cancerous transformation: monitoring the function of F-actin microfilaments in the modulation of the ion channel activity. *Nanoscale* **7**, 1879-1887 (2015).
106. Abdollahramezani, S.; Chizari, A.; Dorche, A. E.; Jamali, M. V.; Salehi, J. A. Dielectric metasurfaces solve differential and integro-differential equations. *Optics Letters* **42**, 1197-1200 (2017).
107. Chizari, A.; Abdollahramezani, S.; Jamali, M. V.; Salehi, J. A. Analog optical computing based on a dielectric meta-reflect array. *Optics Letters* **41**, 3451-3454 (2016).
108. Arik, K.; Abdollahramezani, S.; Farajollahi, S.; Khavasi, A.; Rejaei, B. Design of mid-infrared ultra-wideband metallic absorber based on circuit theory. Opt Commun 381, 309-313 (2016).
109. Hemmatyar, O.; Rahmani, B.; Bagheri, A.; Khavasi, A. Phase Resonance Tuning and Multi-Band Absorption Via Graphene-Covered Compound Metallic Gratings. *IEEE J. Quantum Elect.* **53**, (2017).
110. Zareei, Ahmad, et al. "Continuous profile flexural GRIN lens: Focusing and harvesting flexural waves." Applied Physics Letters 112, 023901 (2018).

111. Darabi, Amir, et al. "Experimental demonstration of an ultrabroadband nonlinear cloak for flexural waves." Physical review letters 121, 174301 (2018).
112. Darabi, Amir, and Michael J. Leamy. "Analysis and experimental verification of multiple scattering of acoustoelastic waves in thin plates for enhanced energy harvesting." Smart Materials and Structures 26, 085015 (2017).
113. Darabi, Amir, et al. "Broadband bending of flexural waves: acoustic shapes and patterns." Scientific reports 8.1 (2018): 1-7.
114. Darabi, Amir, Massimo Ruzzene, and Michael J. Leamy. "Piezoelectric T-matrix approach and multiple scattering of electroacoustic waves in thin plates." Smart Materials and Structures 26.12 (2017): 125018.
115. Darabi, A., Fang, L., Mojahed, A., Fronk, M. D., Vakakis, A. F., & Leamy, M. J. (2019). Broadband passive nonlinear acoustic diode. Physical Review B, 99(21), 214305.
116. Darabi, Amir, and Michael J. Leamy. "Tunable nonlinear topological insulator for acoustic waves." Physical Review Applied 12.4 (2019): 044030.
117. Darabi, Amir, Manuel Collet, and Michael J. Leamy. "Experimental realization of a reconfigurable electroacoustic topological insulator." Proceedings of the National Academy of Sciences 117.28 (2020): 16138-16142.
118. Darabi, A., Ni, X., Leamy, M., & Alù, A. (2020). Reconfigurable Floquet elastodynamic topological insulator based on synthetic angular momentum bias. Science Advances, 6(29), eaba8656.
119. Darabi, A., & Leamy, M. J. (2019). Reconfigurable topological insulator for elastic waves. The Journal of the Acoustical Society of America, 146(1), 773-781.

CHAPTER 2. SUBRADIANT AND TUNABLE PLASMONIC RESONANCE MODES

In plasmonic systems, hot electrons are generated via the nonradiative decay of plasmons. However, the nonradiative decay channel is not the only path for the extraction of the stored electromagnetic energy in plasmonic resonators. In fact, the radiation of electromagnetic waves, due to the oscillation of the electric dipoles, provides a second loss channel in plasmonic systems, as a consequence of which, a large portion of plasmons cannot be used for the generation of hot carriers. Therefore, it is essential to devise plasmonic platforms that facilitate the suppression of the radiation loss and preserve the energy of plasmons for the hot carrier generation. In addition, the possibility of tuning the resonance wavelength in plasmonic systems could provide a degree of freedom to control the energy of plasmonic hot carriers and create customized media with compelling optical properties for optimized light-mater interactions. The diversity of available metals and the variety of design architectures provide a rich portfolio for statically controlling the resonance lineshape. However, dynamic tuning of resonance attributes (e.g., the resonance wavelength and linewidth) are yet to be more expanded, especially when a narrow resonance linewidth is on demand. In this chapter, using a plasmonic nanopatch array, we design and experimentally demonstrate sharp plasmonic crystal (PC) resonances with full-width at half-maximum (FWHM) of only ~ 6 nm, dynamically tunable over a wide spectral range of 230 nm. The combination of angle-resolved ellipsometry and full-wave simulations shows that diffractive coupling of out-of-plane electric dipoles is the principal contributor in the formation of such sharp PC resonances. In addition, the designed nanopatch PC

supports a plasmonic Fabry-Pérot-like resonance that can be interfered with the PC resonance to generate complex Fano-type lineshapes. The co-existence of tunable resonance features renders our structure as a rich platform for applications seeking enhanced light-matter interactions based on the generation and transport of hot electrons.

2.1 Background, Motivation, and Design of Plasmonic Structure

The localization of light and the enhancement of optical-field-intensity are critical for applications demanding a strong light-matter interaction. For this purpose, optical lenses and dielectric cavities, as two major components of traditional photonics technology, have been extensively utilized. However, optical diffraction limits the domain in which photonic elements can be practically influential. Metallic nanoresonators have the distinct capability to overcome the diffraction limit by leveraging the coherent oscillation of free electrons, known as the localized plasmon resonance (LPR).[1-4] The great diversity of plasmonic metals to choose from and geometries to implement hold a great potential for the design of plasmonic structures working over a wide spectral range with desired spatial field profiles. Surface enhanced Raman spectroscopy (SERS),[5-7] nonlinear optics,[8-9] and refractive index sensing [10-12] are areas experiencing an exceptional growth following the development of plasmonics. However, the fast dephasing time τ_c (2-10 fs) [13-15] assigns an intrinsically-broad spectral linewidth, $\Gamma = 2\hbar\tau_c^{-1}$(> 50 nm),[13] to LPRs that reduces the quality factor of plasmonic nanoresonators. Radiation loss (coupling of the plasmons to far-field photons) and Ohmic loss (absorption of the plasmons by either d-band valance or sp-band conduction electrons) are the two major phenomena contributing to the fast dephasing of LPRs.

Several practical strategies for loss management in plasmonic resonators have been pursued. One approach is to utilize dark plasmonic modes, featuring a damped net electric-dipole-moment that weakly couples to the far-field photons.[16-21] Therefore, the suppression of the radiation loss (in dark modes) assists free electrons to carry on long-lived coherent oscillations and accommodate more energy in the small mode volume of plasmonic resonators. Fano-interference is another phenomenon widely employed to terminate loss channels. In plasmonic systems, Fano lineshapes form upon the interaction of two spectrally close resonances: a broad resonance generated by a lossy mode and a sharp resonance generated by a non-radiative mode.[22-25] Previous studies have shown that the interference of dark subradiant and bright superradiant modes results in Fano-like lineshapes with narrow spectral linewidths and strong spatial field-confinements.[22, 26-28] From a different perspective, PCs, owing to the simultaneous reduction of the radiative and Ohmic losses, have attracted a growing attention lately. PCs take the advantage of in-plane dipolar diffractive coupling of scattered light from the crystal,[29-32] providing narrow resonances at wavelengths approaching inter-particle distances in periodic arrays. In PCs, the interference pathway relies primarily on the phase difference between the scattered light from nano-objects within the array to eliminate the radiation loss independent of the LPR wavelength. This phenomenon was first reported as Wood's anomaly and later was explained as the transition of a grating mode from an evanescent state to a radiative state.[33-34] Footprints of PCs can be observed in the demonstration of plasmonic circuits,[35] demultiplexers and multiport systems,[36] nanolasers,[37] transparency at the terahertz regime [38], and etc. However, the homogeneity of the dielectric environment is a necessity that significantly influences the efficiency of the diffractive coupling and sets limitation on

the practically-achievable quality factor using PCs.[32, 39] Besides, the narrow spectral response of the PCs challenges strong coupling of such modes to the surrounding electromagnetic environments at desired wavelengths. Therefore, dynamic tuning of the lineshape and the resonance wavelength of the PC modes is a crucial step to exploit the promising potential of PCs.

In this study, we demonstrate exceptionally narrow plasmonic crystal resonances (FWHM ≈ 6 nm) in which the resonance wavelength is dynamically tuned over a broad wavelength range of 230 nm, via controlling the angle of incidence in an oblique excitation. Our proposed structure is a periodic nanopatch array comprised of 30 nm-thick gold (Au) nanopatches separated from a backside Au film by an 8 nm-thick alumina (Al_2O_3) film. Angle-resolved spectroscopic ellipsometry combined with full-wave simulations confirms that the interplay of the generated out-of-plane dipoles inside the Au nanopatches and the induced image dipoles inside the backside Au film plays a primary role in formation of the narrow and tunable resonance mode. In addition, we demonstrate the formation of a more complex lineshape with the characteristics of asymmetric Fano resonances through the interference of the PC mode and a Fabry-Pérot (FP)-like plasmonic resonance mode localized beneath the nanopatch elements.

As shown in Figure 7a-b, our designed plasmonic nanopatch crystals are made of a metal film coupled to an array of metallic nanopatches via a thin dielectric spacer. For the fabrication of such samples, we start with the electron beam evaporation of 10 nm/150 nm Ti/Au films on a silicon substrate, followed by the atomic layer deposition of 8 nm-thick Al_2O_3, to achieve a uniform spacer layer. We then integrate metallic nanoparticles on the spacer layer in a three-step fabrication process: (i) standard electron beam lithography for

the definition of nanopatterns, (ii) electron beam evaporation of 2 nm/28 nm Ti/Au metals, and (iii) a lift-off step in acetone for resolving the plasmonic crystal array. To measure the reflection and dark-field spectra of the fabricated plasmonic arrays, under normal excitations, a Craic QDI 202 UV-vis microspectrophotometer on a Leica DM 4000M microscope is employed. The light source used for these measurements is a tungsten halogen lamp with an unpolarized emission, ranging from 400 to 1000 nm. These measurements allow for exploring the FP resonance mode of nanopatch crystals. However, as will be discussed later, the excitation of PC modes requires the illumination of samples under oblique excitations. Therefore, we use a Woollam M-2000 ellipsometer in the reflection mode to carry out angle-resolved measurements. In the utilized system, a broadband (245 – 1690 nm) circularly polarized light excites samples at a wide range of excitation angle ($45° < \theta < 75°$, 2°-stepsize). Changes in the polarization and intensity of light, as it reflects from the PCs, are recorded in terms of $\Psi - \Delta$ values and using the ellipsometry equation $\rho = \frac{R_{TM}^{\theta}}{R_{TE}^{\theta}} = |\tan(\Psi)|^2$ we interpret the acquired data. To make sure that optics of our ellipsometer system does not affect optical reflection spectra, we use two different lenses with numerical apertures of ~ 0.1 and 0.5 on the illumination and detection arms of the ellipsometer, respectively.

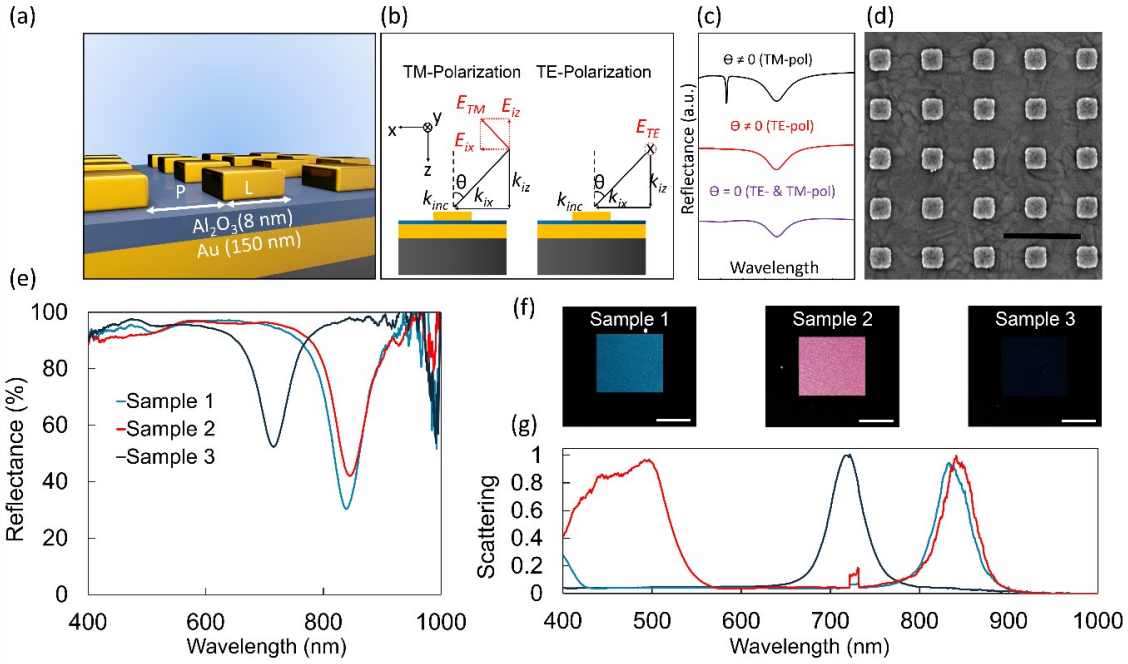

Figure 7: Overview of the PCs studied in this work, designation of polarization states, and optical characterizations at the normal AOI ($\theta = 0^{o}$). (a) The schematic representation of the two-dimensional gold nanopatch array. (b) In-plane and out-of plane electric-field components of the excitation wave and designation of TM- and TE-polarized light in the plane of incidence (i.e., x-z plane). (c) The schematic representation of the optical response obtained from the sample at different AOIs and polarization states. The sharp resonance at short wavelengths represents the PC mode and the broad resonance at long wavelengths represents the FP mode. (d) A representative SEM micrograph of the fabricated samples (the scale bar is 500 nm). (e) Measured bright-field optical reflection spectra of three PCs. Samples 1, 2, and 3 demonstrate resonances at λ_{FP} = 839, 844, and 715 nm, respectively. (f) Dark-field optical images of the three fabricated samples (scale bars are 100 μm). (g) Normalized dark-field scattering spectra of the PCs. Samples 1 and 2 scatter light at short wavelengths, in accordance with the first order reflective grating modes of these arrays. The sharp features around 720nm in pannel (g) are the artifacts of the spectrometer.

2.2 Numerical Modeling and Resonance Mode Analysis

This structure supports a localized FP mode and a PC mode that can only be observed under oblique excitations (Figure 7c). These two resonances can be "statistically"

tuned (independent of each other) via designing the geometrical dimensions of the proposed structure. However, in direct contrast to the FP mode, the PC mode can also be "dynamically" tuned via adjusting the incident angle under oblique excitations. Thus, we focus on the dynamic tuning of the PC mode via changing the angle of incidence (AOI, θ). We characterize three samples of different pitch (P) and nanopatch side length (L), which will be referred to as Sample 1 (L = 100 nm, P = 250 nm), Sample 2 (L = 100 nm, P = 350 nm), and Sample 3 (L = 75 nm, P = 250 nm) throughout this work. In all three samples, the thickness of the Au film, Al_2O_3 spacer, and Au nanopatches is 150 nm, 8 nm, and 30 nm, respectively. Figure 7d shows a scanning electron (SEM) micrograph of a representative sample. To identify the FP modes of each sample, we performed bright-field optical reflection spectroscopy (Figure 7e) at a normal AOI (i.e., $\theta = 0^o$) by routing an incoherent white light beam through a 50X objective (NA: 0.5) on the arrays. Then, the reflected light was collected using the same objective lens and guided to a commercial spectrometer via a multimode optical fiber. The suppressed reflection of light at λ_{FP} = 839, 844, and 715 nm shows the coupling of the excitation light to the fundamental plasmonic-FP mode of samples 1-3, respectively. As we will discuss in the following section, this mode is localized underneath the Au nanopatches. Indeed, the spatial proximity of the Au nanopatches and the backside Au film intensifies the local electric-field within the spacer layer, which in turn increases the effective refractive index, particularly at the edges of the nanopatches. The induced refractive index contrast causes reflection of the propagating waves underneath the nanopatches and leads into the formation of a FP-like nano-plasmonic cavity with a standing-wave nature.[40-41] In Figure 1e, we do not observe any narrow resonance within the 400 - 1000 nm wavelength range (limited by the spectrometer)

under the normal excitation angle. In addition, we explore the possibility of observing reflective (lossy) grating modes in all of the three samples using dark-field optical characterizations (Figure 7f-g). Results confirm that none of the samples possess reflective grating modes above 565 nm wavelength. Thus, we use the spectral interval between the grating modes and the FP mode for demonstration of the narrow PC modes. The weak rise in the scattering spectrum of Sample 1 and the broad peak in that of Sample 2 at the short wavelengths originate from the first-order grating modes of the associated arrays, consistent with the dark-field optical images of the samples presented in Figure 7f. Note that, because of the highly reflective nature of the samples at off-resonance wavelengths, bright-field optical reflection spectroscopy cannot be practiced to identify grating modes.

We proceed with the polarization-dependent near-/far-field simulation of the nanopatch arrays, at varying AOIs to set the ground for the theoretical and experimental demonstration of tunable PC modes. To do so, we perform three-dimensional finite-difference time-domain (FDTD) simulations using Lumerical simulation package in which TM- and TE-polarized plane waves are used to excite the nanopatch array (see Figure 7b for the designation of polarization states). In these simulations, the sample (geometrically identical to Sample 1) is excited at several AOIs and optical reflections are calculated over a spectral range spanning from 400 to 1000 nm. Figure 8a illustrates the calculated optical reflection spectra of Sample 1 under the TM-polarized excitation, R_{θ}^{TM}, in which two spectrally separate resonances can be identified. The resonances at shorter wavelengths are characterized as the diffractive coupling of scattered light from the individual nanopatches (i.e., the PC resonance), manifesting the suppressed reflection of light at angle-dependent wavelengths of λ_{PC}s. Upon increasing θ, coupling efficiency to the PC mode significantly

increases at larger $\lambda_{PC}s$ so that extremely narrow resonance linewidths emerge at angles larger than 45°. However, the second resonance at longer wavelengths, which is the FP resonance mode of the nanopatch array (at λ_{FP}), undergoes minor changes upon increasing θ. In striking contrast to the TM polarization, the TE-polarized light fails to excite the sharp PC resonance, as shown in calculated R_θ^{TE} spectra in Figure 8b. The strikingly different optical response of the PC structure under the TM and TE polarizations can be explained based on electric-field components of the excitation waves (as depicted in Figure 7b). Under the TM polarization, the out-of-plane component of the incident electric-field E_{iz}, excites an out-of-plane electric dipole within the nanopatches that leads to the resonant coupling of the incident light to the PC mode. However, the absence of the E_{iz} component in the TE-polarized light prohibits the excitation of the PC modes, regardless of the incident angle. Note that the enhanced reflection of the grazing component of the incident light weakens absorption of light at λ_{FP}. To solidify preceding explanations, we compare the near-field optical response of the PC mode and that of the FP mode under the TM-polarized excitation. Figure 7Figure 8c-h shows electric-field intensity enhancement (IE) profiles monitored at λ_{PC} = 657 nm (panels c-e) and λ_{FP}= 831 nm (panels f-h) within x-z and x-y planes at θ = 60°. At λ_{PC}, the $\left|\frac{E_z}{E_0}\right|^2$ component of the near-field profile (Figure 8d) is oriented along the z-direction and dominates the overall IE profile of the mode (Figure 8c), which verifies the out-of-plane dipolar nature of the PC resonance. In addition, as shown in Figure 8e, the enhanced field intensity across the x-y plane (i.e., the plane of the array) confirms the formation of an in-plane crystal mode via the near-field interaction of the out-of-plane dipoles. A similar analysis at λ_{FP} shows that $\left|\frac{E_z}{E_0}\right|^2$ (Figure 8g) also dominates the

overall IE profile (Figure 8f) but in this case the electric-field is primarily confined underneath the nanopatches within the spacer layer, implying the in-plane (x-direction) nature of the dipoles generating the FP-like resonance mode. As an inherent behavior of the on-resonance-excited FP cavities, light is spatially concentrated at the vicinity of the nanopatches as shown in the x-y plane near-field profile in Figure 8h, in contrast to that of the PC mode. We repeated previous simulations at various angles (not shown here) and verified that changing θ only influences the spectral location of λ_{PC} and IE of the mode, while the nature of the resonance at λ_{PC} and λ_{FP} remains identical to those presented in Figure 8. An interesting aspect of our designed plasmonic nanopatch array is the strong spatial overlap between the field profiles of the PC and FP modes, particularly inside the spacer layer. This feature makes the nanopatch array an ideal candidate for applications seeking strong light-matter interactions,[42-45] including plasmonic nanolasers and nonlinear optical processes, by simply replacing the Al_2O_3 with gain media or a nonlinear optical material. It is important to notice that the formation of such crystal resonance modes in plasmonic systems allows for achieving a sub-diffraction limit mode volume, a feature that is not within our reach using photonic crystal systems.[46] Moreover, since the LP mode is essentially subradiant, the on-resonance excitation of the device at λ_{LP} leads into the generation of a dense hot electron population above the Fermi level of Au. Therefore, utilizing good electron acceptor materials such as TiO2, silicon, and ITO as the spacer layer in the design of the plasmonic crystal, allows for the demonstration of hot-electron based functionalities.[47]

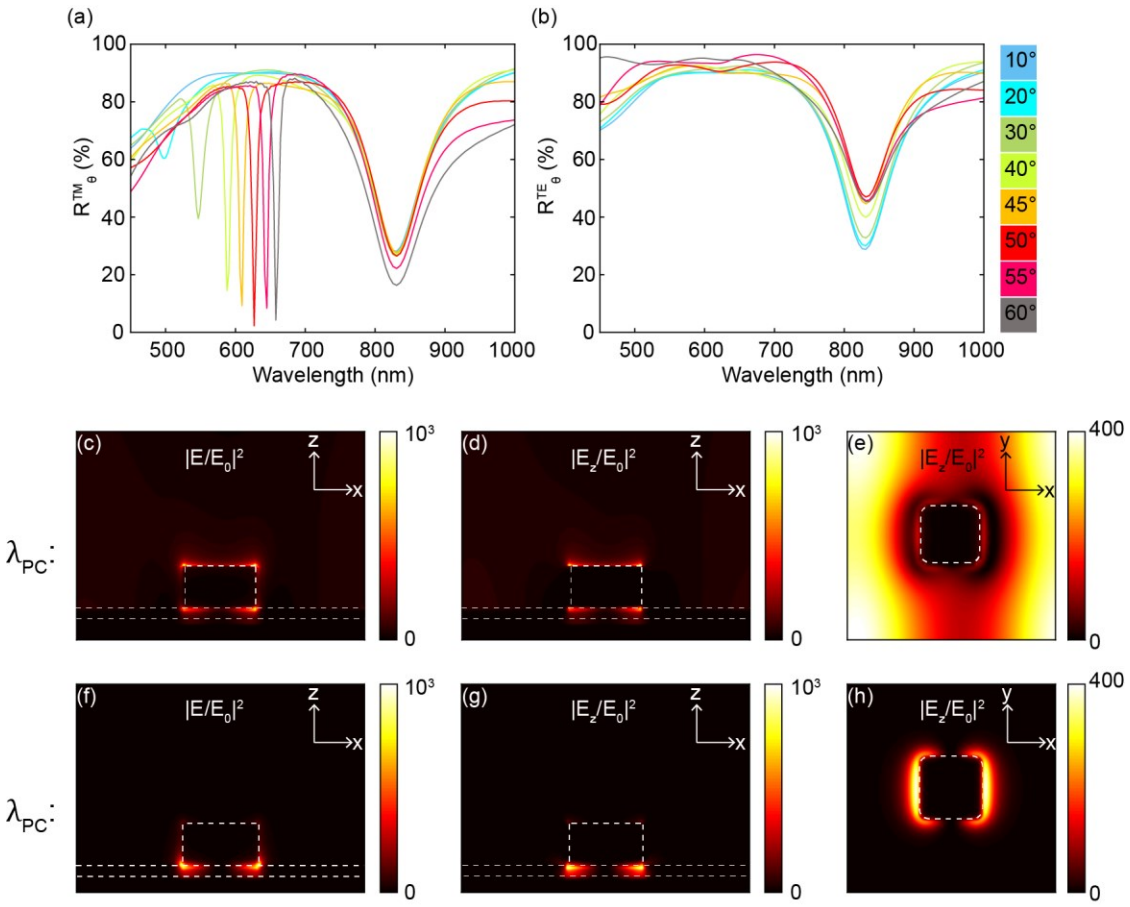

Figure 8: Full-wave numerical study of the angle-resolved and polarization-resolved near-/far-field response of the nanopatch plasmonic crystals. Angle-dependent reflection spectra under the (a) TM-polarized and (b) TE-polarized excitations. For the TM-polarized excitation, the set of sharp resonances at λ_{PC} is identified as the PC modes, while the TE-polarized excitation lacks such features. Color codes show the excitation angle. The arrows show direction of FP mode evolution by changing θ from 0° to 60°. (c-e) Electric-field intensity enhancement profiles projected on different planes as labeled on the figures (at θ = 60° and λ_{PC} = 657 nm). The z-component in panel (d) illustrates the out-of-plane dipolar nature of the PC mode. (e) The near-field response in the x-y plane (2 nm above the spacer layer) depicts the long-range non-vanishing field enhancement profile. (f-h) Electric-field intensity enhancement profiles similar to those of (c-e) but monitored at λ_{FP} = 831 nm, identified as the plasmonic FP resonance. Geometrical dimensions used in these simulations are identical to those of Sample 1.

2.3 Spectroscopic Ellipsometry Characterization of PC Modes

We proceed with the experimental demonstration of PC resonances utilizing spectroscopic ellipsometry carried out in a reflection mode. In these measurements, a broadband circularly-polarized (CP) light excites the array and a detector measures $\Psi - \Delta$ spectra of reflected light for $45° < \theta < 75°$ from which we calculate $\rho = \frac{R_\theta^{TM}}{R_\theta^{TE}}$. Figure 9 illustrates the measured ρ spectra for Sample 1, which offers the narrowest PC resonances. It is important to note that in the spectral range of 500-720 nm, where the PC resonances emerge, the ρ spectra imitate the characteristics of R_θ^{TM} because R_θ^{TE} has no resonance behavior (see Figure 8b) in this wavelength range (i.e., $\rho = \frac{R_\theta^{TM}}{R_\theta^{TE}} \approx R_\theta^{TM}$). Thus, spectroscopic ellipsometry can be used unambiguously for the characterization of the sharp PC resonances. The obtained ρ spectra at θ = 69°, 71°, and 73° reveal linewidths narrower than 6 nm, an order of magnitude narrower than the FWHM of most plasmonic systems reported to date. We note that efficient light scattering from nanostructures in periodic arrays is the primary step in the formation of narrow PC modes based on the out-of-plane dipolar coupling. To fulfill this condition, previous reports were restricted to the use of thick metallic nanostructures (> 100 nm).[27] However, we lift this limitation via incorporating the backside Au film into our design in which narrow lineshapes can be achieved using Au nanopatches of only 30 nm-thick. To verify this claim, we calculate the charge distribution profile within one unite cell of the array at λ_{PC} (Figure 9b). Results show that the excited out-of-plane dipole inside the Au nanopatch additively couples to the induced image dipole within the backside Au film, enabling efficient coupling of the incident light to the PC modes using very thin nanopatches. Such a dipolar coupling allows for damping the radiation loss and, therefore, achieving spectrally narrow PC resoance modes at angle

tunable λ_{PC}s. In sharp contrast, the calculated charge distribution at λ_{FP} (Figure 9d) manifests formation of an in-plane electric dipole within the Au nanopatch that is spatially oriented against the induced electric dipole within the backside Au film. Therefore, this resonance mode is more of a FP-like plasmonic resonance rather than a dipolar mode, as we discussed above. We also, fabricated a control sample in which the device geometry is similar to that of the Sample 1, except that the backside Au film is replaced with a thick alumina layer.

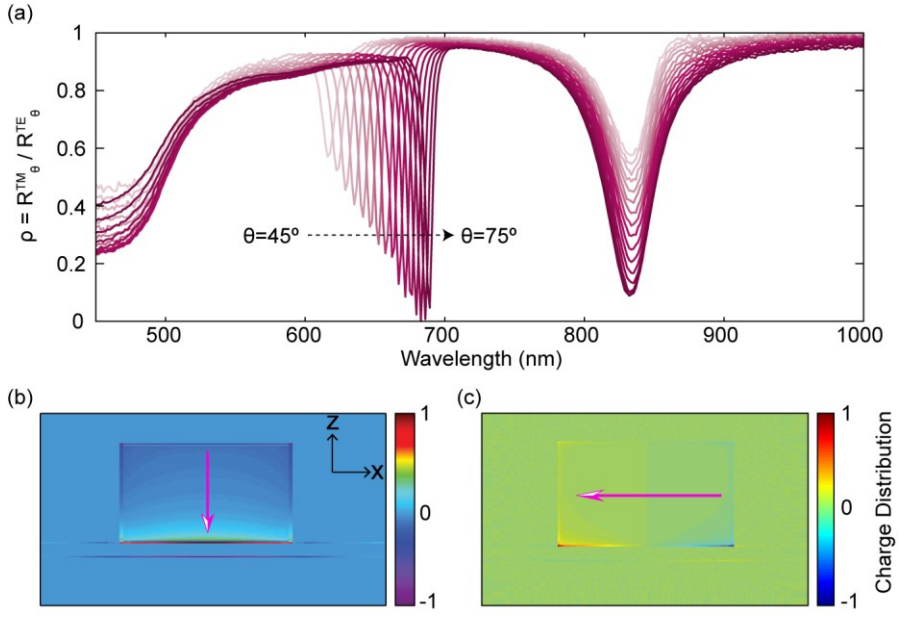

Figure 9: Experimental spectroscopic ellipsometry demonstration of sharp PC resonances. (a) The angle-dependent evolution of $\rho = \frac{R^{\theta}_{TM}}{R^{\theta}_{TE}}$ measured on Sample 1, when θ varies from 45° to 75° in steps of 2°. The redshift of the PC resonance mode and enhanced absorption of light are observed upon increasing the AOI. Calculated (normalized) charge distribution profiles at (b) λ_{PC} and (c) λ_{FP}, for θ = 65°. The orientations of the dipoles are outlined using arrows. The diffractive coupling of the out-of-plane electric dipoles within the Au nanopatches enables the formation of the PC mode. We use geometrical dimensions similar to Sample 1 for the calculation of charge distribution profiles.

In our structure, the lattice plasmon resonance wavelength depends on the excitation angle and the periodicity (d = L + P) of the array. Based on the Rayleigh formulation, [34] λ_{PC} is calculated using $\lambda_{PC}^{m} = \frac{d}{m}[n + Sin\theta]$, where m and n are the mode order and the refractive index of the environment (air or Al_2O_3), respectively. To verify consistency of our results with the Rayleigh formula, we fabricate three samples of different periodicity and experimentally measure the resonance wavelength of each sample at various excitation angles. As shown in Figure 10, the measured λ_{PC}s in all three samples match the predicted value by the Rayleigh formula (n and m are both set to one). This observation allows us to use the Rayleigh formula for calculation of the ultimate wavelength tuning range ($\Delta\lambda_{PC}$) beyond limitations imposed by our ellipsometry measurements (i.e., $45^{o} < \theta < 75^{o}$). For example, the expected tuning range provided in Sample 1 is estimated to be $\Delta\lambda_{PC}^{1} = \lambda_{PC}^{1}(\theta = 90°) - \lambda_{PC}^{1}(\theta = 20°) = 350\ (1\text{-}Sin20^{\circ}) \approx 230$ nm. Note that in this calculation $\theta = 20°$ is the smallest AOI at which the PC resonance can be excited (see Figure 8a).

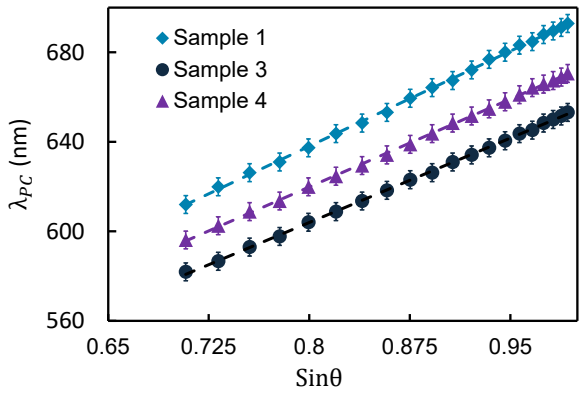

Figure 10: Comparison of the experimentally measured PC resonance wavelength with Rayleigh formula. The dashed lines represent the Rayleigh formula fitted to the experimentally extracted data (i.e., symbols) from samples 1, 3, and 4.

The narrow PC resonances demonstrated in this study should not be misinterpreted as two alternatively possible resonances that the nanopatch PC might support: (i) the surface plasmon (SP) resonance at the interface of the Au-film/Al_2O_3-spacer, momentum matched via the integrated nanopatch array or (ii) higher order FP modes, excited through the asymmetric excitation of the array. We rule out the first possibility because the identical in-plane lattice momenta of the TE- and the TM-polarized light should make the structure insensitive to the polarization of the excitation light, while our demonstrations reveal strong polarization-dependency of this resonance mode. However, the involvement of the SP mode in the coupling of light to the PlC mode is possible. The second possibility is also not credible as the resonance wavelength of the higher order FP modes primarily depend on the cavity length and the effective refractive index of the spacer layer. However, in our demonstrations variation of the AOI changes the spectral location of the resonance mode, while the cavity length and the refractive index of the spacer layer are invariant.

2.4 Tunable Fano-Like Resonance Modes

The presence of the two resonance modes, which are tunable either statically (both PC and FP modes) or dynamically (the PC mode), provides a rich platform for generation of more complex lineshapes that can be useful for varieties of applications. For instance, in SERS applications it is essential to design plasmonic structures that support two resonance modes with spectral proximity and spatial overlap (for the pump and Stoke's signals). For such a purpose, Fano lineshape has been extensively used,[26, 48] where interference of two resonances (e.g., subradiant and superradiant plasmonic modes) leads to the demonstration of the efficient SERS. Here, in a dedicated design (Sample 2 in Figure 7), we tune the in-plane crystal momentum of the plasmonic lattice so that the PC mode

spectrally interferes with the broad FP mode to form asymmetric Fano resonances (Figure 11a). Apparently, the AOI determines details of the interference lineshape via controlling the spectral location of the PC mode, which serves as a subradiant discrete state in the Fano scheme.[23, 25] In Figure 11a, existence of two dips and one peak is a general trend in all the measured spectra, the nature of which is explored using numerical simulations at several representative excitation angles (45°-55°) as depicted in Figure 11b-f. The enhancement of the overall electric-field and that of its z-component are shown, respectively, in Figure 11c, d at λ_{dip-1}= 780 nm (the narrow dip) and in Figure 5e, f at λ_{dip-2} = 849 nm (the broad dip), when polarization and AOI are set to TM and θ = 45°, respectively. At both λ_{dip-1} and λ_{dip-2} the enhancement of the z-component dominates the overall enhancement profiles, while the near-field behaviors at these two wavelengths are significantly different. At λ_{dip-1}, the near-field profile (Figure 11d) can be constructed by overlaying the individual profiles associated with the PC (Figure 8d) and the FP (Figure 8g) modes. At λ_{dip-2}, however, the broken symmetry of the near-field profile, with respect to the z-axis, rules out simple superposition of the two modes. This asymmetric field profile can be qualitatively explained based on the calculated induced electric dipoles and charge distribution inside the nanopatches as illustrated in Figure 11g. At λ_{dip-2}, the spectral vicinity of λ_{PC} and λ_{FP} allows the simultaneous excitation of the in-plane and out-of-plane dipoles, which leads to the formation of a tilted net electric dipole parallel with the overall excitation electric field and breaks the symmetry of the near-field response. Also, there is a resonance peak between λ_{dip-1} and λ_{dip-2} that originates from the constructive interference of the PC and FP modes, enhancing light reflection from the array. Since this

phenomenon occurs only for the TM polarization, the measured ρ spectra contains values larger than unity in a wavelength range between λ_{dip-1} and λ_{dip-2}.

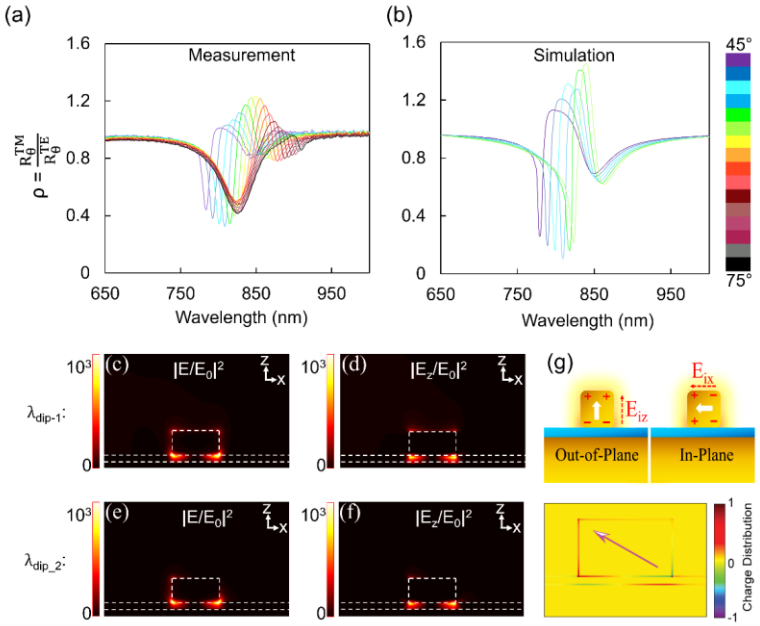

Figure 11: Demonstration of Fano lineshapes through the interference of the PC mode and the FP-cavity mode. (a) Spectroscopic ellipsometry measurement of $\rho = \frac{R_\theta^{TM}}{R_\theta^{TE}}$ on Sample 2 as θ (the color codes) varies from 45° to 75° in steps of 2°. The constructive Fano interference increases the light reflection from the sample leading to values larger than unity in ρ spectra. (b) Simulated ρ spectra for θ ranging from 45° to 55°, with step size of 2° (color codes in panels (a) and (b) are the same). The electric-field intensity enhancement profile projected into the x-z plane at θ =45°, when monitored at (c-d) λ_{dip-1}= 780 nm and (e-f) λ_{dip-2} = 849 nm. (g) The schematic (top panel) representation of the electric charge distribution and the induced dipoles in nanopatch elements explains the asymmetric origin of the calculated charge distribution. Geometrical dimensions used in these simulations are identical to those of Sample 2.

In conclusion, we experimentally demonstrated plasmonic resonances with extremely narrow linewidths (FWHM ≈ 6 nm)and thoeretically found that under oblique excitations , the out-of-plane dipoles of individual nanopatches couple within the plane of

the lattice, which enables formation of a plasmonic crystal resonance. The AOI was leveraged for precise tuning of the resonance wavelength over a large spectral range. The exceptionally sharp PC resonances were established in only 30 nm-thick nanopatches by taking advantage of the strong interaction between the excited out-of-plane dipoles within the nanopatches and the induced image dipoles within the backside Au film. In addition, asymmetric Fano lineshapes were generated via the interference of the PC modes and the localized FP-like resonance mode of the nanopatch crystal. The device architecture exploited here (i.e., Au-nanopatch/dielectric-spacer/Au-film stack) holds great promises for applications ranging from strong light-matter interactions (e.g., harmonic generation, SERS, plasmonic lasing, and photoluminescence enhancement) to optical signal processing.

2.5 References

[1] J. A. Schuller, E. S. Barnard, W. S. Cai, Y. C. Jun, J. S. White, M. L. Brongersma, Nat Mater 2010, 9.

[2] E. Ozbay, Science 2006, 311, 189.

[3] N. Fang, H. Lee, C. Sun, X. Zhang, Science 2005, 308, 534.

[4] X. Zhang, Z. W. Liu, Nat Mater 2008, 7, 435.

[5] H. Ko, S. Singamaneni, V. V. Tsukruk, Small 2008, 4, 1576.

[6] E. C. Le Ru, P. G. Etchegoin, Principles of Surface-Enhanced Raman Spectroscopy: And Related Plasmonic Effects 2009, Xvii.

[7] B. Nikoobakht, J. P. Wang, M. A. El-Sayed, Chem Phys Lett 2002, 366, 17.

[8] M. Kauranen, A. V. Zayats, Nat Photonics 2012, 6, 737.

[9] J. Butet, P. F. Brevet, O. J. F. Martin, Acs Nano 2015, 9, 10545.

[10] J. Homola, S. S. Yee, G. Gauglitz, Sensor Actuat B-Chem 1999, 54, 3.

[11] K. S. Lee, M. A. El-Sayed, J Phys Chem B 2006, 110, 19220.

[12] N. Liu, M. Mesch, T. Weiss, M. Hentschel, H. Giessen, Nano Lett 2010, 10, 2342.

[13] H. Baida, D. Mongin, D. Christofilos, G. Bachelier, A. Crut, P. Maioli, N. Del Fatti, F. Vallee, Phys Rev Lett 2011, 107.

[14] S. Link, M. A. El-Sayed, J Phys Chem B 1999, 103, 8410.

[15] C. Sonnichsen, T. Franzl, T. Wilk, G. von Plessen, J. Feldmann, O. Wilson, P. Mulvaney, Phys Rev Lett 2002, 88.

[16] S. A. Maier, Nat Mater 2009, 8, 699.

[17] F. P. Schmidt, H. Ditlbacher, U. Hohenester, A. Hohenau, F. Hofer, J. R. Krenn, Nano Lett 2012, 12, 5780.

[18] H. Wang, Y. P. Wu, B. Lassiter, C. L. Nehl, J. H. Hafner, P. Nordlander, N. J. Halas, P Natl Acad Sci USA 2006, 103, 10856.

[19] J. B. Khurgin, Nat Nanotechnol 2015, 10, 2.

[20] V. Giannini, G. Vecchi, J. G. Rivas, Phys Rev Lett 2010, 105.

[21] J. Marae-Djouda, R. Caputo, N. Mahi, G. Leveque, A. Akjouj, P. M. Adam, T. Maurer, Nanophotonics-Berlin 2017, 6, 279.

[22] B. Luk'yanchuk, N. I. Zheludev, S. A. Maier, N. J. Halas, P. Nordlander, H. Giessen, C. T. Chong, Nat Mater 2010, 9, 707.

[23] B. Gallinet, O. J. F. Martin, Acs Nano 2011, 5, 8999.

[24] Y. Francescato, V. Giannini, S. A. Maier, Acs Nano 2012, 6, 1830.

[25] V. Giannini, Y. Francescato, H. Amrania, C. C. Phillips, S. A. Maier, Nano Lett 2011, 11, 2835.

[26] F. Hao, P. Nordlander, Y. Sonnefraud, P. Van Dorpe, S. A. Maier, Acs Nano 2009, 3, 643.

[27] W. Zhou, T. W. Odom, Nat Nanotechnol 2011, 6, 423.

[28] A. Christ, Y. Ekinci, H. H. Solak, N. A. Gippius, S. G. Tikhodeev, O. J. F. Martin, Phys Rev B 2007, 76.

[29] E. M. Hicks, S. L. Zou, G. C. Schatz, K. G. Spears, R. P. Van Duyne, L. Gunnarsson, T. Rindzevicius, B. Kasemo, M. Kall, Nano Lett 2005, 5, 1065.

[30] G. Vecchi, V. Giannini, J. G. Rivas, Phys Rev B 2009, 80.

[31] B. Lamprecht, G. Schider, R. T. Lechner, H. Ditlbacher, J. R. Krenn, A. Leitner, F. R. Aussenegg, Phys Rev Lett 2000, 84, 4721.

[32] B. Auguie, W. L. Barnes, Phys Rev Lett 2008, 101.

[33] M. Meier, A. Wokaun, P. F. Liao, J Opt Soc Am B 1985, 2, 931.

[34] Rayleigh, P R Soc Lond a-Conta 1907, 79, 399.

[35] W. F. Andress, H. Yoon, K. Y. M. Yeung, L. Qin, K. West, L. Pfeiffer, D. Ham, Nano Lett 2012, 12, 2272.

[36] A. Drezet, D. Koller, A. Hohenau, A. Leitner, F. R. Aussenegg, J. R. Krenn, Nano Lett 2007, 7, 1697.

[37] W. Zhou, M. Dridi, J. Y. Suh, C. H. Kim, D. T. Co, M. R. Wasielewski, G. C. Schatz, T. W. Odom, Nat Nanotechnol 2013, 8, 506.

[38] G. C. Dyer, G. R. Aizin, S. J. Allen, A. D. Grine, D. Bethke, J. L. Reno, E. A. Shaner, Nat Photonics 2013, 7, 925.

[39] G. Vecchi, V. Giannini, J. G. Rivas, Phys Rev Lett 2009, 102.

[40] A. Moreau, C. Ciraci, J. J. Mock, R. T. Hill, Q. Wang, B. J. Wiley, A. Chilkoti, D. R. Smith, Nature 2012, 492, 86.

[41] J. B. Lassiter, F. McGuire, J. J. Mock, C. Ciraci, R. T. Hill, B. J. Wiley, A. Chilkoti, D. R. Smith, Nano Lett 2013, 13, 5866.

[42] H. Taghinejad, M. Taghinejad, A. Tarasov, M. Y. Tsai, A. H. Hosseinnia, H. Moradinejad, P. M. Campbell, A. A. Eftekhar, E. M. Vogel, A. Adibi, Acs Photonics 2016, 3, 700.

[43] M. Taghinejad, H. Taghinejad, M. Ganji, A. Rostamian, S. Mohajerzadeh, M. Abdolahad, M. Kolahdouz, Ieee T Electron Dev 2014, 61, 3239.

[44] M. L. Andersen, S. Stobbe, A. S. Sorensen, P. Lodahl, Nat Phys 2011, 7, 215.

[45] H. Taghinejad, S. Hamed Shams-Mousavi, Y. Gong, M. Taghinejad, A. A. Eftekhar, P. Ajayan, A. Adibi, Plasmonics 2016.

[46] C. W. Hsu, B. Zhen, J. Lee, S. Chua, S. G. Johnson, J. D. Joannopoulos, M. Soljacic, Nature 2013, 499, 188.

[47] M. Taghinejad, H. Taghinejad, Z. Xu, Y. Liu, S. P. Rodrigues, K. T. Lee, T. Lian, A. Adibi, W. Cai, Adv Mater 2018, DOI: 10.1002/adma.201704915.

[48] J. Ye, F. F. Wen, H. Sobhani, J. B. Lassiter, P. Van Dorpe, P. Nordlander, N. J. Halas, Nano Lett 2012, 12, 1660.

CHAPTER 3. HOT-ELECTRON ENABLED FEMTOSECOND ALL-OPTICAL SWITCHING IN PLASMONICS

Hot-carrier induced phenomena in plasmonic systems represent an exciting current frontier in nanophotonics. The generation, transport, and extraction of such photoexcited carriers with energies greater than those at thermal equilibrium have enabled a wealth of physical and chemical processes. The highly interdisciplinary field of study has led to diverse applications for chemical catalysis, photothermal heating, photodetection, and energy conversion. The light-induced modification of the effective temperature and density of free electrons in the metal also facilitates all-optical modulation via optical Kerr nonlinearities. The modulation speed of this process in all prior demonstrations, however, is limited to a picosecond timescale, due to the intrinsically slow phonon-facilitated mechanisms for the thermalization of hot-electrons. The optical Kerr nonlinearity of plasmonic metals provides enticing prospects for developing reconfigurable and ultracompact all-optical modulators.[1-7] In nanostructured metals, the coherent coupling of light energy to plasmon resonances creates a nonequilibrium electron distribution at an elevated electron temperature that gives rise to significant Kerr optical nonlinearities.[8-12] Although enhanced nonlinear responses of metals facilitate the realization of efficient modulation devices, the intrinsically slow relaxation dynamics of the photoexcited carriers, primarily governed by electron-phonon interactions,[9,13-15] impedes ultrafast all-optical modulation. In this chapter, we demonstrate femtosecond all-optical modulation of light via the activation of electron-dominated relaxation pathways for hot-electrons. Both the relaxation kinetics and the optical nonlinearity can be actively tuned in rationally designed plasmonic

systems. Our finding has the potential to substantially expand the scope of hot-electron science and technology beyond the conventional photovoltaics and photocatalysis, and find application in nonlinear optical processes with a femtosecond-scale response time. We will see that both the relaxation kinetics and the optical nonlinearity can be actively tuned by leveraging the spectral response of the plasmonic devices in the linear regime. Our findings offer an opportunity to exploit hot-electron induced nonlinearities for design of self-contained, ultrafast, and low-power all-optical switches based on plasmonic platforms.

3.1 Background, Motivation, and Design of Plasmonic Structure

The term 'hot-electron' is frequently used in the literature to describe electrons in a solid with energies greater than those thermally excited at ambient temperature.[16-18] As we discussed in Chapter 1, in nanostructured metals, hot-electrons are primarily generated by the decay of localized surface plasmons through several competing nonradiative processes including the interband and the phonon-assisted intraband electronic transitions.[19-22] Internal thermalization of the plasmonically induced carriers via electron-electron interactions, however, distributes the absorbed light energy among all free carriers in the conduction band of the metal, creating a population of electrons with an elevated effective temperature. The optical modification of the temperature and density of free carriers drastically alters dielectric permittivity of metals, as manifested by their strong Kerr-type optical nonlinearities, and enables plasmonic structures as self-sufficient active platforms for all-optical data processing confined to a miniaturized footprint.[1-4] Although the Kerr nonlinearity of metals can be exploited for the dynamic control of plasmonic responses, the slow energy transfer from thermalized electrons to the lattice, through the electron-phonon interaction, limits the modulation speed to a picosecond timescale.[9,13-14]

Indeed, the internal thermalization of hot-electrons constrains the relaxation dynamics to intrinsically slow phonon-facilitated mechanisms. In this chapter, we show that extraction of plasmonic hot-electrons from nanostructured metals triggers an electron-dominated relaxation channel, through which the equilibration of optically excited plasmonic systems occurs in an ultrafast femtosecond regime. For the experimental demonstration, we incorporate an electron acceptor material in a carefully designed plasmonic lattice that supports spectrally tunable lattice plasmon (LP) resonances with an extremely damped radiation loss. The on-resonance excitation of the plasmonic lattice drives the exchange of energetic hot-electrons at the interface of the plasmonic metal and the acceptor material, and enables all-optical modulation of the optical response in this plasmonic system with a femtosecond response time. Transient pump-probe measurements reveal that the relaxation kinetics and optical nonlinearity can be actively controlled by exploiting the sensitivity of the LP modes to the polarization of pump and probe signals.

The plasmonic lattice used in our study is composed of a square array of gold (Au) nanocubes (thickness: 40 nm, length: 100 nm, pitch: 250 nm) placed on an Au film separated by a 10 nm-thick ITO spacer **(**Figure 12a-b). The static optical response of the structure under a normal excitation angle, as illustrated in Figure 12c, stems from a Fabry-Pérot (FP)-like plasmonic resonance formed underneath the nanocubes. In fact, the spatial proximity of the nanocubes and the metal film leads to the formation of plasmonic hot spots and therefore, a large impedance mismatch around the nanocubes' edges. Multiple reflections of light from the edges enable the plasmonic FP mode within the spacer layer and suppress the light reflection from the structure, as indicated by the resonance dip at λ_{FP} = 870 nm.[23-24] In contrast, under oblique excitation at an incident angle θ, the in-plane

momentum of light adds up to that of the lattice, thereby facilitating the resonant coupling of light to a lattice plasmon (LP) mode. The excitation of the subradiant LP mode is manifested in angle-resolved spectroscopic ellipsometry spectra (Figure 12d) through the observation of angle-dependent resonances at λ_{LP}, which possesses substantially reduced resonance linewidths. In the ellipsometry spectra, the angular and polarization behaviors of the structure are evaluated by measuring $R_{TM}^{\theta}/R_{TE}^{\theta}$, where R_{TM}^{θ} and R_{TE}^{θ} are the reflection coefficients for TM- and TE-polarized incidence, respectively. Unlike the resonance wavelength λ_{FP}, which stays at a fixed spectral location insensitive to the angle of incidence, the λ_{LP} can be accurately tuned over a wide spectral range by adjusting θ as predicted by $\lambda_{LP} = d\,(\mathrm{Sin}\theta + 1)$,[25] where d is the lattice constant of the structure. Moreover, the ellipsometric study suggests strong sensitivity of the LP mode to the polarization of the incident light. This fact stems from the out-of-plane dipolar nature of the LP mode (as reported elsewhere [25]), whose excitation relies on the out-of-plane electric-field component of a TM-polarized light. The distinctive nature of the LP and FP modes is further revealed in the normalized near-field intensity profiles of the two modes as shown in Figure 12e, where the LP mode displays a spatially distributed profile while the FP mode is largely confined to the geometrical boundaries of the gold nanocubes. The collection of these optical properties renders the devised plasmonic lattice a rich platform for spectral and polarization resolved nonlinear optical processes, facilitated by the generation and injection of hot-carriers (insets of Figure 12a).

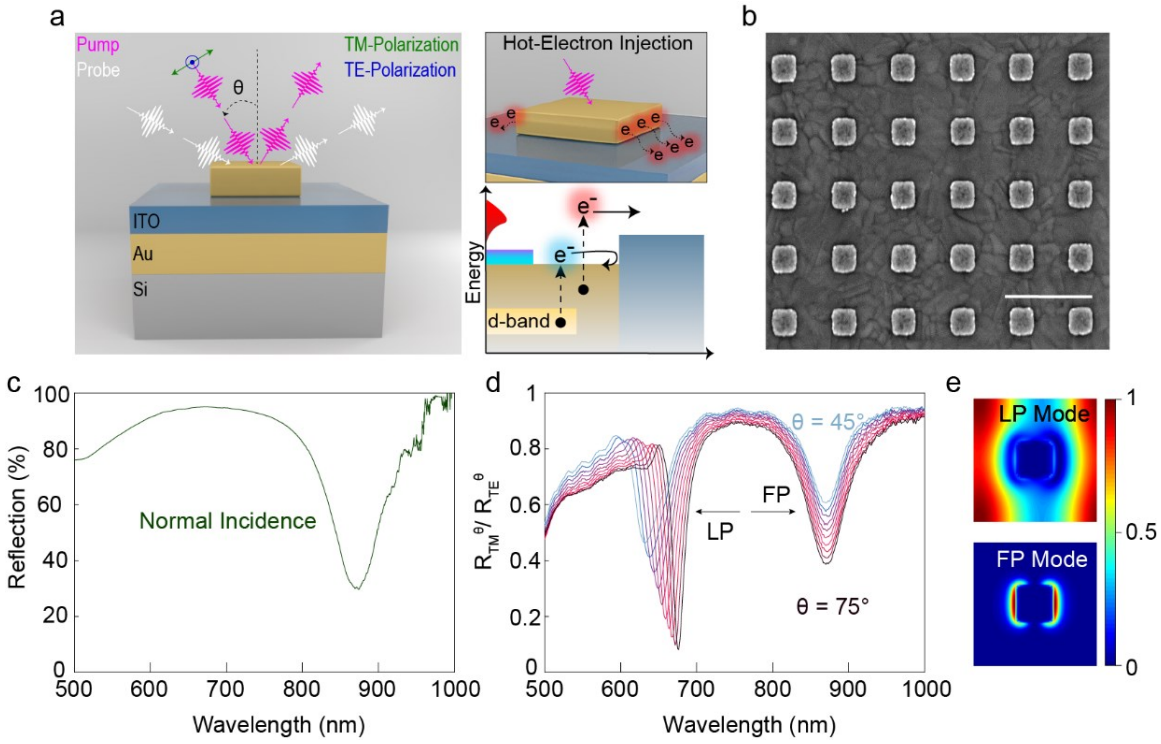

Figure 12: Plasmonic lattice, designation of polarization states, and static optical characterization. (a) Schematic of the plasmonic lattice and definition of the TM and TE polarizations with respect to the plane of incidence. In all the following measurements, the probe angle is 10° larger than the pump angle. The two insets schematically describe injection of hot-electrons from Au into the ITO layer. (b) A representative scanning electron microscope image of the fabricated device. The scale bar is 500 nm. (c) Measured reflectance spectrum of the plasmonic lattice under normal incidence. The resonance dip at 870 nm reveals the spectral location of the FP mode. (d) Spectroscopic ellipsometry of $R_{TM}^{\theta}/R_{TE}^{\theta}$, as θ varies from 45° to 75° with a step size of 2°. The angle-dependent LP resonances represent a reduced linewidth compared to the FP mode, especially at larger incident angles, originated from the reduced radiation loss thanks to the diffractive coupling of the scattered light from the Au nanocubes. (e) Normalized near-field intensity profiles calculated at λ_{LP} (top) and λ_{FP} (bottom) for θ = 65°.

3.2 All-Optical Modulation of Plasmons Based on Conventional Kerr Effect

To demonstrate the ultrafast all-optical modulation of light using the plasmonic lattice, we employ a femtosecond pump-probe transient spectroscopy technique, where the

pump (control) light modulates the optical reflection of a broadband probe (data) signal from the device. In these experiments, the pump induced transient reflection is characterized in terms of the change in the optical density $\Delta OD = \log_{10}(R_p/R_0)$, where R_0 and R_p are, respectively, the reflectance *before* and a *delay time (τ_d) after* the incidence of the pump light. Figure 13a-c illustrates transient response maps when the sample is probed with a TM-polarized signal at varied incident angles of $\theta_{probe} = 45°$, 55°, and 65°, respectively, and under excitation with a TM-polarized pump at $\lambda_{pump} = 500$ nm and a pulse duration of 150 fs. As spectral behavior in Figure 13d-f reveals, the maximum modulation is achieved at wavelengths around the plasmonic resonances, for both the λ_{FP} and the angle-dependent λ_{LP}, thanks to the enhanced sensitivity of these two modes to pump-induced changes in the permittivity (i.e., the optical Kerr nonlinearity) of gold. The observed transient lineshapes manifest a pump-induced redshift and a spectral broadening of the LP and the FP resonance modes. Moreover, the spectral location of the maximum modulation undergoes a blueshift upon increasing the pump energy. This effect originates from the inherent wavelength-dependent Kerr nonlinearity of gold, where the interband electronic transitions lead to a stronger modification of the permittivity and therefore, a more intensified pump-induced modulation, at shorter wavelengths. Nevertheless, we can achieve a greater ΔOD at a longer λ_{LP} (corresponding to a higher θ_{probe}) despite the weaker Kerr nonlinearity of Au at longer wavelengths as seen in Figure 13a-c, because of the considerable reduction in the linewidth of the LP modes.

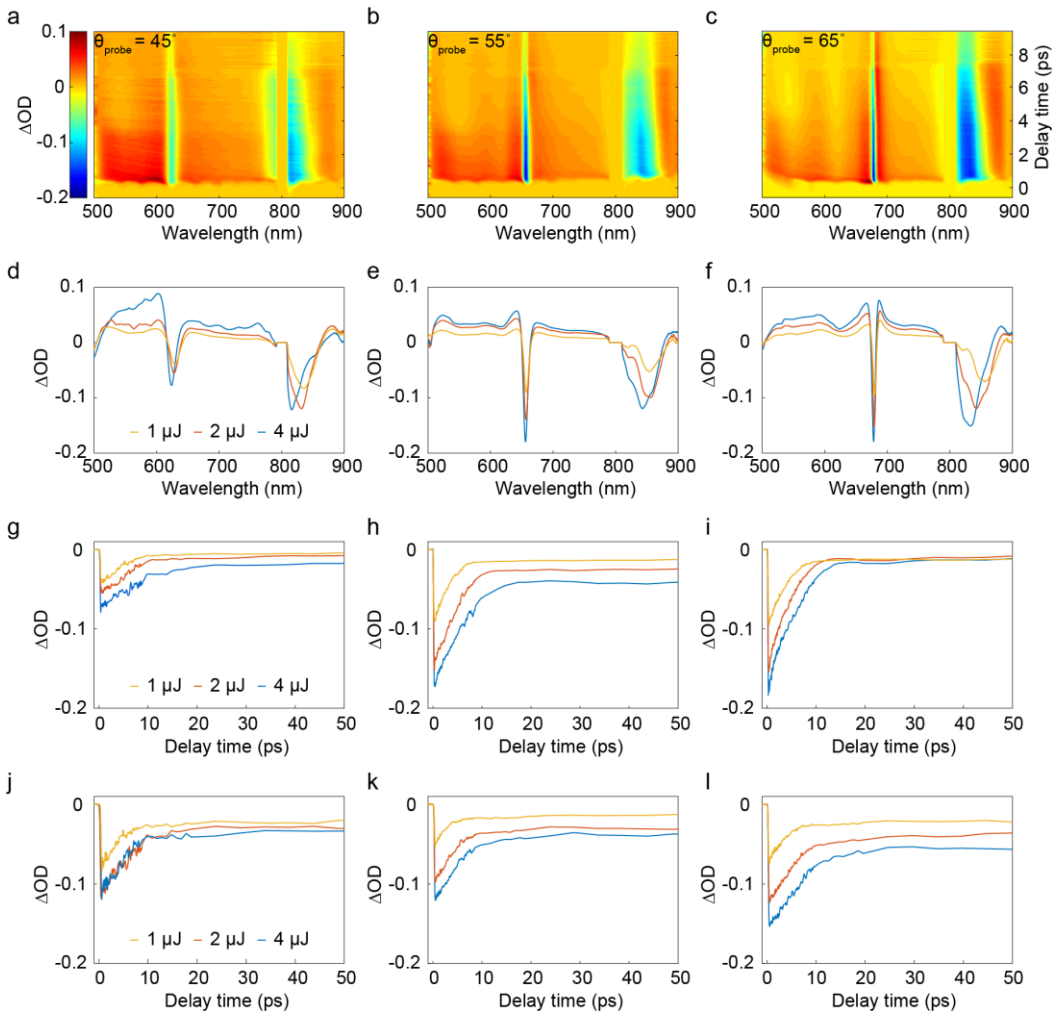

Figure 13: Angle- and time-resolved spectroscopy of the Au/ITO/Au plasmonic lattice with an off-resonance control light. (a-c) Two-dimensional transient reflection maps measured with an off-resonance pump and TM-polarized probes at $\theta_{probe} = 45°$, 55°, and 65°, respectively. The pump wavelength is fixed at 500 nm, near the interband transition of gold, and the energy per pulse is 4 μJ. (d-f) Spectral responses of transient ΔOD for various pump energies, monitored at delay times corresponding to the maximum ΔODs for each probe angle. Dynamic tunability of the modulation wavelength and the narrow full-width-half-maximum (FWHM) of the transient reflection are witnessed around the LP resonance. (g-i) Effect of the pump energy on the temporal response of ΔOD at λ_{LP} at the stated values of θ_{probe}. A larger modulation depth along with faster dynamics is achieved at larger excitation angles. (j-l) Similar measurements performed at λ_{FP}. At λ_{FP}, the time dynamics and the modulation depth are less sensitive to the excitation angle.

Time dynamics of the all-optical modulations at both the LP (Figure 13g-i) and the FP (Figure 13j-l) modes can be interpreted using two relaxation time constants corresponding to the electron-phonon ($\tau_{e\text{-}ph}$) and phonon-phonon ($\tau_{ph\text{-}ph}$) scattering processes. The former relaxation event occurs on a characteristic timescale of several picoseconds while the latter occurs on a timescale of hundreds of picoseconds to a few nanoseconds. Regardless of the incident angle, increasing the pump energy decelerates both relaxation pathways because the higher thermal load increases the electron heat capacity of gold.[9-10,12] At any given pump energy, however, the LP mode consistently demonstrates faster relaxation dynamics as θ_{probe} increases. For instance, $\tau_{e\text{-}ph}$ decreases from 4.86 to 2.32 ps under a 1 μJ excitation energy when the probe angle changes from 45° to 75°. To understand this trend, we investigate the chronology of scattering events that succeeds the photoexcitation of the plasmonic structure. The optical pump at 500 nm, close to the interband transition of gold, initially creates an athermal electron distribution that is subsequently thermalized through the electron-electron scattering on a femtosecond timescale. Under such a condition, for relatively long probe wavelengths, the transient response of gold primarily stems from the increased intraband damping effects, which subsequently modify both the real and the imaginary parts of the permittivity with a dominant contribution to $\mathrm{Im}(\varepsilon_{Au})$.[2,9] The increased association of the optical Kerr effect to the $\mathrm{Im}(\varepsilon_{Au})$, on one hand, and the reduced contribution of the absorption loss to the resonance linewidth of the LP mode, on the other hand, lead to overall faster relaxation dynamics at longer resonance wavelengths. Following a similar rationale, the larger resonance wavelength of the FP mode enables slightly faster transient dynamics than the LP mode, especially at smaller probe angles.

3.3 Femtosecond Optical Switching Facilitated by Hot-Electron Transport

Resonant pumping has a substantial impact on the time dynamics of the nonlinear transient response. In this case, "resonant pumping" refers to the excitation of the sample using TM-polarized light with $\lambda_{pump} = \lambda_{LP}$, λ_{LP} being obtained from the static measurements (Figure 14a). For an incident angle of $\theta_{pump} = 55°$, we set the pump wavelength to $\lambda_{pump} = 657$ nm and probe the sample using a TM-polarized beam at $\theta_{probe} = 65°$. While the 2D map (Figure 14b) shows typical transient bleaching around the LP and FP resonance wavelengths (i.e., $\lambda_{LP} = 677$ nm and $\lambda_{FP} = 830$ nm, respectively) surrounded by induced reflection wings, the time dynamics (Figure 14c) under on-resonance pumping drastically differ from the relaxation kinetics shown in Figure 13. When we pump the sample on resonance at λ_{LP}, both resonance modes of the probe light display an extra relaxation channel, through which most of the stored energy in the electron gas is dissipated within a femtosecond timescale (LP mode: 192 ± 0.04 fs; FP mode: 173 ± 0.03 fs). This fast component is followed by electron-phonon and phonon-phonon scattering events with slower time dynamics. We attribute the femtosecond transient component to the fast injection of plasmonically induced hot-electrons from the Au nanocubes into the adjacent ITO layer. Indeed, the resonantly excited lattice plasmons decay through the intraband excitation of conduction electrons in a non-radiative manner and thus create a population of energetic hot-carriers above the Fermi level (Ef). The quasi-instantaneous transition of the hot-electrons across the Au/ITO interface prevents internal thermalization and enables the ultrafast optical modulation observed in Figure 14c. The measured femtosecond component does not show pump power dependency; therefore, eliminating the possible influence of the plasmonically enhanced light absorption on the activation of the ultrafast relaxation pathway.

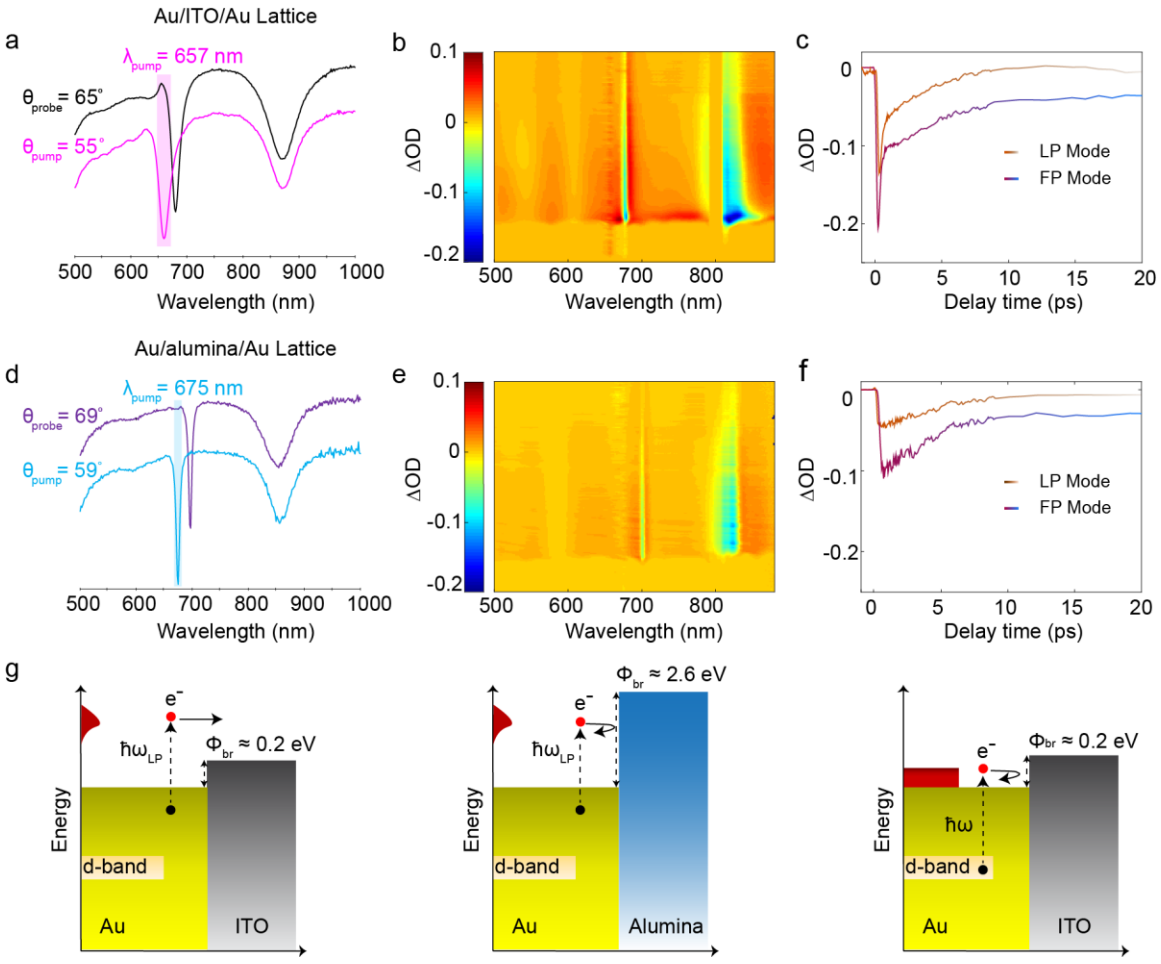

Figure 14: Femtosecond all-optical modulation enabled by the interfacial transfer of hot-electrons. (a) Static optical response of the Au/ITO/Au plasmonic lattice, obtained at 55° and 65° incidence angles. These angles are maintained for subsequent ultrafast measurements with pump and probe lights. The shaded region shows the FWHM of the LP mode where efficient resonant pumping of the device is achievable. (b) Transient ΔOD map of the plasmonic lattice with on-LP-resonance excitation at λ_{pump} = 657 nm. (c) Relaxation kinetics of the resonant modes monitored using TM-polarized probes at λ_{LP} = 677 nm and λ_{FP} = 830 nm. A femtosecond component in the transient response of the Au/ITO/Au structure is enabled by the ultrafast dynamics of hot-electron exchange at the Au/ITO interface. (d-f) Analogous characterization shown for the Au/alumina/Au control device. The lack of the femtosecond component in this case confirms the hot-electron assisted nature of the ultrafast phenomena in the Au/ITO/Au plasmonic lattice. (g) Schematic band diagrams at the interface of Au/ITO under 657 nm excitation (left), Au/alumina under 675 nm excitation (middle), and Au/ITO under 500 nm excitation (right).

To further verify the mechanism of the observed phenomenon, we conducted a control experiment in which we replace the ITO layer in the plasmonic lattice with an alumina spacer with a similar thickness. The control device is designed to have a static optical response resembling that of the ITO-incorporated structure, so that the difference in the time dynamics of the two samples, if any, can be safely attributed to the material-related differences. Figure 14d-f illustrates the linear optical response, the 2D transient map, and the relaxation kinetics of the control device, respectively, under similar excitation conditions to those of the Au/ITO device. As Figure 14f depicts, the temporal response in the control sample has no trace of a femtosecond component, and its dynamics are primarily governed by the slow relaxation mechanisms discussed before. Since the on-resonance pump light also generates energetic carriers in the control device, the observed discrepancy in the dynamics of the two samples is then ascribed to different potential barriers (Φ_{br}) at the interface of Au and spacer layers in the two cases. As illustrated in the band diagrams in Figure 14g, the injection barrier at the Au/ITO interface ($\Phi_{br} \approx 0.2$ eV [17]) is much smaller than that of the Au/alumina interface ($\Phi_{br} \approx 2.6$ eV [26,27]). Therefore, the generated hot-electrons in the Au/ITO/Au lattice have sufficient energy (up to $E_{LP} \approx 1.88$ eV) to overcome the potential barrier, while those in the Au/alumina/Au sample stay confined in the metal and eventually thermalized after prolonged decay processes. Moreover, the absence of the femtosecond component in the resonantly excited Au/alumina/Au device rules out the possibility of coherent plasmonic effects as the origin of the ultrafast dynamics. In the case of off-resonance excitation ($\lambda_{pump} = 500$ nm, Figure 13), the photoexcited carriers in Au are primarily generated from the direct interband transition of d-band electrons (~ 2.5 eV below E_f) to the sp-band located slightly above the

Fermi level (Figure 14g). As a result, the energy of the photoexcited electrons is not sufficient to overcome the barrier height at the Au/ITO interface. Moreover, unlike the plasmonically induced hot-electrons, the photoexcited carriers are not localized to the surface of the nanocubes, so they undergo scattering events before reaching the Au/alumina interface.[28] Consequently, the extra energy of the electrons in this case is mostly dissipated via thermal processes at the pico- to nano-second timescale.

3.4 Interplay Between Polarization of Light and Modulation Depth

To further elucidate the nature of the femtosecond transient component in the Au/ITO/Au plasmonic lattice, we performed polarization-resolved pump-probe measurements. The blue curve in Figure 15a displays the time dynamics of the LP mode probed with a TM-polarized light and excited with a TE-polarized pump at λ_{pump} = 657 nm. The temporal response exhibits a picosecond timescale followed by thermalization via phonon-phonon scattering, similar to the dynamics of isolated nanoparticles excited with an intraband pump signal.[15] The observed slow relaxation was expected, as the TE-polarized pump cannot excite the LP resonance, causing the impinging photons to heat up the conduction electrons rather than generating energetic surface carriers. This observation substantiates the proposed mechanism, which is based on the injection of plasmonically induced hot-electrons into the ITO layer,as the principal cause of the femtosecond component in the relaxation process. While conductive transparent oxides such as ITO can offer strong third-order optical nonlinearities,[29-30] in our all-optical modulation technique, the ITO layer is primarily used as a host material for hot-electrons; and the fast component is independent of the intrinsic relaxation dynamics of the photoexcited carriers inside this layer. This explanation is verified by acquiring the transient response of another control

device in which an ITO layer was deposited on an unpatterned gold substrate. In the absence of plasmonic modes, the same measurement for this control sample exhibits a slower picosecond-scale response time, shown by the green curve in Figure 15a.

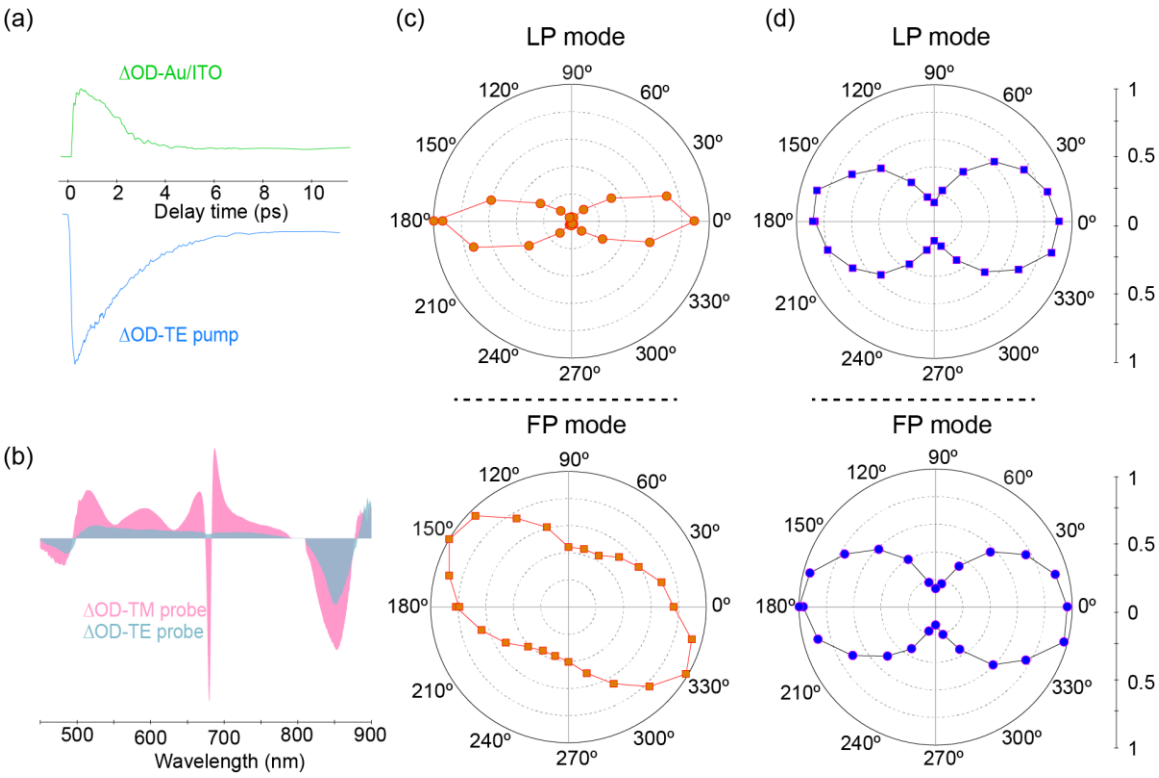

Figure 15: Dynamic tuning of transient |ΔOD| via polarization control. (a) Temporal response of the Au/ITO/Au plasmonic lattice measured with a TM-polarized probe at $\lambda_{probe} = 677$ nm and pumped with a TE-polarized light at $\lambda_{pump} = 657$ (blue curve). The green curve exhibits the transient response of a thin ITO/gold stack, recorded via TM-polarized pump and probe signals at the aforementioned wavelengths, where no femtosecond response is present. (b) Spectral response of the transient ΔOD for TM- and TE-polarized probes, excited with a TM-polarized pump light. (c) Polar diagrams illustrate the normalized transient |ΔOD| as a function of the polarization angle of the probe light, extracted at the LP (top) and the FP (bottom) resonance wavelengths. In these measurements, a TM-polarized pump light at $\lambda_{pump} = 500$ nm with 1 μJ pulse energy is used to excite the Au/ITO/Au plasmonic lattice. The polar diagram of the LP mode helps to separate the plasmon-induced contribution from the effect of the intrinsic material responses. In these diagrams, 0° and 90° correspond to TM- and TE-polarized probes, respectively. (d) Effect of pump polarization on the modulation depth of the probe signals at the LP and FP resonances, acquired

using a 657 nm control light with 1 μJ pump energy at $\theta_{pump} = 55°$. The measured |ΔOD| of the LP mode at $\theta_{pol} = 90°$ is analogous to a transient change in response to an off-resonance intraband excitation.

Besides activating the ultrafast relaxation pathway for hot-carriers, plasmonic resonances are essential to enhance the optical modulation depth through the extraordinary sensitivity of the resonance lineshape to the pump-induced change in the dielectric permittivity. The polarization dependence of the LP mode allows us to study the impact of the static response of the plasmonic lattice on the achievable modulation depth. As shown in Figure 15b, switching the probe polarization from TM to TE drastically affects the spectral behavior of ΔOD. For the TM-polarized probe, the plasmonic lattice displays a large negative ΔOD at λ_{LP} that was previously ascribed to the spectral shift and broadening of the resonance lineshape. In sharp contrast, the TE-polarized probe in absence of the LP resonance reveals a weak induced reflection that can be attributed to the pump-induced modifications of gold and ITO permittivities. The significance of the plasmonic resonances is better visualized in the normalized polar diagrams of ΔOD, recorded at λ_{LP} (Figure 15c, top) and λ_{FP} (Figure 15c, bottom) as a function of the probe polarization angle θ_{pol}. At both resonant wavelengths, the magnitude of ΔOD is dynamically tunable for a fixed pump condition by controlling polarization of the probe signal. In the case of the LP mode, the dynamic tuning of the modulation depth from the maximal ΔOD to zero is possible, as revealed in Figure 15c. The diminished net modulation depth occurs at a specific probe angle, at which the LP-induced negative ΔOD cancels out the transient reflection induced by changes in the permittivities of Au and the ITO layer. The transient modulation at the FP resonance, on the contrary, cannot be set to zero by tuning polarization of the probe signal, as the polar pattern in this case is determined largely by the combined near- and far-

field optical interactions. We also studied the dynamic control of the modulation depth by varying the pump polarization. Figure 15d shows the normalized polar diagram of ΔOD as a function of the pump polarization angle, measured using a TM-probe light. As expected, maximum modulation occurs at the TM-polarized pump (on-resonance excitation) and the minimum transient change is located at the TE-polarized pump (off-resonance excitation). In contrast to the polar plots for probe polarization angles (Figure 15c), both resonance modes in Figure 15d display similar patterns, because manipulation of the pump polarization has no impact on the excitation of the resonance modes (that are controlled by the probe polarization) and instead, it influences the magnitude of the optically-induced perturbation of the permittivity of the constituent materials.

In conclusion, we demonstrated here that the slow response time of optical Kerr nonlinearities in metals, which has remained as an intrinsic limitation in plasmonic all-optical modulation systems, can be effectively lifted by employing the ultrafast dynamics of hot-electron injection at the interface of nanostructured metals and electron acceptor materials to enable ultrafast dynamics. This phenomenon, by reducing the impact of electron-phonon interactions, instigates a relaxation pathway that allows recovery of the stored optical energy in the metal within a timescale shorter than 200 fs. Furthermore, the performed transient spectroscopy reveals active control over the modulation depth and speed, owing to the optimized response of the designed lattice plasmon in the linear domain. Our findings address the emerging demand for the development of ultrafast all-optical modulators for nanophotonic devices and systems. The results of this work will also expand the scope of hot-electron science and technology beyond the conventional

photovoltaic and photocatalytic applications, in particular, for ultrafast optical nonlinear processes.

3.5 Details of Fabrication and Optical Characterizations

The fabrication process starts with electron-beam (e-beam) evaporation (Denton Inc.) of 10 nm/100 nm Ti/Au films on a silicon substrate, followed by the deposition of an approximately 10 nm thick ITO layer using an RF sputtering machine (Denton Inc.) at room temperature. Afterwards, the plasmonic structures were formed on top of the ITO layer in a three-step fabrication process: (i) standard e-beam lithography (JEOL JBX – 9300FS) to define the plasmonic lattice pattern, (ii) e-beam evaporation of 2 nm/40 nm Ti/Au metal, and (iii) a lift-off process in acetone to resolve the plasmonic array. We used poly (methyl methacrylate) (PMMA) as the positive tone electron resist for the e-beam lithography.

The reflectance spectra of the samples at a normal incident angle were collected with a 50× objective (NA: 0.5) using a Craic QDI 202 micro-spectrophotometer mounted on a Leica DM 4000M microscope. The light source used for the reflectance measurement is a tungsten halogen lamp. A woollam M-2000 ellipsometer in the reflection mode was used for the angle-resolved ellipsometry measurements. A broadband (245 – 1690 nm) circularly polarized light illuminates the sample at a wide range of excitation angles ($45° < \theta < 75°$, 2^o-stepsize). Changes in the polarization and intensity of light, as reflected from the sample, are recorded in terms of $\Psi - \Delta$ values. The accuracy of the ellipsometry system is better than $\delta\Psi = \delta\Delta = 0.015°$. The ratio of the two reflection coefficients R_{TM}^{θ} and R_{TE}^{θ} was then calculated based on the ellipsometry equation $R_{TM}^{\theta} / R_{TE}^{\theta} = |\tan(\Psi)|^2$.

The femtosecond transient reflection setup is based on a regenerative amplified Ti: Sapphire femtosecond laser system (Coherent Legend, 1 kHz repetition rate, 150 fs pulse duration, and 2.4 mJ/pulse fundamental pulse energy at 800 nm), and the data collection was conducted using a Helios spectrometer (Ultrafast Systems Inc.). A 90:10 beam splitter divides the 800 nm output light of the amplifier into two beams. The low intensity part is focused on a 2 mm thick sapphire window to generate a white light continuum (WLC) as the probe signal. To account for unwanted fluctuations, the WLC signal is divided again into two parts (70:30) to probe the sample using the 70% portion and correct fluctuations using the 30% portion. We focus the probe beam on the sample using a parabolic mirror and the reflected light is collected by employing an optical fiber that is coupled into a visible spectrometer equipped with a 1024 elements CMOS camera. To generate the pump signals, 1 mJ of the 800 nm fundamental beam is focused on an optical parametric amplifier (Opera coherent) and generates two tunable near-IR (NIR) pulses, signal and idler. The signal beam is then separated using a dichroic mirror and focused on a second harmonic generation BBO crystal to generate the pump beams we used for transient measurements. A bandpass filter is added to filter out the remaining NIR pulse and the 800 nm pulse. Two visible half-wave plates are placed right before the sample for both pump and probe beams to change their polarizations. The typical instrument response is well fitted by a Gaussian function with a 150 fs FWHM. The chirp is corrected by fitting the solvent response in all data sets.

3.6 References

[1] M. Kauranen, A. V. Zayats, *Nature Photon.* **2012**, *6*, 737.

[2] G. A. Wurtz, R. Pollard, W. Hendren, G. P. Wiederrecht, D. J. Gosztola, V. A. Podolskiy, A. V. Zayats, *Nature Nanotech.* **2011**, *6*, 106.

[3] K. F. MacDonald, Z. L. Samson, M. I. Stockman, N. I. Zheludev, *Nature Photon* **2009**, *3*, 55.

[4] G. Li, S. Zhang, T. Zentgraf, *Nature Rev. Mater.* **2017**, *2*, 17010.

[5] S. P. Rodrigues, S. F. Lan, L. Kang, Y. H. Cui, P. W. Panuski, S. X. Wang, A. M. Urbas, W. S. Cai, *Nature Commun.* **2017**, *8,* 14602.

[6] K. M. Dani, Z. Y. Ku, P. C. Upadhya, R. P. Prasankumar, S. R. J. Brueck, A. J. Taylor, *Nano Lett.* **2009**, *9*, 3565.

[7] D. Pacifici, H. J. Lezec, H. A. Atwater, *Nature Photon.* **2007**, *1*, 402.

[8] G. V. Hartland, *Chem. Rev.* **2011**, *111*, 3858.

[9] C. Voisin, N. Del Fatti, D. Christofilos, F. Vallee, *J. Phys. Chem. B* **2001**, *105*, 2264.

[10] N. Del Fatti, F. Vallee, C. Flytzanis, Y. Hamanaka, A. Nakamura, *Chem. Phys.* **2000**, *251*, 215.

[11] A. D. Neira, N. Olivier, M. E. Nasir, W. Dickson, G. A. Wurtz, A. V. Zayats, *Nature Commun.* **2015**, *6*, 7757.

[12] S. Link, M. A. El-Sayed, *J. Phys. Chem. B* **1999**, *103*, 8410.

[13] S. Park, M. Pelton, M. Liu, P. Guyot-Sionnest, N. F. Scherer, *J. Phys. Chem. C* **2007**, *111*, 116.

[14] M. Abb, Y. D. Wang, C. H. de Groot, O. L. Muskens, *Nature Commun.* **2014**, *5*, 4869.

[15] H. Baida, D. Mongin, D. Christofilos, G. Bachelier, A. Crut, P. Maioli, N. Del Fatti, F. Vallee, *Phys. Rev. Lett.* **2011**, *107*, 057402.

[16] M. L. Brongersma, N. J. Halas, P. Nordlander, *Nature Nanotech.* **2015**, *10*, 25.

[17] C. Clavero, *Nature Photon.* **2014**, *8*, 95.

[18] K. Wu, J. Chen, J. R. McBride, T. Lian, *Science* **2015**, *349*, 632.

[19] H. Zhang, A. O. Govorov, *J. Phys. Chem. C* **2014**, *118*, 7606.

[20] R. Sundararaman, P. Narang, A. S. Jermyn, W. A. Goddard, H. A. Atwater, *Nature Commun.* **2014**, *5*, 5788.

[21] A. Manjavacas, J. G. Liu, V. Kulkarni, P. Nordlander, *ACS Nano* **2014**, *8*, 7630.

[22] W. Li, J. Valentine, *Nano Lett.* **2014**, *14*, 3510.

[23] A. Moreau, C. Ciraci, J. J. Mock, R. T. Hill, Q. Wang, B. J. Wiley, A. Chilkoti, D. R. Smith, *Nature* **2012**, *492*, 86.

[24] J. B. Lassiter, F. McGuire, J. J. Mock, C. Ciraci, R. T. Hill, B. J. Wiley, A. Chilkoti, D. R. Smith, *Nano Lett.* **2013**, *13*, 5866.

[25] H. T. Mohammad Taghinejad, Sidney T. Malak, Hesam Moradinejad, Zihao Xu, Yawei Liu, Eric V. Woods, Ali A. Eftekhar, Tianquan Lian, Vladimir V. Tsukruk, Ali Adibi, *Laser Photon. Rev*. in press **2017**.

[26] H. Chalabi, D. Schoen, M. L. Brongersma, *Nano Lett.* **2014**, *14*, 1374.

[27] R. Banan-Sadeghian, S. Badilescu, Y. Djaoued, S. Balaji, V. V. Truong, M. Kahrizi, *IEEE Electr. Dev. L* **2008**, *29*, 312.

[28] B. Y. Zheng, H. Q. Zhao, A. Manjavacas, M. McClain, P. Nordlander, N. J. Halas, *Nature Commun.* **2015**, *6*, 7797.

[29] P. J. Guo, R. D. Schaller, L. E. Ocola, B. T. Diroll, J. B. Ketterson, R. P. H. Chang, *Nature Commun.* **2016**, *7*, 12892.

[30] M. Z. Alam, I. De Leon, R. W. Boyd, *Science* **2016**, *352*, 795.

CHAPTER 4. COHERENT CONTROL OF PHASE AND POLARIZATION OF LIGHT

As we discussed in the previous chapter, the ultrafast modulation of light properties is a rapidly evolving frontier in nanophotonics, envisioned for all-optical data communication and high-speed data processing. The current state-of-the-art in this area is mainly focused on the all-optical modulation of light "intensity", which is the primary information-containing attribute of light in existing systems. However, exploiting the "phase" and "polarization" of light as carriers of information enables denser data storage and an improved means of encryption, especially under conditions with low power budgets. In spite of such a pressing need, the span of literature on the ultrafast all-optical control of phase and polarization remains limited to a few sparse reports. In this chapter, we demonstrate ultrafast all-optical tuning of the phase and polarization of light across the visible spectrum. By introducing a fundamentally novel approach we show that hot-electron transfer at the interface of plasmonic metals and electron acceptor materials enables the femtosecond modulation of the phase, polarization, and intensity of light, independent of the intrinsic carrier dynamics of comprising materials. Our work reveals the viability of dynamic phase and polarization control in plasmonic systems for all-optical switching and data processing, in a spectrally tunable fashion.

4.1 Background, Motivation, and Design of Reflective Plasmonic Polarizers

All-optical active plasmonics – the control of coherent charge oscillations with light – is a fast-evolving frontier in nanophotonics with promising prospects for optical

communications and high-speed data processing. The current portfolio of this area of study contains a rich diversity of design platforms primarily based on subwavelength plasmonic elements for the active tuning of light properties from the visible to mid-infrared (IR) spectral range.[1-9] As a working principle, most of these designs rely on the interplay between the resonant behavior of plasmonic cavities and the change in the refractive index of comprising materials, induced by high-intensity light beams. In this regard, noble metals and transparent conductive oxides (TCOs) have been extensively explored as they simultaneously offer dense free electrons necessary for plasmonic responses and strong optical Kerr nonlinearity for optical switching.[1, 2, 10-17] TCO-based devices exhibit superior performance thanks to their smaller electron heat capacity, which leads to a notable change in the refractive index under strong optical excitation.[10, 13] However, the comparably lower electron density in TCOs limits the application of such materials to the near-to-mid-IR regime. Optical modulation of plasmons within the visible spectrum, therefore, needs to be addressed using metals with significantly larger electron densities.

In terms of wave properties, all optical modulators have traditionally utilized the modulation of the amplitude as the primary information-containing attribute of light. Although exploiting the light intensity relaxes the level of complexity in the demonstration of ultrafast optical switching, this convenience limits all-optical modulation from incorporating a wide range of on-demand functionalities in modern nanophotonics and quantum optics. For instance, controlling the valley polarization,[18] splitting the degenerate Landau level transitions,[19, 20] and the spin angular momentum [21, 22] are among emerging applications that seek active tuning through the modulation of the phase and polarization rather than the amplitude of light. Exploring the two extra degrees of freedom of light, the

phase and polarization, allows for a denser packing of information onto optical carrier waves in a multiplexed manner. Moreover, phase- and polarization-encoded information can be more accurately retrieved under low signal-to-noise operation conditions, expanding the realm of the applications that all-optical signal processing may contribute to. The span of the literature on the ultrafast switching of phase and polarization is, however, limited to a few reports utilizing anisotropically-strained quantum wells,[23] magnetic Kerr-type materials,[24, 25] perfect absorbers made of doped cadmium oxides,[26] and hybrid TCO structures at the epsilon-near-zero regime.[27] In these limited but inspiring studies, the performance of the reported devices largely depends on the intrinsic material nonlinearities, which are significant mostly at the infrared or terahertz regions. To circumvent such material constraints, an alternative modulation scheme based on device-level designs is much needed. In this chapter, we will discuss all-optical phase and polarization modulation of light in the visible spectrum by employing a planar plasmonic crystal (PlC) that supports high quality factor (high-Q) and polarization-resolved plasmonic resonances. We will see that the on-resonance optical excitation of the PlC mode enables pronounced phase and polarization modulation around the predesigned operating wavelength of the device, which can be spectrally tuned via the in-plane momentum of light. Our experiments reveal that the suppressed radiation loss of the PlC mode allows for efficient generation of hot electrons via the nonradiative decay of plasmons. The transport of such energetic carriers from the devised nanostructured metals into an electron-accepting material (i.e., indium tin oxide (ITO)) activates an ultrafast relaxation pathway through which femtosecond modulation becomes prominent. To the best of our knowledge, this work represents the first demonstration of all-optical phase and polarization

modulation across the visible spectrum, using any mechanism, that offers a response time on the picosecond scale or faster.

Our devised PlC consists of a two-dimensional square array of gold nanoparticles separated from a backside gold film via a 10 nm-thick ITO layer (Figure 16a). As shown in Figure 16b, the simulated reflection spectra of the device for TM- and TE-polarized incidence exhibit disparate behaviors. The desired polarization selectivity of the device can be captured from an extra resonance mode that only appears under the TM-polarized excitation (Figure 16b, left map) and is continuously tunable by adjusting the angle of incidence. Under TM illumination, the structure supports two resonance modes: a Fabry-Pérot (FP)-like plasmonic resonance that is independent of the incident angle, and (ii) a PlC mode that is spectrally tunable by varying the angle of incidence. In contrast, the TE-polarized light fails to excite the PlC mode, while the angle-insensitive FP mode still exists and remains at a fixed spectral location. This angle and polarization sensitivity is further verified in the measured reflection spectra, as depicted in Figure 16c. For instance, at an incident angle of 60°, more than 92% of the TM-polarized light is absorbed at λ_{PlC} = 669 nm, while less than 3% of the TE light is absorbed at the same spectral location. Such an anisotropic optical behavior is essential to the manipulation of the polarization and phase of light as will be seen later.

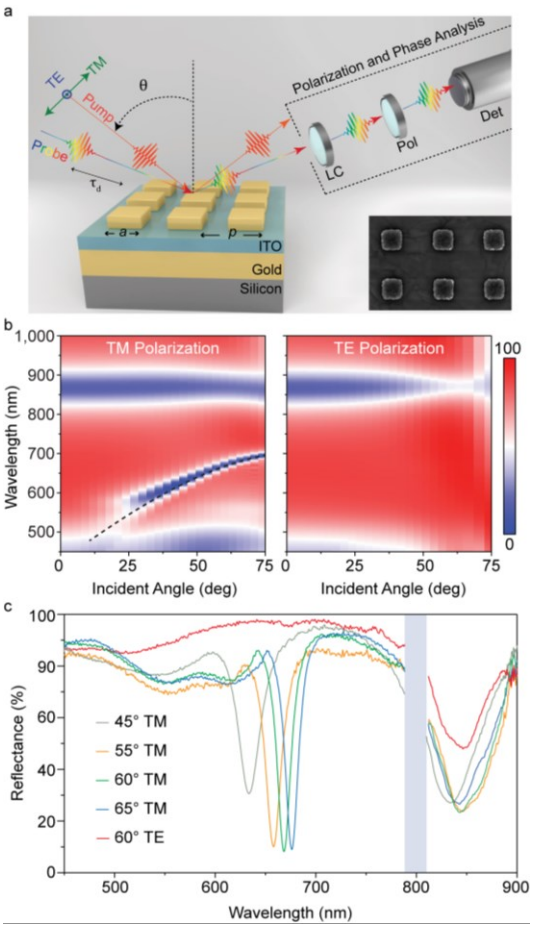

Figure 16: Characterization of the static optical response of the plasmonic crystal. (a) Schematic of the plasmonic crystal and the characterization setup. The liquid crystal phase retarder (LC) and the polarizer (Pol) are used for the transient analysis of the phase and polarization of the reflected light from the device. The inset shows a representative SEM image of the sample with a = 110 nm and p = 360 nm. (b) Numerically calculated reflection spectra of the plasmonic crystal in (a) at varying incident angles under TM- and TE-polarized light. The dashed line on the TM-polarized map indicates the spectral location of the PlC mode, predicted by the Rayleigh formula. (c) The static optical reflection of the device measured at a few representative angles. The spectral region marked with gray color has been filtered out because of its proximity with the pump beam at 800 nm.

The polarization dependence of the plasmonic crystal mode stems from its out-of-plane dipolar nature that can be triggered exclusively via the out-of-plane electric field component of a TM-polarized wave. Since the TE polarization does not offer such a field

component, the PlC mode is absent from the static optical response under TE polarization, despite the fact that both polarization states provide the crystal with identical in-plane momenta at all incident angles. The excitation of out-of-plane dipoles within the Au nanoparticles allows for the resonant coupling of the scattered light from the unit cells and leads to the suppression of the optical reflection from the array at the angle-tunable resonance wavelength of the PlC mode (i.e., λ_{PlC}). As indicated by the dashed line on Figure 1b, the resonance wavelength of the PlC mode follows Rayleigh formula $\lambda_{PlC} = p\ (1 + \mathrm{Sin}\theta)$, where p is the lattice constant and θ is the incident angle. The minor differences witnessed between the numerical results and the Rayleigh formula at small incident angles can be explained by the spectral proximity of the PlC mode and the higher-order localized resonance mode of the structure. Besides the polarization sensitivity and spectral tunability, the narrow resonance linewidth is another critical feature of the PlC mode, especially at large incident angles. Indeed, the suppression of radiative loss in the plasmonic crystal enables the conduction-band electrons of gold to undergo a long-lived coherent oscillation within the nanoparticles and, therefore, leads to a high-Q resonance mode. This key feature renders our structure a promising candidate for applications that rely on plasmonically-induced hot electrons, because the energy of the PlC mode will be dissipated primarily via the absorption loss and thereby yielding energetic carriers above the Fermi level of gold.

4.2 Static Ellipsometry Measurements

The polarization state of light can be accurately determined by monitoring the phase difference (Δ) and amplitude ratio ($\gamma = |E_{TM}/E_{TE}|$) of the orthogonal components of the electric field (i.e., E_{TM} and E_{TE}). Thus, we use spectroscopic ellipsometry to simultaneously measure changes in Δ and γ upon the reflection of light from the plasmonic crystal. Figure

17a, c shows ellipsometric Ψ – Δ spectra of our structure, respectively, at a few representative incident angles. For this measurement, the PlC is illuminated with a linearly polarized beam at $\theta_{pol} = 45°$ and the spectral behavior of γ can be calculated as $\gamma = |\tan(\Psi)|$. The Ψ spectra exhibit angle- and wavelength-dependent trends with two resonance dips at λ_{PlC} and λ_{FP}, similar to those observed in the reflection spectra (Figure 16c). We note that around the λ_{PlC}, the plasmonic crystal primarily acts as a mirror for the TE component with near perfect reflection, while for the TM component a secondary mode appears with angle-dependent absorption. For this reason, the Ψ spectra (i.e., $\Psi = \tan^{-1}(|E_{TM}/E_{TE}|) \approx \tan^{-1}(|E_{TM}|)$) take on characteristics dominated by the TM-component of the reflected light and demonstrate similar trends to those observed in Figure 1c. Furthermore, upon reflection from the crystal surface, the relative phase difference between TM and TE components displays two semi-singularities around the λ_{PlC} and λ_{FP} (Figure 17c). Such behaviors are fingerprints of the transfer function of resonant cavities when a transition from an in-phase to an out-of-phase oscillation occurs around the resonance wavelength. As a result, the spectral behavior of the Δ parameter is strongly correlated to the γ parameter and the FWHM of the resonance modes. Therefore, a small γ at a large incident angle enables the plasmonic crystal to create a substantial static phase shift within a narrow wavelength range at the vicinity of the PlC mode.

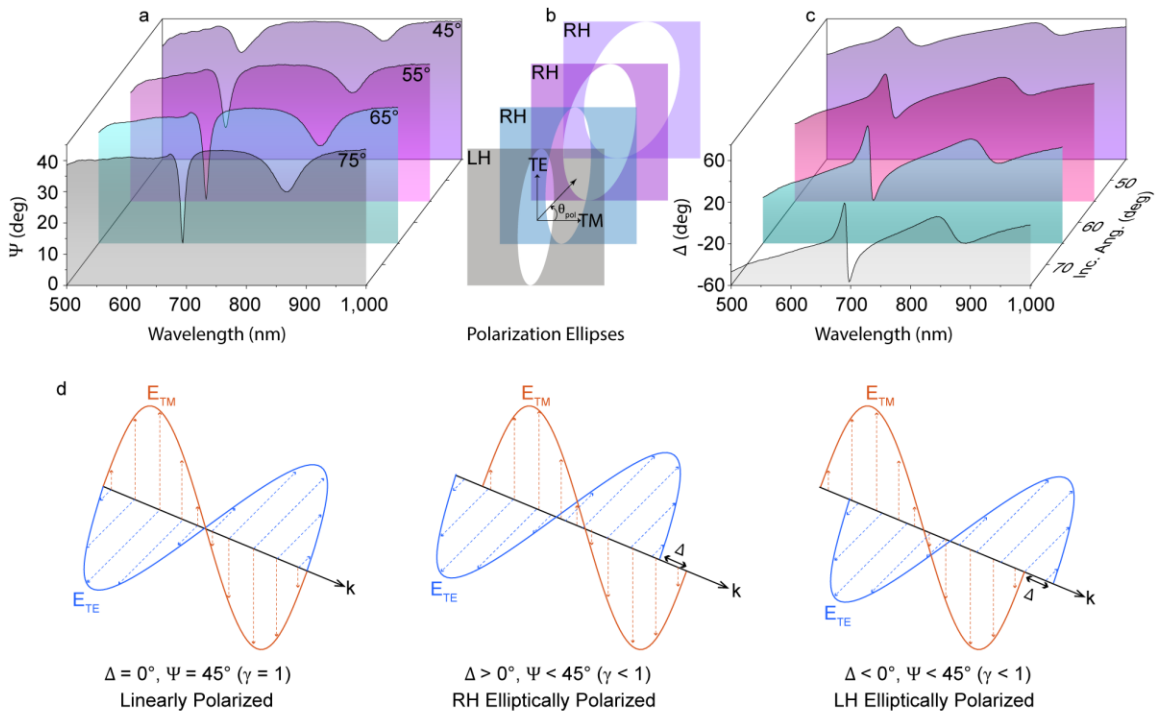

Figure 17: Angle-resolved characterization of static phase and polarization responses. (a) Measured Ψ spectra upon the reflection of a linearly polarized light (θ_{pol} = 45°) from the PlC, monitored at θ = 45°, 55°, 65°, and 75°. The two resonant dips indicate the spectral locations of the PlC (i.e., narrow dip) and FP (i.e., broad dip) modes. (b) Output polarization ellipses at λ_{PlC}, retrieved from the measured Ψ – Δ spectra. At larger excitation angles, the reduced reflection of the TM-component rotates the polarization ellipse towards the TE polarization axis. (c) The measured phase difference between the TE and TM components, induced by the interaction of light with the plasmonic crystal at incident angles identical to those shown in (a). (d) Schematic description of the polarization state based on the Ψ – Δ values. Here, the angle of incidence serves as a knob for controlling the phase difference and intensity ratio of the orthogonal components of the electric field for the spectral tuning of the output polarization.

Utilizing the measured Ψ – Δ spectra in Figure 17a, c, we can calculate the polarization state of the reflected light at λ_{PlC}. As depicted in Figure 17b, the linear polarization of the input light is converted into an elliptical state that rotates progressively towards the TE axis by increasing the incident angle. The non-vanishing nature of Δ sets the TE component out of phase with the TM component, enabling the conversion of the

polarization state following the reflection of light from the structure. Schematic illustrations in Figure 17d provide an analogy between output polarization states and various $\Delta - \Psi$ combinations, within the context of our work. The $\Delta = 0°$ and $\Psi = 45°$ ($\gamma = 1$) condition describes a linear-polarization state with equal contributions of the orthogonal field components (i.e., $\theta_{pol} = 45°$), corresponding to the input polarization state in our ellipsometry measurements. Since the polarization-sensitive response of the pattern imposes a condition of $\Psi < 45°$ (i.e., $\gamma < 1$), the output polarization can be either right handed (RH) elliptical ($\Delta > 0°$), left handed (LH) elliptical ($\Delta < 0°$), or linear with a $\theta_{pol} > 45°$ at the zero-phase-difference crossing points. Such a wide range of available polarization states offers an amenity for the effective demonstration of all-optical phase and polarization switching, as will be discussed later.

4.3 All-Optical Intensity Switching via Hot-Electron Transport

Our all-optical modulation scheme exploits time-resolved pump-probe characterizations in which an ultra-short laser pulse serves as a control signal to manipulate the interaction of a broadband probe light with the plasmonic crystal. For these measurements, off-resonance (at 500 nm wavelength) and on-resonance (at variable λ_{PIC}) excitations are employed to distinguish the interplay between various relaxation channels following the optical perturbation of the electron distribution within the momentum space. In all measurements, there is a fixed 10° offset between the incident angle of the pump and that of the probe light (i.e., $\theta_{probe} = \theta_{pump} + 10°$), as denoted in Figure 16a. Figure 18a-b illustrates transient maps of the relative optical reflection ($\Delta R/R$), monitored at the probe incident angle of 60° for pump wavelengths of 500 nm and 645 nm, respectively. The latter

pump condition represents the resonance wavelength of the PlC mode at $\theta = 50°$, used as a representative on-resonance excitation. Under both excitations, the device exhibits similar spectral responses (Figure 18c) around the PlC resonance mode. The observed transient lineshape is a manifestation of spectral broadening and slight redshift of the PlC mode as a result of pump-induced changes in the refractive indices of the comprising materials.[28, 29] We also witness that upon changing the pump wavelength from 500 nm to 650 nm, the peak of the induced reflection slightly redshifts, which could be attributed to the change in the refractive indices incurred by the pump light. Contrary to the observed similarity in the spectral responses, the relaxation dynamics, plotted in Figure 18d, shows distinct fingerprints for the two excitation schemes. For the off-resonance excitation, the induced reflection decays within a picosecond timeframe ($\sim$ 7.5 ps), while for the on-resonance excitation a femtosecond relaxation component ($\sim$ 200 fs) primarily governs the temporal response. We attribute the femtosecond decay component to the injection of plasmonically-induced hot electrons over the Schottky barrier (Φ_{inj}) at the interface of Au and ITO.

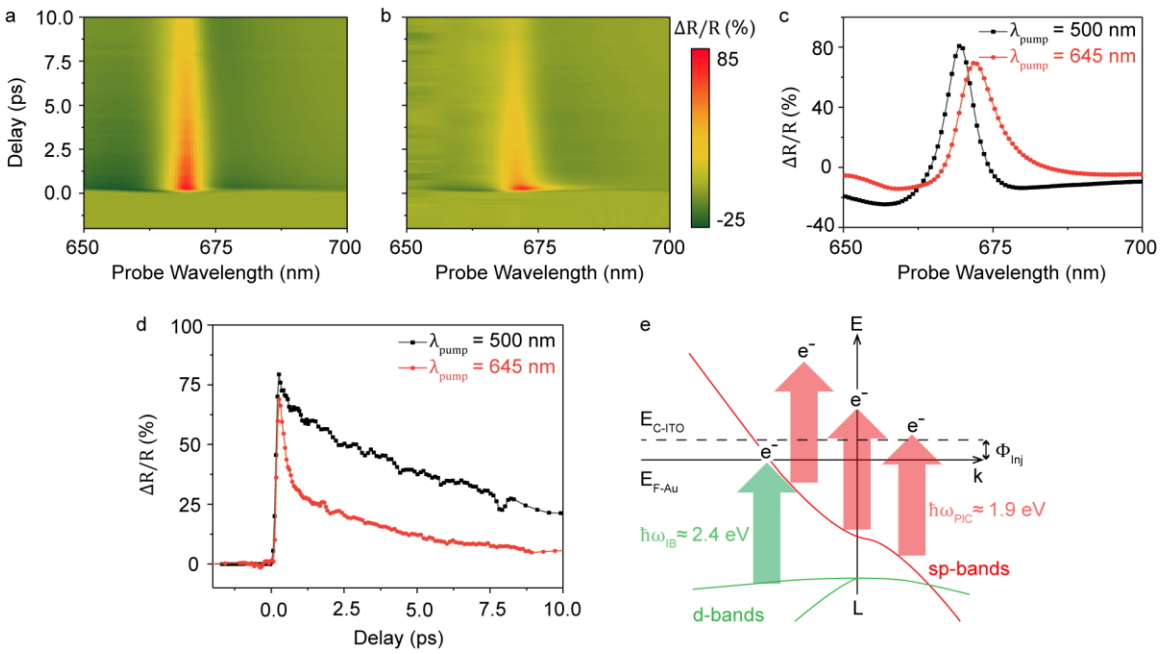

Figure 18: Effect of the excitation wavelength on the relaxation dynamics of photo-excited carriers. Transient ΔR/R maps of the plasmonic crystal under excitation with (a) an off-resonance 500 nm pump light and (b) an on-PlC-resonance 645 nm pump light. In both measurements, pump and probe polarizations are set to TM and incident angles are θ_{pump} = 50° and θ_{probe} = 60°. (c) Spectral ΔR/R responses at the vicinity of the PlC mode, obtained at 270 fs delay time when the maximum modulation occurs. (d) The relaxation dynamics of the PlC resonance mode studied under off- and on-resonance perturbations. The on-resonance excitation allows for the ultrafast modulation of the optical reflection within a 200 fs timescale. The relaxation curves are monitored at wavelengths corresponding to the maximum pump-induced changes. (e) Schematic illustration of the Au band structure around the high-symmetry point L. Contrary to the off-resonance interband excitation, the on-resonance intraband excitation of the PlC mode enables the generation of nonthermal hot electrons with energies beyond the Schottky barrier at the Au/ITO interface.

To unravel the subtle role of the photon energy of the pump light on the transient response of the device, in Figure 18e we have schematically illustrated dominant electronic transitions that can occur around the high symmetry point L. For a pump wavelength of 500 nm, the interband transition of d-band electrons to the sp-band states (the green arrow) is the dominant electronic transition through which a nonthermal electron distribution forms

above the Fermi level of gold ($E_{F\text{-}Au}$).[30-32] The ultrafast decay of nonthermal electrons via the electron-electron scattering subsequently establishes a thermalized state with an elevated effective electron temperature. Such changes in the temperature and density of electrons modify the refractive index of gold and result in the all-optical modulation of the resonance behavior around λ_{PlC}. However, the inherently slow dissipation of the absorbed optical energy via electron-phonon scattering sets a relaxation process with a picosecond characteristic timescale, consistent with the reported results for noble plasmonic metals.[7, 33] In contrast, the temporal response is substantially faster when we excite the device on the PlC resonance. The resonant pumping initially excites the plasmonic crystal mode, which then decays nonradiatively through the intraband transition of sp-band electrons to energy states $E_{F\text{-}Au} < E < E_{F\text{-}Au} + \hbar\omega_{PlC}$ above the Fermi level (red arrows).[34-37] The plasmonically-generated hot electrons have sufficient energy to overcome the injection barrier at the Au/ITO interface ($\Phi_{inj} = 0.2$ eV) [38] and transition from the host metal (i.e., Au) into the electron acceptor (i.e., ITO) within a femtosecond timescale. Indeed, the inherently fast nature of the hot-electron transport combined with the reduced thermal loading of the optically excited system plays the major role in the activation of an ultrafast relaxation pathway under the resonant pumping. The on-resonance measurements we performed at various incident angles, ranging from 45° to 65°, did not reveal a notable change in the dynamics of hot-electron related relaxation. This fact primarily originates from the limitation on the dynamic range of hot-electrons energy, which is limited to $\hbar\omega_{PlC}$ (45°) – $\hbar\omega_{PlC}$ (65°) ≈ 0.2 eV. Since not all energetic carriers are injected across the barrier, the relaxation dynamics also exhibits a phonon-related time trace as manifested by the tail of the time response curve.

4.4 Coherent Control of Phase and Polarization of Light

The strength of the refractive index modulation primarily depends on the intrinsic material properties and is generally independent of the polarization. Therefore, for active polarization switching, utilizing a polarization-selective structure is necessary. The plasmonic platform used in this work satisfies this criterion, as only TM-polarized light may couple to the subradiant PlC mode, which, in turn, can be effectively tuned by pump-induced changes in the refractive indices. In contrast, the TE component of light around λ_{PlC} is largely decoupled from the PlC mode, and the refractive index modification barely influences the response of the TE-polarized light. For experimental demonstrations, we set the probe light to be linearly polarized at 45° and employ the Stokes technique to measure the Δ and γ parameters of the reflected beam, before and after on- or off-resonance optical excitation. We also investigated the $\Psi - \Delta$ spectra of the device at an incident angle of 60° to assess the optimum wavelength for significant phase and polarization modulations. As shown in Figure 19a, three important wavelengths are denoted by color bars: (i) λ_{PlC} (pink), at which the TM content of the reflected light is minimized (i.e., smallest γ); (ii) the phase-near-zero crossing wavelength (λ_{PNZ}, green), at which the static phase difference between the TE and TM components is minimized, so that the output polarization is closest to linear; (iii) a wavelength (purple) at which the reflected light has a major share of the TM component (i.e., a large γ), and meanwhile is sufficiently close to the λ_{PlC} to take advantage of the pronounced pump-induced modulation near the PlC mode. Figure 19b depicts the static polarization states of the output light at these representative wavelengths, measured using the Stokes technique and verified with ellipsometry data.

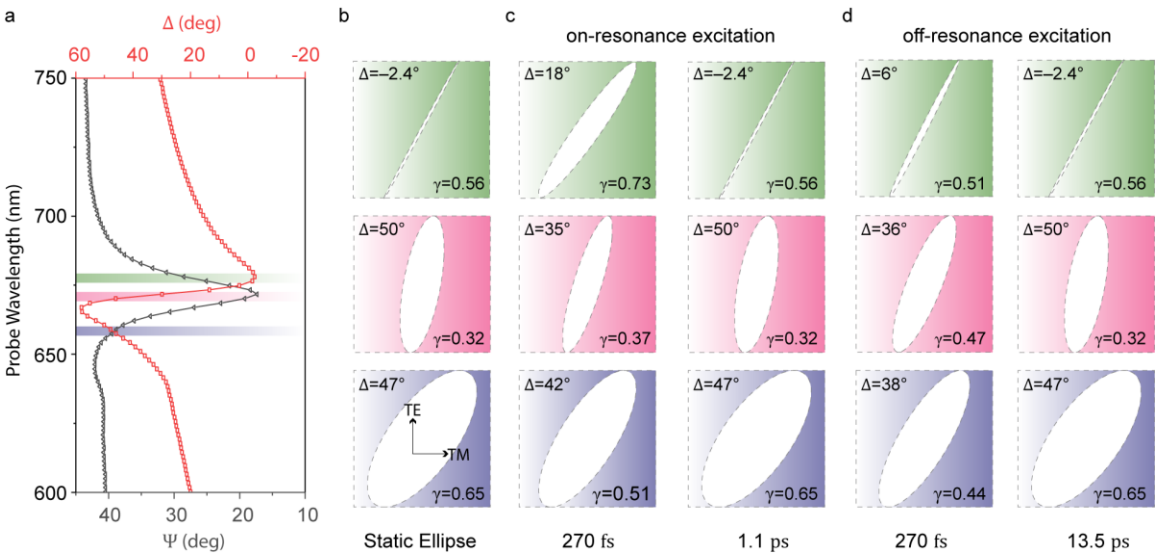

Figure 19: Dynamic tuning of the polarization state of the reflected light. (a) Static Ψ – Δ spectra measured at θ = 60°. The large spectral sensitivity of Δ at the vicinity of the λ_{PIC} originates from the narrow linewidth of the PlC mode. (b) Static (i.e., zero delay time) polarization ellipses measured at the wavelengths marked by the color bars shown in panel (a). (c) The measured polarization ellipses at delay times 270 fs and 1.1 ps following the on-resonance excitation of the plasmonic crystal. (d) The measured polarization ellipses monitored at delay times 270 fs and 13.5 ps upon the off-resonance interband pumping. The ultrafast modulation speed in panel (c) is induced by the injection of hot electrons from the gold nanoparticles into the ITO electron acceptor.

For both on- and off-resonance excitations, the transient states of the output polarization are shown in Figure 19c-d, respectively. These polarization ellipses are monitored at a delay time of ~ 270 fs to identify the ultrafast temporal response, and further characterized at longer delay times of 1.1 ps (for on-resonance excitation) and 13.5 ps (for off-resonance excitation) to elucidate recovery timeframes. At λ_{PNZ} (green), the polarization state of the output light deviates drastically from its near-linear static state, and it evolves into an elliptical one with a clockwise (counterclockwise) rotation towards the TM axis under on-resonance (off-resonance) excitation. This rotation is consistent with the increased (decreased) reflection of the TM-polarized light following the on-resonance

(off-resonance) optical pumping of the device (Figure 18c). For the case of on-resonance excitation, we observe more than 20° of optically induced modification in the phase difference between the two orthogonal electric field components (i.e., Δ), which is the primary cause of the linear-to-elliptical polarization conversion at λ_{PNZ}. At λ_{PlC} (pink), the transient output polarization displays a trend similar to that of the λ_{PNZ}, except that both on- and off-resonance excitation schemes rotate the polarization ellipses in a counterclockwise direction. At the third wavelength (purple), the output ellipse rotates counterclockwise towards the TE-axis, a direct outcome of the reduced reflection of the TM-polarized light from the plasmonic crystal, upon optical pumping.

While the observed trends in the transient rotation of polarization ellipses are implicitly explainable through the intensity modulation response of the device (Figure 3), the transient behavior of the Δ parameter needs further clarification. For all three studied representative wavelengths, the modulation trends of the Δ parameter could be qualitatively explained based on the spectral broadening of the PlC resonance and the slight redshift of λ_{PlC}. Indeed, following the introduction of the pump signal, the linewidth of the resonance mode increases, which in turn reduces the Q of the resonance, particularly at a delay time when the intensity modulation is strongest (i.e., ~270 fs). Thus, such a broadening effect significantly reduces the amount of the abrupt change near the semi-singular point in the Δ spectrum (Figure 4a) and enables a strong phase modulation at λ_{PNZ}. In our device, the modulation mechanism is primarily dominated by the spectral broadening of the PlC mode rather than its resonance shift because λ_{PlC} follows the Rayleigh diffraction mode in the air but not in the ITO layer (Figure 1b). By coating our plasmonic crystal with a thick layer of appropriate dielectric materials, such as TiO_2, we can excite the Rayleigh crystal mode

inside the coating medium, $\lambda_{PlC} = p\ (n_{coating} + Sin\theta)$. Therefore, the activation of the hot-electron transfer pathway facilitated by the on-resonance excitations, allows for an improved modulation depth with the ultrafast recovery of the output polarization in a sub-picosecond timescale. The co-existence of a significant modulation depth, ultrafast modulation speed, and spectral tunability of the operating wavelength exhibits promising potential of the proposed plasmonic platform for the all-optical control of light attributes within the visible spectrum.

In conclusion, we demonstrated the ultrafast modulation of phase, polarization, and intensity of light in the visible spectrum. For such a demonstration, we employed an array of Au nanostructures that supports a PlC mode with three key features: *i*) extremely diminished radiation loss (i.e., very high-Q); *ii*) polarization selectivity (i.e., only a TM-polarized light can be coupled to the PlC mode); *iii*) accurate spectral tunability (via adjusting the incident angle). By taking advantage of the first feature we showed that on-resonance pumping of the device enables femtosecond intensity modulation of the crystal mode assisted by the generation of hot electrons within gold nanoparticles and their subsequent injection into the surrounding ITO layer. In addition, through the combination of the first and second features we showed ultrafast polarization switching behaviors with an induced phase difference exceeding 20° between TE and TM components of light. The spectral tunability of the PlC mode (the third feature) facilitates all-optical switching of light at a wide wavelength range within the visible spectrum. Besides the demonstrated applications, our approach can be used for the experimental measurement of the nonlinearity of materials via monitoring of temporal or spectral evolution of phase and polarization upon light-mater interactions.

4.5 Details of Fabrication and Optical Characterizations

The fabrication process starts with evaporation of 10 nm/100 nm Ti/Au layers on a silicon substrate using an electron beam (e-beam) evaporator (Denton Inc.). Then a 10 nm-thick ITO layer was sputtered on the metal layers at room temperature using a RF-sputtering system (Denton Inc.). The array of gold nanoparticle was formed on top of the ITO layer in a three-step process: standard e-beam lithography (JEOL JBX – 9300FS) using Poly(methylmethacrylate) (PMMA) as the positive tone electron resist; e-beam evaporation of 2 nm/40 nm Ti/Au metal with an evaporation rate of 0.2 A°/sec; an overnight lift-off process in acetone to resolve the plasmonic crystal array.

A Woollam M-2000 ellipsometer was utilized to carry out the angle-resolved ellipsometry measurements in reflection mode. A broadband (245 – 1690 nm) linearly-polarized light at 45° illuminates the plasmonic crystal at a wide range of incident angle ($45° < \theta < 75°$, a 2°-step size). Changes in the polarization state of light upon reflection from the structure were then monitored by measuring the standard Ψ – Δ ellipsometry parameters (accuracy of the ellipsometer is $\delta\Psi = \delta\Delta = 0.015°$). To calculate the static polarization ellipses at a desired wavelength, we insert the Ψ – Δ values into the following equation:

$$\gamma^{-2}E_{TM}^2 + E_{TE}^2 - 2\gamma^{-1}E_{TM}E_{TE}\cos(\Delta) + \cos^2(\Delta) = 1,$$

where E_{TM} and E_{TE} are the electric field components of the reflected light from the structure. For the sake of comparison, all polarization ellipses are normalized to the amplitude of the TE-component of the output electric field.

The femtosecond transient reflection setup is based on a regenerative amplified Ti: Sapphire femtosecond laser system (Coherent Legend, 1 kHz repetition rate, 150 fs pulse duration, and 2.4 mJ/pulse fundamental pulse energy at 800 nm), and the data collection was conducted using a Helios spectrometer (Ultrafast Systems Inc.). A 90:10 beam splitter divides the 800 nm output light of the amplifier into two beams. The low intensity part is focused on a 2 mm thick sapphire window to generate a white light continuum (WLC) as the probe signal. To account for unwanted fluctuations, the WLC signal is divided again into two parts (70:30) to probe the sample using the 70 % portion and correct fluctuations using the 30 % portion. We focus the probe beam on the sample using a parabolic mirror and the reflected light is collected by employing an optical fiber that is coupled into a visible spectrometer equipped with a 1024 elements CMOS camera. To generate the pump signals, 1 mJ of the 800 nm fundamental beam is focused on an optical parametric amplifier (Opera coherent) and generates two tunable near-IR (NIR) pulses, signal and idler. The signal beam is then separated using a dichroic mirror and focused on a second harmonic generation BBO crystal to generate the pump beams we used for transient measurements.

The transient polarization state of light was characterized by locating a liquid crystal (LC) phase retarder and a linear polarizer (Pol) between the plasmonic crystal and the detector, as schematically shown in Figure 1a. Then we measure the intensity of the transmitted light (I_T) through the linear polarizer under four different conditions: ($\beta = 0°$, 15°, 30°, 45°; $\alpha = 0°$; $\delta = 108°$), where β and α are defined as the direction of the fast axis of the LC and the transmission axis of the linear polarizer, respectively. δ defines the induced phase difference between electric field components that are parallel and

perpendicular to the fast axis of the phase retarder. Eventually, the Stokes parameters (*I*, *M*, *C*, *S*) were retrieved from the following equation: [39]

$$I_T(\alpha,\beta,\delta) = \frac{1}{2}\{I + (M\cos 2\beta + C\sin 2\beta)\cos 2(\alpha-\beta) + [(C\cos 2\beta - M\sin 2\beta)\cos\delta + S\sin\delta]\sin 2(\alpha-\beta)\}$$

4.6 References

(1) Wurtz, G. A.; Pollard, R.; Hendren, W.; Wiederrecht, G. P.; Gosztola, D. J.; Podolskiy, V. A.Zayats, A. V.; *Nat. Nanotech.* **2011**, 6, 106-110.

(2) MacDonald, K. F.; Samson, Z. L.; Stockman, M. I.Zheludev, N. I.; *Nat. Photon.* **2009**, 3, 55-58.

(3) Pacifici, D.; Lezec, H. J.Atwater, H. A.; *Nat. Photon.* **2007**, 1, 402-406.

(4) Sim, S.; Jang, H.; Koirala, N.; Brahlek, M.; Moon, J.; Sung, J. H.; Park, J.; Cha, S.; Oh, S.; Jo, M. H.; Ahn, J. H.Choi, H.; *Nat. Commun.* **2015**, 6, 8814.

(5) Dani, K. M.; Ku, Z. Y.; Upadhya, P. C.; Prasankumar, R. P.; Brueck, S. R. J.Taylor, A. J.; *Nano Lett.* **2009**, 9, 3565-3569.

(6) Ren, M. X.; Plum, E.; Xu, J. J.Zheludev, N. I.; *Nat. Commun.* **2012**, 3, 833.

(7) Abb, M.; Wang, Y. D.; de Groot, C. H.Muskens, O. L.; *Nat. Commun.* **2014**, 5, 4869.

(8) Dintinger, J.; Robel, I.; Kamat, P. V.; Genet, C.Ebbesen, T. W.; *Adv. Mater.* **2006**, 18, 1645-1648.

(9) Taghinejad, M.; Taghinejad, H.; Xu, Z.; Liu, Y.; Rodrigues, S. P.; Lee, K. T.; Lian, T.; Adibi, A.Cai, W.; *Adv. Mater.* **2018**, 30, 17049015-17049021.

(10) Alam, M. Z.; De Leon, I.Boyd, R. W.; *Science* **2016**, 352, 795-797.

(11) Guo, P. J.; Schaller, R. D.; Ketterson, J. B.Chang, R. P. H.; *Nat. Photon.* **2016**, 10, 267-274.

(12) Guo, P. J.; Schaller, R. D.; Ocola, L. E.; Diroll, B. T.; Ketterson, J. B.Chang, R. P. H.; *Nat. Commun.* **2016**, 7, 12892.

(13) Baida, H.; Mongin, D.; Christofilos, D.; Bachelier, G.; Crut, A.; Maioli, P.; Del Fatti, N.Vallee, F.; *Phys. Rev. Lett.* **2011**, 107, 057402-057405.

(14) Voisin, C.; Del Fatti, N.; Christofilos, D.Vallee, F.; *J. Phys. Chem. B* **2001**, 105, 2264-2280.

(15) Brown, A. M.; Sundararaman, R.; Narang, P.; Schwartzberg, A. M.; Goddard, W. A.Atwater, H. A.; *Phys. Rev. Lett.* **2017**, 118, 087401-087406.

(16) Neira, A. D.; Olivier, N.; Nasir, M. E.; Dickson, W.; Wurtz, G. A.Zayats, A. V.; *Nat. Commun* **2015**, 6, 7757.

(17) Del Fatti, N.; Voisin, C.; Achermann, M.; Tzortzakis, S.; Christofilos, D.Vallée, F.; *Phys. Rev. B* **2000**, 61, 16956-16966.

(18) Mak, K. F.; He, K. L.; Shan, J.Heinz, T. F.; *Nat. Nanotech.* **2012**, 7, 494-498.

(19) Chen, Z. G.; Chen, R. Y.; Zhong, R. D.; Schneeloch, J.; Zhang, C.; Huang, Y.; Qu, F. M.; Yu, R.; Li, Q.; Gu, G. D.Wang, N. L.; *P. Natl. Acad. Sci. USA* **2017**, 114, 816-821.

(20) Koshino, M.Ando, T.; *Phys. Rev. B* **2007**, 75, 033412-033414.

(21) Kang, L.; Rodrigues, S. P.; Taghinejad, M.; Lan, S. F.; Lee, K. T.; Liu, Y. M.; Werner, D. H.; Urbas, A.Cai, W. S.; *Nano Lett.* **2017**, 17, 7102-7109.

(22) Rodrigues, S. P.; Lan, S.; Kang, L.; Cui, Y.; Panuski, P. W.; Wang, S.; Urbas, A. M.Cai, W.; *Nat. Commun.* **2017**, 8, 833.

(23) Wraback, M.Shen, H.; *Appl. Phys. Lett.* **2000**, 76, 1288-1290.

(24) Kampfrath, T.; Sell, A.; Klatt, G.; Pashkin, A.; Mahrlein, S.; Dekorsy, T.; Wolf, M.; Fiebig, M.; Leitenstorfer, A.Huber, R.; *Nat. Photon.* **2011**, 5, 31-34.

(25) Vicario, C.; Ruchert, C.; Ardana-Lamas, F.; Derlet, P. M.; Tudu, B.; Luning, J.Hauri, C. P.; *Nat. Photon.* **2013**, 7, 720-723.

(26) Yang, Y. M.; Kelley, K.; Sachet, E.; Campione, S.; Luk, T. S.; Maria, J. P.; Sinclair, M. B.Brener, I.; *Nat. Photon.* **2017**, 11, 390-396.

(27) Alam, M. Z.; Schulz, S. A.; Upham, J.; De Leon, I.Boyd, R. W.; *Nat. Photon.* **2018**, 12, 79-84.

(28) Harutyunyan, H.; Martinson, A. B. F.; Rosenmann, D.; Khorashad, L. K.; Besteiro, L. V.; Govorov, A. O.Wiederrecht, G. P.; *Nat. Nanotech.* **2015**, 10, 770-775.

(29) Sun, C. K.; Vallee, F.; Acioli, L.; Ippen, E. P.Fujimoto, J. G.; *Phys. Rev. B* **1993**, 48, 12365-12368.

(30) Zheng, B. Y.; Zhao, H. Q.; Manjavacas, A.; McClain, M.; Nordlander, P.Halas, N. J.; *Nat. Commun.* **2015**, 6, 77977.

(31) Guerrisi, M.; Rosei, R.Winsemius, P.; *Phys. Rev. B* **1975,** 12, 557-563.

(32) Sundararaman, R.; Narang, P.; Jermyn, A. S.; Goddard, W. A.Atwater, H. A.; *Nat. Commun.* **2014**, 5, 5788.

(33) Park, S.; Pelton, M.; Liu, M.; Guyot-Sionnest, P.Scherer, N. F.; *J. Phys Chem. C* **2007**, 111, 116-123.

(34) Brongersma, M. L.; Halas, N. J.Nordlander, P.; *Nat. Nanotech.* **2015**, 10, 25-34.

(35) Govorov, A. O.; Zhang, H.; Demir, H. V.Gun'ko, Y. K.; *Nano Today* **2014**, 9, 85-101.

(36) Sykes, M. E.; Stewart, J. W.; Akselrod, G. M.; Kong, X. T.; Wang, Z. M.; Gosztola, D. J.; Martinson, A. B. F.; Rosenmann, D.; Mikkelsen, M. H.; Govorov, A. O.Wiederrecht, G. P.; *Nat. Commun.* **2017**, 8, 986.

(37) Wu, K.; Chen, J.; McBride J. R.; Lian, T; *Science* **2015**, 349, 632-635.

(38) Clavero, C.; *Nat. Photon.* **2014**, 8, 95-103.

(39) Berry, H. G.; Gabrielse, G.Livingston, A. E.; *Appl. Opt.* **1977**, 16, 3200-5.

CHAPTER 5. SECOND-ORDER OPTICAL NONLINEARITIES INDUCED BY HOT-ELECTRON TRANSPORT

In previous two chapters, we discussed the impact of the generation and transport of hot electron on the third-order nonlinear response of noble metals. Considering that majority of optical materials exhibit a nonzero third-order dielectric susceptibility, the generation and transport of hot carriers primarily impacts the strength and dynamics of third-order nonlinear processes. In a sharp contrast, the existence of crystal inversion symmetry prohibits the observation of nonlinear effects of second-order type in majority of adopted optical media in the mainstream of nanophotonic technologies. It is a long-standing challenge and pressing need to break this fundamental constraint and enable second-order nonlinearities in semiconductors and oxides that dominate the optoelectronics arena. Second-order optical effects are essential to the on-demand generation of spectral components as well as the active control of light via nonlinear processes such as sum/difference-frequency generation, optical parametric amplification, and Pockels effect. In this chapter, we demonstrate sub-picosecond conversion of a statically-passive dielectric to a transient second-order nonlinear medium upon the ultrafast transfer of hot electrons. Induced by an optical switching signal, the amorphous dielectric with vanishing intrinsic $\chi^{(2)}$ develops dynamically tunable second-order nonlinear responses. By taking the second-harmonic generation as an example, we show that breaking the inversion symmetry through hot-electron dynamics can be leveraged to address the critical need for all-optical control of second-order nonlinearities in nanophotonics. Our approach can be generically

adopted in a variety of material and device platforms, offering a new class of complex nonlinear media with promising potentials for all-optical information processing.

5.1 Background, Motivation, and Design Principles

Under the electric-dipole approximation, centrosymmetric optical media exhibit a vanishing second-order nonlinear susceptibility, $\chi^{(2)}$, imposing a major challenge towards the efficient realization of second-order nonlinear processes such as second-harmonic generation (SHG), Pockels effect, optical parametric oscillation, and optical rectification [1-3]. In such materials, the atomic-scale disordered sites at surfaces and interfaces are the limited regions where the termination of the bulk crystal lattice allows for second-order nonlinear light-matter interactions, yet not in an efficient manner. Although resonant optical cavities assist promoting the surface nonlinearity through the enhancement and localization of optical fields [4-7], nevertheless, developing robust symmetry breaking techniques seems to be inevitable to enable nonlinear processes of the second-order type in the bulk of centrosymmetric media. In this context, exerting external strain, applying direct-current electric fields, and electric currents are the primary pursued techniques for breaking the inversion symmetry of centrosymmetric materials [8-15]. In the current span of the literature, however, symmetry breaking schemes via optical means are yet to develop, and initial explorations in this regard are needed to unlock the ultimate potential of nanophotonic systems for active and nonlinear optical functionalities. The importance of such developments becomes even more evident once we notice that the optical control of $\chi^{(2)}$ processes potentially paves the way towards second-order nonlinear interactions in an all-optical manner. In this study, we demonstrate that the spatially asymmetric transfer

of plasmonic hot electrons into an amorphous electron-accepting medium creates an ultrashort timeframe, during which the centrosymmetric material reveals a nonzero bulk second-order susceptibility, imitating the relaxation behavior of hot electrons in the time-domain. As an example, we show that the transient nature of the induced $\chi^{(2)}$ allows for the dynamic control of the SHG process, proving the feasibility of ultrafast all-optical manipulation of second-order nonlinearities through the transient breaking of the inversion symmetry.

The working principle of the proposed symmetry breaking technique and relevant design considerations are schematically depicted in Figure 20. In our study, we utilize a hybrid gold (Au) and amorphous TiO_2 material system, in which gold serves as an electron reservoir and the TiO_2 layer represents a prototypical centrosymmetric media that can host the transferred electrons from the gold. In this structure, the formation of a Schottky potential barrier (Φ_{br}) at the Au/TiO_2 interface blocks the intrinsic transport of electrons into the TiO_2 layer, allowing for an on-command injection of electrons upon the arrival of an optical control signal. To boost the interaction of the control light with electrons in the conduction band of gold, the metallic reservoir is tailored into an array of plasmonic nanostructures with a plasmon energy exceeding the Schottky barrier. In this scenario, the on-resonance illumination of the plasmonic structure with control laser pulses excites the plasmonic mode, which subsequently decays by elevating conduction electrons into high energy electronic states above the Fermi level (E_F) of gold. A portion of these highly energetic electrons, referred to as hot electrons, overcome the Schottky barrier and make a transition from gold reservoirs to the TiO_2 region, thereby breaking the inversion symmetry of the host layer.

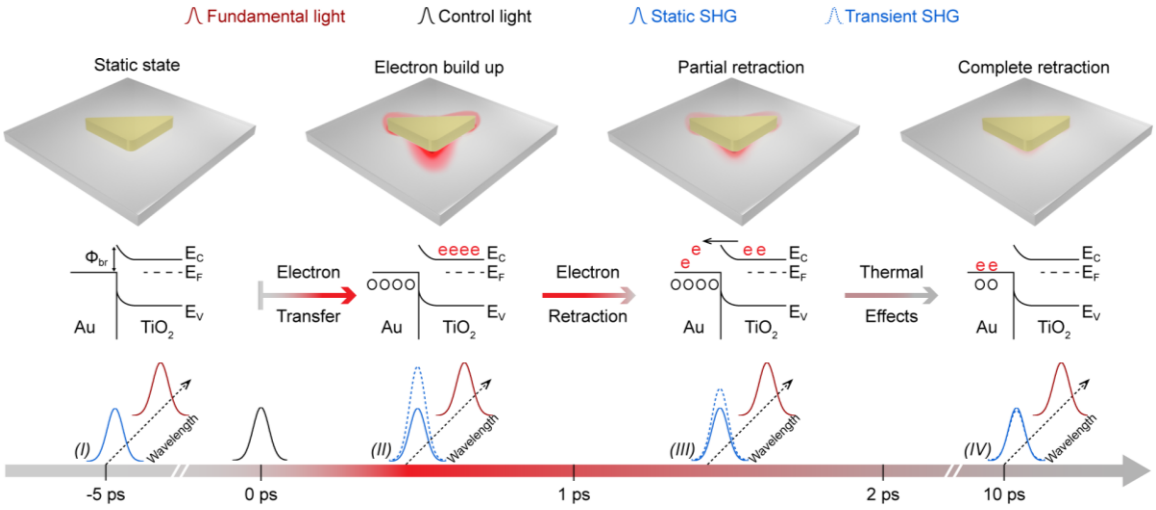

Figure 20: Breaking the inversion symmetry via hot-electron transfer. A suitable plasmonic platform made of hybrid metal/dielectric materials is required for the efficient generation and transfer of hot electrons. The on-resonance excitation of the plasmonic structure using a control beam initiates the hot-electron generation process. The ultrafast transfer of high energy electrons converts the amorphous dielectric layer into a transient nonlinear medium with an effective $\chi^{(2)}$ susceptibility that enhances the total intensity of frequency-doubled signal emitted from the structure. The induced nonlinearity vanishes as the injected electrons are retracted to the metal side of the junction.

The spatial distribution of the injected hot electrons in the electron-accepting layer, TiO_2 in the present case, follows the intensity profile of the plasmonic resonance mode [16-19]. Such a spatial correlation provides a largely oversighted opportunity to invoke plasmonic geometries with asymmetric light concentration profiles (e.g., Au triangles) for breaking the spatial symmetry of the amorphous TiO_2 film upon the nonuniform injection of hot electrons. Indeed, despite the non-existing bulk $\chi^{(2)}$ response of the TiO_2 layer, the injected hot electrons carry over the asymmetric spatial profile of the plasmon field into the amorphous layer and facilitate breaking its inversion symmetry in a transient manner. Moreover, the buildup of positive and negative charges in the metal and dielectric sides of the Schottky junction, respectively, establishes an electric field across the TiO_2 slab. The

hot-electron-induced electric field transduces the third-order dielectric susceptibility $\chi^{(3)}$ of the TiO_2 layer into an effective $\chi^{(2)}$ component that activates second-order nonlinear interactions throughout the bulk of the amorphous electron accepting film. The overall hot-electron induced $\chi^{(2)}$ response is optically enabled, with a transient response rate down to a sub-picosecond regime. The establishment of an interfacial Coulombic force naturally brings the injected electrons back to the interface for recombination with the positively charged gold nanostructures, quenching the induced $\chi^{(2)}$ response within an ultrafast characteristic timescale. Thus, the transient nature of the proposed symmetry breaking method is well suited for the ultrafast all-optical tuning of second-order nonlinear processes, as illustrated in Figure 20.

5.2 Experimental Demonstration of Symmetry Breaking via Electron Transport

To experimentally demonstrate the proposed idea in Figure 20, we fabricated a two-dimensional square array of gold triangles, separated from an optically opaque gold film via a 25 nm-thick amorphous TiO_2 layer (Figure 21a). The plasmonic array supports two major resonances at 700 and 800 nm that are exclusively accessible via two orthogonal eigenpolarizations, denoted as V and U in Figure 21b. This desired linear dichroic response allows us to use a 700 nm V-polarized laser beam (i.e., I_{Ctrl}) to control the generation of hot electrons in the gold triangles, and an 800 nm U-polarized laser beam serves as the fundamental light (i.e., I_{ω}) for monitoring the evolution of the induced transient $\chi^{(2)}$ response. In addition, the triangular shape of gold nanostructures leads to the asymmetric confinement of the electric-field profile to triangles upon the on-resonance illumination of the sample, as revealed by the simulated plasmon field profiles in Figure 21b. Since the

nonradiative decay of plasmons is the primary mechanism contributing to the plasmon-to-electron conversion, the spatial distribution of hot-electrons inside gold triangles quadratically follows the asymmetric profile of the electric field [16,17,19]. As a result, the injected electrons extend the asymmetricity of the triangle array into the statically-symmetric amorphous TiO_2 film for symmetry breaking purposes.

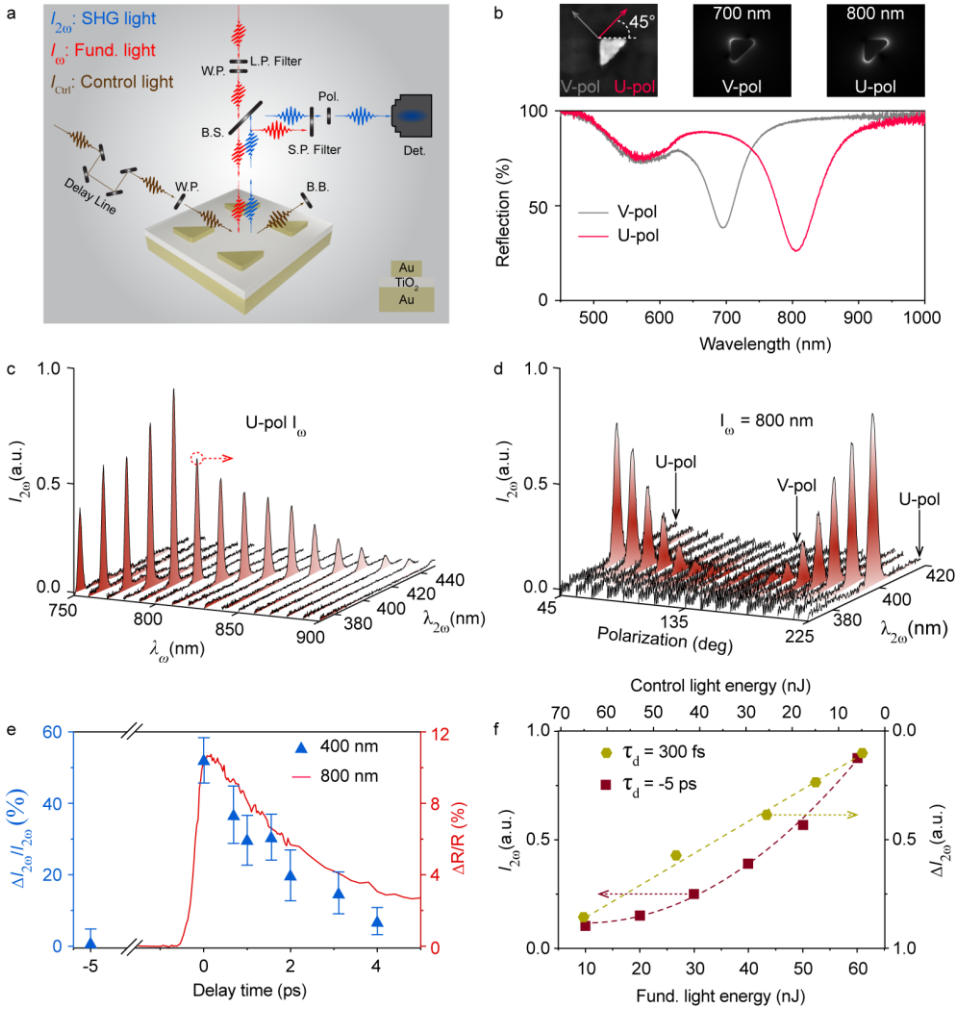

Figure 21: Static and transient second-order nonlinear characterizations of the plasmonic platform. (a) Schematic of the sample and the simplified measurement setup. (b) Static reflection spectra of the plasmonic structure for the two eigenpolarizations. The definition of polarization states (left), the simulated field profile at 700 nm (middle), and the field profile at 800 nm (right) are presented above the reflection spectra. (c) Measured static $I_{2\omega}$ spectra when the structure is excited with a U-

polarized fundamental light of varying λ_ω. (d) Dependence of the $I_{2\omega}$ signal on the polarization of the fundamental wave for λ_ω= 800 nm. (e) Temporal response of the normalized $\Delta I_{2\omega}$ and the transient reflection change ΔR upon the illumination of the structure with a V-polarized 700 nm control beam. (f) The static $I_{2\omega}$ as a function of the intensity of the fundamental wave at 800 nm (red squares) and the $\Delta I_{2\omega}$ as a function of the control beam intensity (green hexagons), monitored at τ_d = 300 fs.

Although the devised plasmonic structure comprises amorphous materials, the asymmetricity of gold triangles combined with the collective resonance response of the array yet enables frequency doubling of incident photons. To explore the static response, we collected the spectra of nonlinear optical signals $I_{2\omega}$ upon the excitation of the plasmonic array via U-polarized laser pulses with a constant intensity and varying fundamental wavelength from 750 to 900 nm. As depicted in Fig. 2c, $I_{2\omega}$ spectra exhibit a frequency-doubled behavior that peaks at $\lambda_{2\omega} = \lambda_\omega/2$ and feature an increasing efficiency as λ_ω approaches the corresponding resonance dip for the U-polarized illumination, revealing the impact of the resonance-enhanced field concentration on the SHG process. In addition, because of the linear dichroism of triangles, the harmonic generation efficiency is expected to have a strong dependence on the in-plane polarization of the incident field, particularly when the fundamental light is in resonance with the array. Indeed, our measurements (Figure 21d) show that the static nonlinear dipolar response (i.e., $\chi_s^{(2)}$) of the structure under U-polarized fundamental light is much stronger than that of V-polarized fields, a fact that declares the tensorial nature of $\chi_s^{(2)}$, as previously reported in similar structures [20,21].

We study the hot-electron induced symmetry breaking by characterizing dynamics of the second-order nonlinear interaction of a U-polarized 800 nm fundamental beam with

the plasmonic array following the hot-electron injection. In our experiment, the density of hot electrons is controlled using a 700 nm (i.e., ~ 1.77 eV) laser beam. The control light initially excites the V-polarized plasmon mode, which then nonradiatively decays via the intraband transition of the *sp*-like conduction electrons to energy states $E_F < E < E_F +$ 1.77eV. The excited electrons overcome the Au/TiO_2 injection barrier $\Phi_{br} \approx 1$ eV, making a semi-instantaneous transport from the gold to the TiO_2 layer. This interfacial charge transfer modulates the $\chi_{eff}^{(2)}$ of the device, verified by measuring the change in the intensity of the frequency-doubled nonlinear signal $\Delta I_{2\omega}$, normalized to the static SHG light $I_{2\omega}$, as a function of the delay time τ_d (Figure 21e, blue triangles). These measurements reveal that, despite a notable reduction in the absorption of the 800 nm fundamental light (Figure 21e, red line), the hot-electron transfer enables enhancing $I_{2\omega}$ by ~ 55%. The induced $\Delta I_{2\omega}$ occurs in a timescale shorter than 300 fs and monotonically decays in 5 ps, manifesting the creation of a transient second-order nonlinear medium that transduces the dynamic of the hot-electron transfer process into the temporal evolution of the SHG response. Although the static $I_{2\omega}$ quadratically scales with I_ω, the maximum induced $\Delta I_{2\omega}$, occurring at τ_d = 300 fs, shows a linear dependence on I_{Ctrl} (Figure 21f). Such a linear dependence suggests that characterizing the dynamic of second-order optical processes can be considered as a promising alternative to time-resolved absorption techniques for evaluating hot-electron transient dynamics [22].

The hot-electrons density has a major impact on the strength of transiently induced second-order nonlinear response. Increasing the population of electrons within the TiO_2 film facilitates breaking the inversion symmetry of the amorphous host layer via the asymmetric injection of hot electrons. Moreover, the strength of the transient electric field

E_{tr} formed across the TiO_2 film directly impacts the transient nonlinearity of the plasmonic structure. Indeed, the hot-electron induced E_{tr} by acting on the third-order susceptibility $\chi^{(3)}$ of TiO_2 produces an effective second-order nonlinear response that can be described as $E_{\mathrm{tr}}\chi^{(3)}(2\omega;\omega,\omega,0)$. The combined contribution of the asymmetric hot-electron transfer and the transient field effect leads to the formation of a transient $\Delta\chi_{\mathrm{tr}}^{(2)}$ that is linearly tunable via I_{Ctrl}. The total emitted SHG light from the plasmonic platform is expressed as $I_{2\omega} \propto I_{\omega}^{2}\left|\chi_{\mathrm{s}}^{(2)} + \Delta\chi_{\mathrm{tr}}^{(2)}\right|^{2}$, which benefits from the contribution of the bulk TiO_2 film as well. The modulation magnitude of the SHG signal can be expressed as $\Delta I_{2\omega} \propto I_{\omega}^{2}\Delta\chi_{\mathrm{tr}}^{(2)}[2\chi_{\mathrm{s}}^{(2)} + \Delta\chi_{\mathrm{tr}}^{(2)}]$. Comparing this relation with the $\Delta I_{2\omega}$ vs. I_{Ctrl} curve in Figure 21f implies that the leading term in the $\Delta I_{2\omega}$ relation holds the major contribution to the modulation of $I_{2\omega}$. Such a linear trend is consistence with strong static $\chi_{\mathrm{s}}^{(2)}$ of the asymmetric triangle array under U-polarized illuminations, dominating the impact of $2\chi_{\mathrm{s}}^{(2)}$ term over that of $\Delta\chi_{\mathrm{tr}}^{(2)}$ in the $\Delta I_{2\omega}$ relation.

5.3 Design and Characterization of a Control Structure

In addition to enabling the generation and injection of hot electrons, the application of the control beam also modulates the linear optical response of the plasmonic array. The combination of hot-electron transfer and Kerr-like optical nonlinearity transiently modifies the refractive index of gold, a change that often weakens resonance effects on the blue side of the static resonance of plasmonic structures [23-26]. Consequently, it is expected to witness a decrease in the efficiency of the nonlinear light generation from resonant systems. In our case, the competing influences of the hot-electron symmetry breaking effect and the

refractive index change complicate the evaluation of the exact impact of the electron injection on the achievable $\Delta I_{2\omega}$. To unravel such complexities, we designed a control sample that exhibits a linear optical response (Figure 22a) resembling that of the TiO_2-incorporated structure, but the electron accepting layer is replaced with an Al_2O_3 film to block the electron transfer ($\Phi_{br} \approx 2.6$ eV [23,24]). We utilize a V-polarized 700 nm pump light and a U-polarized broadband probe beam to characterize the impact of refractive index change on the linear response of the control device. The transient reflection map (Figure 22b) shows a decrease in the light absorption at the spectral vicinity of 800 nm, leading to ~ 25% reduction in $I_{2\omega}$, a change that qualitatively follows our expectation based on the measured ~ 10% change in the absorption of I_{ω} (the red curve in Figure 22c). Therefore, the origin of the observed $\Delta I_{2\omega}$ is primarily governed by the modulation of the linear plasmonic response (i.e., spectral redshift) rather than the direct modification of the intrinsic dielectric susceptibilities of comprising materials, as previously reported for bulk media [27-29]. Moreover, the kinetic of the induced $\Delta I_{2\omega}$ closely follows the relaxation of the linear reflection at 800 nm, which is dominated by the thermalization of confined hot electrons in gold triangles via electron-phonon interactions [23,31].

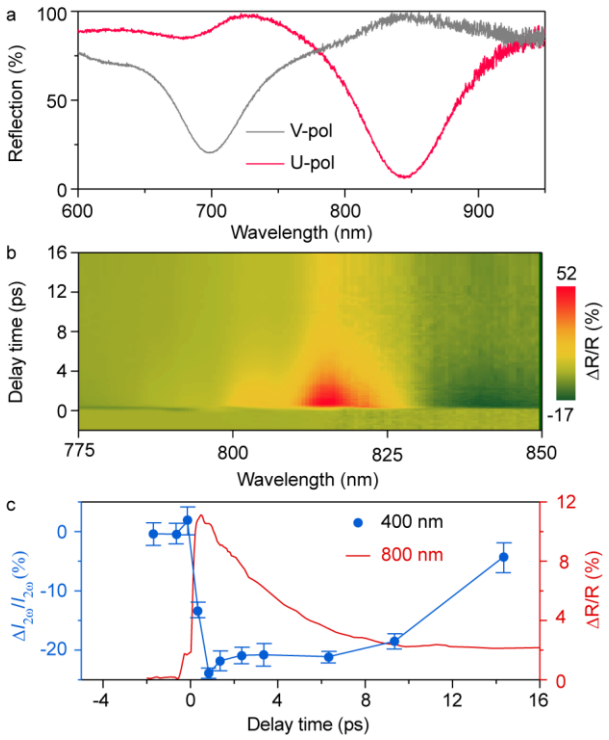

Figure 22: Dynamic of the second-order nonlinear response without the involvement of the hot-electron transfer. (a) Polarized static optical reflection spectra of the control sample. (b) Two-dimensional transient reflection map acquired using a U-polarized broadband probe light upon the excitation of the structure with a 700 nm V-polarized control light. The intensity of the control light is set to provide an absolute reflection change equal to that of the TiO_2-incorporated sample. (c) Dynamics of the normalized second-harmonic change $\Delta I_{2\omega}$ and the induced linear reflection change ΔR in the control sample in the absence of the hot-electron transport.

Comparing the nonlinear transient behavior of the main and control samples exposes two subtle, yet critical, roles of hot-electron transfer on the active tuning of nonlinear processes. First, the injection of high-energy electrons into the amorphous TiO_2 film converts this statically-passive layer into a second-order transient nonlinear medium that, contrary to the case of the control sample, leads to the enhancement of the effective $\chi^{(2)}$ response. Second, the dynamic of the electron transfer facilitates achieving an intrinsically fast modulation speed that is beyond the characteristics of thermal processes in optically

perturbed noble metals. In addition, since the refractive index change has a similar impact on the linear response of the TiO_2-incorporated device, the actual SHG change stemmed from the hot-electron transfer should be larger than what we observed in Figure 21e. As seen from the measured polar diagrams of the absolute reflection change in Figure 23b, optical excitation of plasmonic array lowers the absorption of V- and U-polarized beams at 700 and 800 nm, respectively. Therefore, the observed ~ 8% reduction in the absorption of 800 nm (i.e., I_ω) enforces the damping of the SHG output by ~ 20%. Considering that $\Delta I_{2\omega}^{\text{total}} \approx \Delta I_{2\omega}^{\text{hot-e}} + \Delta I_{2\omega}^{\text{n-change}}$, we can roughly estimate the contribution of the hot-electron transfer on the modulation of the second-harmonic signal to be ~ 75%, yielding an intensity-dependent nonlinear modulation rate of ~ 1.3% per nanojoule. This nonlinear generation rate can be notably improved by increasing the hot-electron generation and injection efficiencies in an optimized structure, for instance, by approaching the near infrared regime [16,19,32,33] or utilizing subradiant dark plasmonic modes [19,32].

5.4 Tensorial Components of the Optically Induced Transient $\chi^{(2)}$

We experimentally examined the output polarization state of the frequency-doubled light before and after the injection of hot electrons into the TiO_2 layer. Given that the V-polarized component of the fundamental wave at λ_ω = 800 nm cannot effectively contribute to the SHG process (Figure 21d), during these measurements we fix the input polarization of the fundamental beam to the U-state. Moreover, since the fundamental beam is illuminated on the sample at a normal incident angle, only the in-plane U and V polarizations are considered as the possible orientations of the field components at the 2ω frequency. Figure 23c depicts the polar diagram of $I_{2\omega}^{j}$ as a function of the output

polarization *j*, at -5 ps and 300 fs delay times, corresponding to the static and transient conditions, respectively. In both cases, the dominancy of $I_{2\omega}^{V}$ over $I_{2\omega}^{U}$ indicates that the $\chi_{\mathrm{VUU}}^{(2)}$ element of the second-order susceptibility tensor dictates the output polarization state of the SHG signal, which is perpendicular to that of the fundamental field. This behavior originates from the mirror symmetry of the triangle array with respect to the V axis, which forbids U-polarized nonlinear emissions, as such a symmetry condition diminishes the $\chi_{\mathrm{UUU}}^{(2)}$ element.

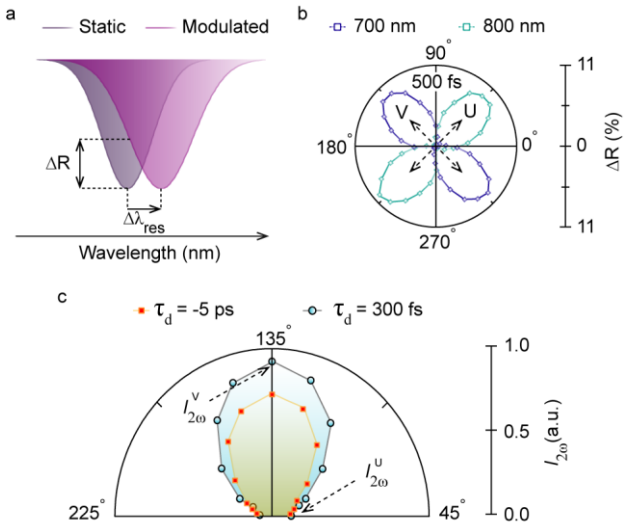

Figure 23: Transient linear and nonlinear polarization responses. (a) Effect of the refractive index change of gold on the spectral lineshape of resonance modes, illustrated schematically. (b) Polar diagrams of the absolute reflection change at 700 and 800 nm, as a function of the polarization angle, induced using a control light intensity identical to what we used for acquiring the transient SHG response in Figure 21e. (c) Polar diagrams revealing the polarization state of the emitted frequency-doubled light before (τ_{d} = -5 ps) and after (τ_{d} = 300 fs) the hot-electron transfer into the TiO_2 film, when the fundamental beam being polarized along the U-direction.

The transient breaking of the inversion symmetry based on hot-electron dynamic has enabled a powerful scheme for the creation and active tuning of effective $\chi^{(2)}$ responses,

in amorphous materials and centrosymmetric crystals where the intrinsic $\chi^{(2)}$ nonlinearity vanishes. Thanks to the ultrafast generation, transport, and decay of hot carriers, second-order nonlinear processes such as frequency doubling, sum-frequency generation, and optical parametric oscillation can be enabled in hybrid plasmonic systems, mitigating the conventional constraint imposed by the strict requirement of non-inversion-symmetry.

5.5 Details of Fabrication and Optical Characterizations

The fabrication process starts with the electron-beam (e-beam) evaporation (Denton Inc.) of the 10 nm/100 nm Ti/Au stack on a silicon substrate, followed by the plasma-assisted atomic layer deposition (ALD) of a 25 nm-thick TiO2 layer at 250 °C using a Cambridge Fiji Plasma ALD system. Afterwards, the gold triangle array was formed on top of the TiO2 layer in a three-step fabrication process: (i) the standard e-beam lithography (Elionix ELS G-100) to define the gold plasmonic structure, (ii) the e-beam evaporation of 2 nm/45 nm Ti/Au metal, and (iii) the lift-off process in acetone to resolve the plasmonic array. For the lithography step, we used poly(methyl methacrylate) (PMMA) as the positive tone electron resist. The periodicity of the array and the side length of the right-angle triangles were designed to be 70 nm and 300 nm, respectively. For the case of the control sample, we used a 10 nm-thick ALD deposited alumina (i.e., Al2O3) layer instead of the TiO2. To obtain a linear dichroic response similar to that of the main sample, the periodicity and the side length of Au triangles of the control sample were adjusted to 95 nm and 380 nm, respectively.

The transient-reflection and time-resolved SHG measurement system is based on a regenerative amplified Ti:sapphire femtosecond laser system (Coherent Legend, 1 KHz

repetition rate, 150 fs pulse duration, and 2.4 mJ/pulse fundamental pulse energy at 800 nm), and the data collection was conducted using a Helios spectrometer (Ultrafast Systems Inc.). An 80:20 beam splitter divides the 800 nm output light of the amplifier into two beams. The low intensity part is focused on a 2 mm-thick sapphire crystal to generate a broadband white light continuum (WLC) as the probe signal, and then collimated by a parabolic mirror. The WLC passes through a broadband half waveplate (Thorlabs) to adjust the polarization state of light during transient measurements. To account for unwanted fluctuations, the WLC signal is further divided into two beams (50:50) to probe the plasmonic structure using one half and correct the laser fluctuations via the other half. The probe beam is focused on the surface of our sample via a long working distance (WD) and a large-numerical-aperture (NA) objective (Mitutoyo 50x objective, 0.55 NA, 133 mm WD). This objective was chosen to make sure we can simultaneously meet requirements of transient reflection and time-resolved SHG measurements. The reflected probe light from the sample is collected using the same objective and travels back to the 50:50 beam splitter. The collected WLC light for both the reference and the optical-information carrying signals are then coupled into an optical fiber, transmitted to a spectrometer, and eventually to a 1024 CMOS detector where the optical data is processed using a Helios ultrafast system. The control pulse for the generation of hot electrons and modification of the refractive index is generated from an optical parametric amplifier (Opera Coherent). The delay between the control beam and the probe light is controlled by a motorized delay stage (Thorlabs). In the time-resolved SHG characterization, the optical path is essentially the same as that of the transient reflection measurement, except that we remove the sapphire plate to convert the probe light into an 800 nm fundamental beam. The SHG signal

is collected by a large-core optical fiber bundle and is then coupled into a liquid-nitrogen cooled CCD detector (1340x100 pixels, PyLoN, Princeton Instruments) after passing through a 400 nm band-pass filter (Thorlabs). The delay time is controlled by the same system as in the transient-reflection characterizations.

For the static SHG measurements, we use a Ti:sapphire ultrafast oscillator (Spectra-Physics Mai Tai HP; pulse duration: 100 fs; repetition rate: 80 MHz) as the excitation source. The fundamental wavelength was tuned from 750 to 900 nm with a step interval of 10 nm to obtain the spectral dispersion of the SHG response depicted in the manuscript. The output beam from the laser source first passes through a long-pass filter to prevent any high-frequency residue from entering the collection path of our system. A set of Glan polarizers and half waveplates is utilized to control the state of polarization and the excitation power. After passing through a beam splitter, the fundamental beam is directed towards the sample mounted on an inverted optical microscope (Zeiss, Axio Observer D1m) with a 20x and NA = 0.5 objective. The emitted SHG signal is then collected using the same objective and sent back to the beam splitter. We use a bandpass filter in front of our spectrometer to prevent the collection of the fundamental light. The detection system comprises a monochromator (Princeton Instruments, IsoPlane) followed by a CCD camera (Princeton Instruments, Pixis 400).

5.6 References

[1] M. Kauranen, A. V. Zayats, Nonlinear plasmonics. *Nat. Photonics* **6**, 737-748 (2012).

[2] K. O'Brien, H. Suchowski, J. Rho, A. Salandrino, B. Kante, X. B. Yin, X. Zhang, Predicting nonlinear properties of metamaterials from the linear response. *Nat. Mater.* **14**, 379-383 (2015).

[3] A. Nahata, A. S. Weling, T. F. Heinz, A wideband coherent terahertz spectroscopy system using optical rectification and electro-optic sampling. *Appl. Phys. Lett.* **69**, 2321-2323 (1996).

[4] M. W. Klein, C. Enkrich, M. Wegener, S. Linden, Second-harmonic generation from magnetic metamaterials. *Science* **313**, 502-504 (2006).

[5] S. Kim, J. H. Jin, Y. J. Kim, I. Y. Park, Y. Kim, S. W. Kim, High-harmonic generation by resonant plasmon field enhancement. *Nature* **453**, 757-760 (2008).

[6] S. Linden, F. B. P. Niesler, J. Forstner, Y. Grynko, T. Meier, M. Wegener, Collective effects in second-harmonic generation from split-ring-resonator arrays. *Phys. Rev. Lett.* **109**, 015502 (2012).

[7] V. K. Valev, N. Smisdom, A. V. Silhanek, B. De Clercq, W. Gillijns, M. Ameloot, V. V. Moshchalkov, T. Verbiest, Plasmonic ratchet wheels: switching circular dichroism by arranging chiral nanostructures. *Nano Lett.* **9**, 3945-3948 (2009).

[8] M. Cazzanelli, F. Bianco, E. Borga, G. Pucker, M. Ghulinyan, E. Degoli, E. Luppi, V. Veniard, S. Ossicini, D. Modotto, S. Wabnitz, R. Pierobon, L. Pavesi, Second-harmonic generation in silicon waveguides strained by silicon nitride. *Nat. Mater.* **11**, 148-154 (2012).

[9] B. Chmielak, C. Matheisen, C. Ripperda, J. Bolten, T. Wahlbrink, M. Waldow, H. Kurz, Investigation of local strain distribution and linear electro-optic effect in strained silicon waveguides. *Opt. Express* **21**, 25324-25332 (2013).

[10] C. Schriever, F. Bianco, M. Cazzanelli, M. Ghulinyan, C. Eisenschmidt, J. de Boor, A. Schmid, J. Heitmann, L. Pavesi, J. Schilling, Second-order optical nonlinearity in silicon waveguides: Inhomogeneous stress and interfaces. *Adv. Opt. Mater.* **3**, 129-136 (2015).

[11] O. A. Aktsipetrov, A. A. Fedyanin, A. V. Melnikov, E. D. Mishina, A. N. Rubtsov, M. H. Anderson, P. T. Wilson, M. ter Beek, X. F. Hu, J. I. Dadap, M. C. Downer, dc-electric-field-induced and low-frequency electromodulation second-harmonic generation spectroscopy of Si(001)-SiO2 interfaces. *Phys. Rev. B* **60**, 8924-8938 (1999).

[12] K. T. Lee, M. Taghinejad, J. Yan, A. S. Kim, L. Raju, D. K. Brown, W. Cai, Electrically Biased Silicon Metasurfaces with Magnetic Mie Resonance for Tunable Harmonic Generation of Light. ACS Photonics 6, 2663-2670 (2019).

[13] E. Timurdogan, C. V. Poulton, M. J. Byrd, M. R. Watts, Electric field-induced second-order nonlinear optical effects in silicon waveguides. *Nat. Photon.* **11**, 200-207 (2017).

[14] Taghinejad, M.; Cai, W. S. Field- and Carrier-Induced Nonlinear Metamaterials. Conference on Lasers and Electro-Optics (CLEO) (2018).

[15] A. B. Ruzicka, L. K. Werake, G. Xu, J. B. Khurgin, E. Y. Sherman, J. Z. Wu, H. Zhao Second-harmonic generation Induced by electric currents in GaAs. *Phy. Rev. Lett.* **108**, 077403 (2012).

[16] M. E. Sykes, J. W. Stewart, G. M. Akselrod, X. T. Kong, Z. M. Wang, D. J. Gosztola, A. B. F. Martinson, D. Rosenmann, M. H. Mikkelsen, A. O. Govorov, G. P. Wiederrecht, Enhanced generation and anisotropic Coulomb scattering of hot electrons in an ultra-broadband plasmonic nanopatch metasurface. *Nat. Commun.* **8**, 986 (2017).

[17] A. O. Govorov, H. Zhang, H. V. Demir, Y. K. Gun'ko, Photogeneration of hot plasmonic electrons with metal nanocrystals: Quantum description and potential applications. *Nano Today* **9**, 85-101 (2014).

[18] A. O. Govorov, H. Zhang, Kinetic density functional theory for plasmonic nanostructures: Breaking of the plasmon peak in the quantum regime and generation of hot electrons. *J. Phys. Chem. C* **119**, 6181-6194 (2015).

[19] M. Taghinejad, W. Cai, All-optical control of light in micro- and nanophotonics. *ACS Photonics* **6**, 1082-1093 (2019).

[20] B. K. Canfield, H. Husu, J. Laukkanen, B. F. Bai, M. Kuittinen, J. Turunen, M. Kauranen, Local field asymmetry drives second-harmonic generation in noncentrosymmetric nanodimers. *Nano Lett.* **7**, 1251-1255 (2007).

[21] R. Czaplicki, J. Makitalo, R. Siikanen, H. Husu, J. Lehtolahti, M. Kuittinen, M. Kauranen, Second-harmonic generation from metal nanoparticles: resonance enhancement versus particle geometry. *Nano Lett.* **15**, 530-534 (2015).

[22] K. Wu, J. Chen, J. R. McBride, T. Lian, T. Efficient hot-electron transfer by a plasmon-induced interfacial charge-transfer transition. *Science* **349**, 632-635 (2015).

[23] M. Taghinejad, H. Taghinejad, Z. Xu, K.-T. Lee, S. P. Rodrigues, J. Yan, A. Adibi, T. Lian, W. Cai, Ultrafast control of phase and polarization of light expedited by hot-electron transfer. *Nano Lett.* **18**, 5544-5551 (2018).

[24] M. Taghinejad, W. Cai, All-Optical Modulation of Ultrasharp Lattice Plasmons. IEEE Photon. Conf., 647-648 (2017).

[25] H. Baida, D. Mongin, D. Christofilos, G. Bachelier, A. Crut, P. Maioli, N. Del Fatti, F. Vallee, Ultrafast nonlinear optical response of a single gold nanorod near its surface plasmon resonance. *Phys. Rev. Lett.* **107**, 057402 (2011).

[26] A. M. Brown, R. Sundararaman, P. Narang, A. M. Schwartzberg, W. A. Goddard, H. A. Atwater, Experimental and ab initio ultrafast carrier dynamics in plasmonic nanoparticles. *Phys. Rev. Lett.* **118**, 087401 (2017).

[27] C. Guo, G. Rodriguez, A. J. Taylor, Ultrafast dynamics of electron thermalization in gold. *Phy. Rev. Lett.* **86**, 1638-1641 (2001).

[28] P. Maldonado, K. Carva, M. Flammer, P. M. Oppeneer, Theory of out-of-equilibrium ultrafast relaxation dynamics in metals. *Phys. Rev. B* **96**, 174439 (2017).

[29] D. H. Son, J. S. Wittenberg, U. Banin, A. P. Alivisatos, Second harmonic generation and confined acoustic phonons in highly excited semiconductor nanocrystals. *J. Phys. Chem. B* **110**, 19884-19890 (2006).

[30] C. Voisin, N. Del Fatti, D. Christofilos, F. Vallee, Ultrafast electron dynamics and optical nonlinearities in metal nanoparticles. *J. Phys. Chem. B* **105**, 2264-2280 (2001).

[31] N. Del Fatti, C. Voisin, M. Achermann, S. Tzortzakis, D. Christofilos, F. Vallee, Nonequilibrium electron dynamics in noble metals. *Phys. Rev. B* **61**, 16956-16966 (2000).

[32] M. L. Brongersma, N. J. Halas, P. Nordlander, Plasmon-induced hot carrier science and technology. *Nat. Nanotechnol.* **10**, 25-34 (2015).

[33] R. Sundararaman, P. Narang, P.; A. S. Jermyn, W. A. Goddard, H. A. Atwater, Theoretical predictions for hot-carrier generation from surface plasmon decay. *Nat. Commun.* **5**, 5788 (2014).

CHAPTER 6. COHERENT CONTROL OF EXCITONIC SECOND-ORDER NONLINEARITIES IN TRANSITION METAL DICHALCOGENIDES

Second-order optical nonlinearities are essential for the active control of light matter interactions and on-demand generation of new spectral components via nonlinear processes such as Pockels effect, sum/difference frequency generation, optical parametric amplification, and optical rectifications. For example, at the terahertz frequency gap (i.e., ~ 0.1-10 THz), difference frequency generation and optical rectification are among the cornerstones of existing technologies for the realization of terahertz sources. Successful demonstration of such critical optical functionalities is highly correlated to the existence of a strong second-order dielectric susceptibility, $\chi^{(2)}$, response in available optical media. Despite the immense importance of second-order nonlinear processes, the portfolio of $\chi^{(2)}$ materials is rather limited as the crystal inversion symmetry in most optical media prevents achieving a non-zero $\chi^{(2)}$ response, under electric-dipole approximation. Therefore, introducing reliable optical methods that facilitate controlling the effective $\chi^{(2)}$ response of noncentrosymmetric materials or allow for inducing effective second-order nonlinear behaviors would be transformative to pave the road for the realization of ultrafast functional components and subsequently high-speed data processing platforms. Within the context of this PhD thesis, we divided the existing optical materials into two major categories: (i) transparent optical materials such as high band gap oxides; (ii) semiconductor media, capable of absorbing electromagnetic waves at a certain spectral range. In previous chapter, we introduced an optical technique for breaking the inversion

symmetry in centrosymmetric transparent materials via the semi-instantaneous transport of hot electrons. In this chapter we propose and experimental demonstrate an optical method for controlling the second-order nonlinearity of noncentrosymmetric and absorptive optical materials. We employ monolayers of transition metal dichalcogenides as a representative example to showcase the possibility of optical control of over the $\chi^{(2)}$ response in excitonic materials. Atomically thin transition metal dichalcogenides (TMDs) in their excited states can serve as exceptionally small building blocks for active optical platforms. In this scheme, optical excitation provides a practical approach to control the interaction between light and TMDs via the photocarrier generation, in an ultrafast manner. Here, we demonstrate the ultrafast modulation of second-order optical nonlinearities in monolayer MoS_2 films via the optical tuning of the photocarrier density. Our combined experimental and theoretical study illustrates that the depopulation of the conduction band electrons, at the vicinity of the high-symmetry *K/K′* points of the momentum space, suppresses the contribution of interband electronic transitions to the effective $\chi^{(2)}$ of the monolayer crystal. Therefore, the intensity of the emitted second-harmonic light from MoS_2 can be substantially modulated by controlling the density of generated photocarriers, in a timeframe as short as ~ 250 fs, in an all-optical manner. The observed strong correlation between the kinetics of photocarriers and the temporal response of optical nonlinearity suggests that time-resolved nonlinear measurements can be utilized as an alternative technique for investigating the material properties of TMDs in their optically excited states.

6.1 Background, Motivation, and Design Principles

Excited states of active optical media enable exotic light-matter interactions with unprecedented functionalities that can be dynamically controlled via external stimuli in an electrical or all-optical manner.[1-5] For instance, although within the context of linear optics a large bandgap dielectric naturally acts as a transparent material in the infrared regime, the optical excitation of photoelectrons circumvents such transparency by facilitating intraband electronic transitions upon the absorption of infrared photons. Therefore, the excited states of such dielectrics enable optical switching, even within their transparency window.[1,6-10] In addition, the thermodynamic tendency of excited electrons to return to a ground-state condition upon the termination of external stimuli, inherently adds the element of time-dependency to the exotic response of excited media. The formation of excited charge carriers induces a transient change in material properties, namely linear and nonlinear indices of refraction, activating a category of ultrafast optical processes that are unlikely to happen through the interaction of light with the static form of matter.[1] Among various applications, all-optical switching – controlling attributes of light with light – is perhaps the most important functionality, which primarily relies on the interaction of light with the excited states of active materials. The span of active media for optical switching covers a wide range of metals,[1,11-15] conductive oxides,[1,16-19] dielectrics,[1,20-24] and organic materials,[25,26] utilized either in bulk formats or tailored as miniaturized device platforms. Besides device footprint considerations, miniaturizing optical media significantly boosts the sensitivity of material attributes to the density of optically excited photocarriers, facilitating the implementation of low-energy optical switches.

Approaching the length of atomic bonds is indeed the extreme case of miniaturization, which is primarily offered by the family of two-dimensional (2D) and 1D materials.[27, 28] As the foremost member of this family, graphene has been vastly employed for optical switching in a variety of configurations, at the near- to mid-infrared regime.[29-31] Since graphene possesses a relatively low electron heat capacity and zero bandgap, the optical creation of a non-equilibrium carrier distribution results in the ultrafast tuning of its indices of refraction and therefore, the optical modulation of light-graphene interactions. Transition metal dichalcogenides (TMDs) are the semiconducting counterpart of graphene with a nonzero electronic bandgap ranging from 1 to 2.5 eV.[30,32,33] This category of 2D crystals comprises a hexagonal plane of metal atoms sandwiched between two hexagonal planes of chalcogen atoms, distributed in a trigonal prismatic lattice. Contrary to their bulk counterparts, monolayers of TMDs develop a direct bandgap that can eliminate the involvement of the phonon emission/absorption during the interband electronic transitions. Thusly, the impact of the photocarrier generation on the manipulation of material properties in atomically thin TMDs is several orders of magnitude stronger than their bulk counterparts.[34-37] In addition, owing to the noncentrosymmetric crystal structure, monolayers of TMDs exhibit a large second-order dielectric susceptibility, $\chi^{(2)}$, facilitating the efficient realization of second-order nonlinear processes such as second-harmonic generation (SHG), sum-frequency generation, and optical parametric amplification. The promising potential of TMD crystals for the demonstration of active optical platforms has been a major driving force behind the prolific spectral and temporal characterization of such materials in optically excited states.[38-41] The current extent of the literature, however, is mostly limited to the study of photocarrier dynamics to promote the understanding of

linear light-TMDs interactions. Nonetheless, the kinetics of $\chi^{(2)}$ based nonlinear processes during the temporal evolution of photocarriers in optically excited TMDs demands further explorations. Understanding such ultrafast mechanisms brings us closer the ultimate potentials of low dimensional materials for the active control of linear and nonlinear properties of light.

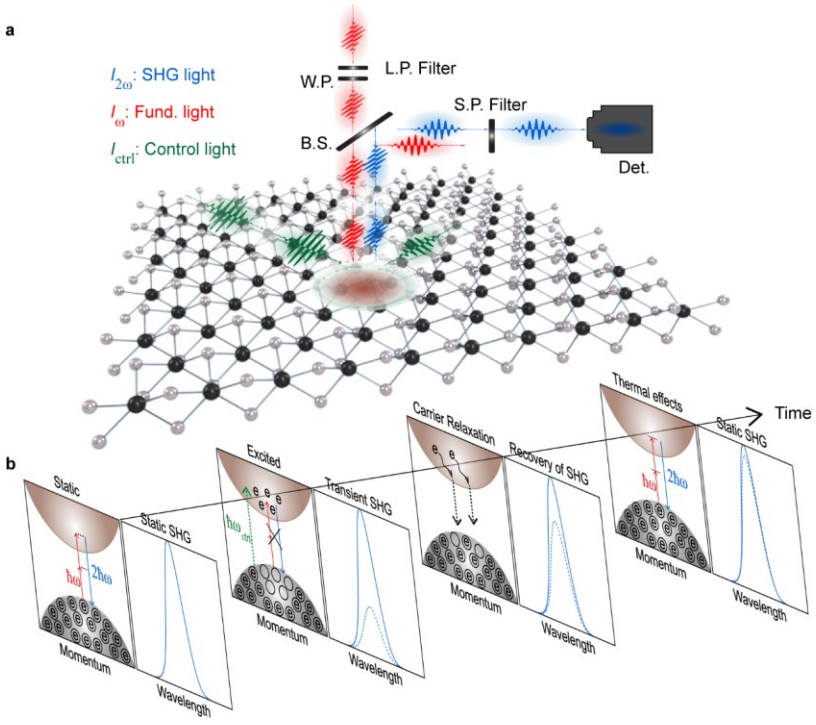

Figure 24: Transient evolution of second-order nonlinear processes in optically excited TMDs. (a) Schematic representation of the experimental setup. A control light (green laser pulses), launched at an incident angle of 60°, excites photocarriers in a monolayer TMD film. For time-resolved linear and nonlinear characterizations, a broadband probe light or an 800 nm fundamental beam (red pulses) interacts with the optically excited monolayer film. (b) Transient correlation between $\chi_{\text{eff}}^{(2)}$ of TMDs and the photoexcited charge carriers. Control photons depopulate the valance band of monolayer crystal and create a non-equilibrium electron system in the conduction band that damps the interband two-photon transitions around the K/K′ point within the momentum space. Therefore, an ultrafast decrease in $\chi_{\text{eff}}^{(2)}$ is observed. The decay of photocarriers naturally brings the excited

TMD film back to its ground state, facilitating the recovery of the second-order dielectric susceptibility, and therefore, the all-optical modulation of the $I_{2\omega}$ signal.

This part of my PhD research, through a set of transient linear and nonlinear characterizations, we demonstrate the ultrafast modulation of second-order optical nonlinearities in a monolayer TMD film via the optical tuning of the photocarrier density. Our investigations show that the creation of photoelectrons substantially lowers the possibility of interband electronic transitions around the high-symmetry *K/K′* points in the momentum space, diminishing the efficiency of nonlinear frequency doubling upon the interaction of light with the excited monolayer crystal. We show that such an opportunity allows us to optically tune the intensity of the emitted SHG signal from TMDs, kinetics of which closely follows the formation/relaxation dynamics of photocarriers. Figure 24 schematically depicts the working principle behind the optical tuning of the effective $\chi^{(2)}$ response of an atomically thin TMD crystal as well as our characterization approach. Initially, ultrashort pulses of a control beam elevate the monolayer TMD film into an excited state by generating non-equilibrium photocarriers, the density of which is tunable via the intensity (I_{ctrl}) and energy ($\hbar\omega_{\mathrm{ctrl}}$) of control photons. The simultaneous reduction in the density of electrons in the valance band and unoccupied electronic states in the conduction band synergistically lowers the possibility of interband transitions via the absorption of two fundamental photons, leading to the quenching of the effective $\chi^{(2)}_{\mathrm{eff}}$ response of the 2D material in its excited state. Under such a circumstance, the detected intensity of the second-harmonic signal ($I_{2\omega}$) significantly drops as a result of the photocarrier generation by the control beam. Upon the elimination of the control light, the excited TMD crystal gradually relaxes back to the ground state through a series of carrier-

carrier and carrier-lattice interactions, as will be discussed later. Therefore, the correlation between the density of photocarriers and the $\chi_{\text{eff}}^{(2)}$ response of the monolayer crystal enforces the $I_{2\omega}$ signal to follow a time trace imitating the kinetic of the excited carriers. Such an inherent correlation not only enables the ultrafast all-optical control of $\chi^{(2)}$-based nonlinear processes, but also provides a promising alternative to time-resolved absorption techniques for evaluating carrier dynamics in TMDs.

6.2 Intrinsic Second-Order Nonlinearity of MoS_2

Motivated by their widespread use, chemical-vapor-deposition (CVD)-grown molybdenum disulfide (MoS_2) crystals are exploited to investigate the described concept in Figure 24. We limit the scope of our study to monolayer films to inhibit the observation of complex dynamic responses in the linear and nonlinear light-MoS_2 interactions, arising from the stacking order and rotational alignment in multilayer films. We identify monolayer crystals via a combination of photoluminescence, Raman, and atomic force microscopy. Figure 25a depicts acquired static second-harmonic signals, following the illumination of a monolayer region via 120 femtosecond (fs) laser pulses of a varying fundamental wavelength, λ_ω, ranging from 750 to 950 nm with a constant intensity. In addition, a few representative nonlinear images of MoS_2 crystals with various shapes and geometries are shown in Figure 25b. The measured $I_{2\omega}$ spectra reveal frequency-doubled peaks at $\lambda_{2\omega} = \lambda_\omega/2$, the intensity of which quadratically scales with that of the fundamental light (inset, Figure 2a). Although the crystal symmetry holds a major impact on the efficiency of $\chi^{(2)}$ based optical processes, the dispersive nature of the measured $I_{2\omega}$ across the presented wavelength range implies the involvement of other effects in the frequency-

doubling response of MoS_2 monolayers. Contrary to noncentrosymmetric oxides, the feasibility of electronic/excitonic transitions in semiconductors allows for enhancing the efficiency of optical nonlinearities via resonant processes, either at λ_ω or $\lambda_{2\omega}$.[38,42] Considering that monolayers of MoS_2 support A, B, and C excitonic transitions at ~ 670, 615, and 425 nm wavelengths, at the spectral vicinity of these wavelengths the SHG signal can be notably boosted. Indeed, the spectral trend illustrated in Figure 2a shows that $I_{2\omega}$ peaks at $\lambda_{2\omega} \approx 425$ nm, confirming the resonance boosting of the $\chi^{(2)}_{\text{eff}}$ at the C exciton of MoS_2, where the band nesting effect enhances the excitonic density of states (DOS). Our results are consistent with previous reports on the static SHG response of exfoliated MoS_2 flakes with various odd number of layers.[38]

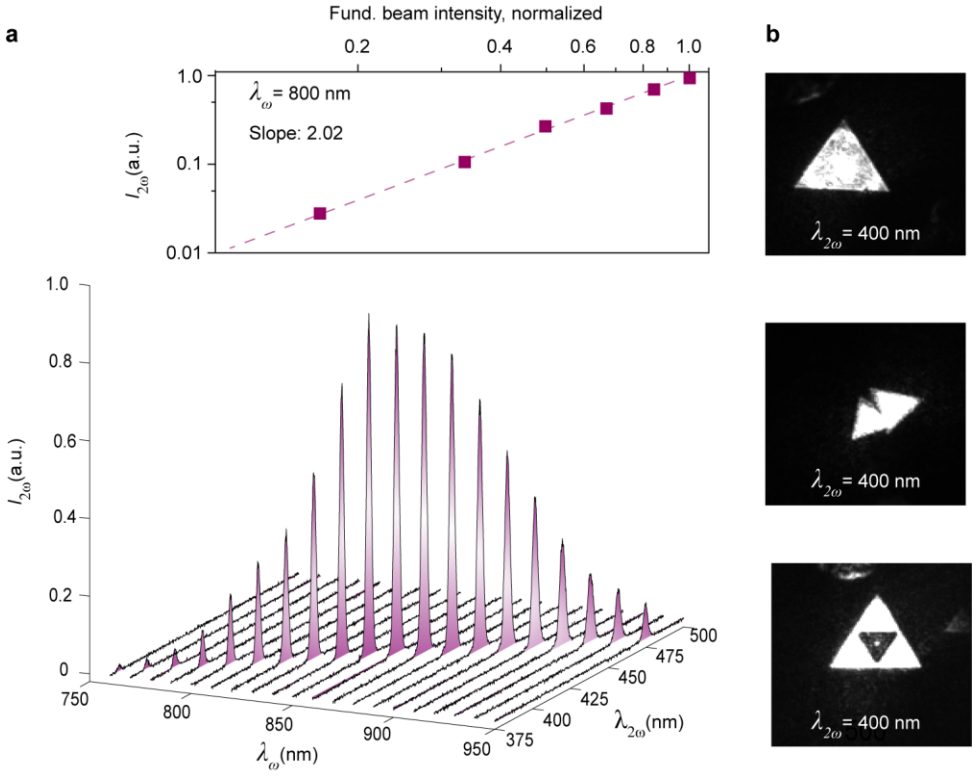

Figure 25: Static second-order nonlinear response of monolayer MoS_2 crystals. (a) Measured nonlinear $I_{2\omega}$ spectra of a single layer MoS_2 film, excited via a varying fundamental wavelength

λ_ω with a constant intensity. The strong SHG signal close to $\lambda_{2\omega}$ = 425 nm stems from the enhanced density of states around the C exciton band. As depicted in the inset, the intensity of frequency-doubled light scales quadratically with that of the fundamental beam. (b) Second-order nonlinear imaging of MoS_2 flakes recorded at the second-harmonic wavelength 400 nm. The emitted $I_{2\omega}$ light is strong at single layer regions and suddenly disappears at double layer regions (e.g., central area, the bottom image).

6.3 Optical Control of Excitonic Second-Order Nonlinearities in MoS_2

To elucidate the impact of photocarriers on the SHG response of MoS_2, we conduct a set of linear and second-order nonlinear time-resolved measurements in which, a broad probe beam or an 800 nm fundamental light (i.e, I_ω) interacts with a monolayer crystal, at various timeframes before and after the photoexcitation (characterization setup, Figure 24). For these measurements two excitation wavelengths are exploited by setting λ_{ctrl} to 500 and 600 nm. Under the latter condition, the energy of control photons, $E_{\mathrm{ctrl}} \approx 2.05$ eV, lays between the excitonic bandgap of MoS_2, $E_{\mathrm{g}}^{\mathrm{exc}} \approx 1.85$ eV, and the electronic bandgap of monolayers, $E_{\mathrm{g}}^{el} \approx 2.3$ eV. Therefore, the 600 nm control light primarily populates the A and B excitons in the MoS_2 film. However, under the λ_{ctrl} = 500 nm excitation, in addition to the creation of excitonic species, control photons have sufficient energy, $E_{\mathrm{ctrl}} \approx 2.5$ eV, to generate free electrons in the conduction band of MoS_2, as will be discussed later. Figure 26a depicts a 2D map of the modulated optical density (ΔOD) of the reflected light from a monolayer MoS_2 crystal, induced via the 500 nm control beam. The induced change in the linear spectral response, monitored at delay time τ_{d} = 250 fs (Figure 26b), shows two negative ΔOD signals around 670 and 610 nm probe wavelengths, revealing the bleaching of the light absorption at the A- and B-exciton energy levels, respectively. Such an absorption bleaching stems from a combination of the band filling effect at the *K/K′* points

of the momentum space, as well as the spectral shift and broadening of the excitonic resonances through the generation of photocarriers.[43,44] A similar ΔOD lineshape is observed when the MoS_2 film is excited close to the B excitonic resonance via the 600 nm control light, indicating that the nature of the absorption bleaching effect does not evolve with the energy of the excitation photons. The absorption bleaching of the excitonic energy levels decays following the relaxation of the photocarriers, as shown in Figure 26c. The relaxation kinetics can be described based on a three-exponential function with characteristic decaying time constants of 0.37 ± 0.1, 4.87 ± 1.1, and 82.2 ± 3.9 ps. The fast, intermediate, and slow relaxation components are consistent with expected kinetics of the carrier thermalization, exciton trapping via mid-bandgap defect states, and the interband carrier-phonon scattering, respectively.[43-46]

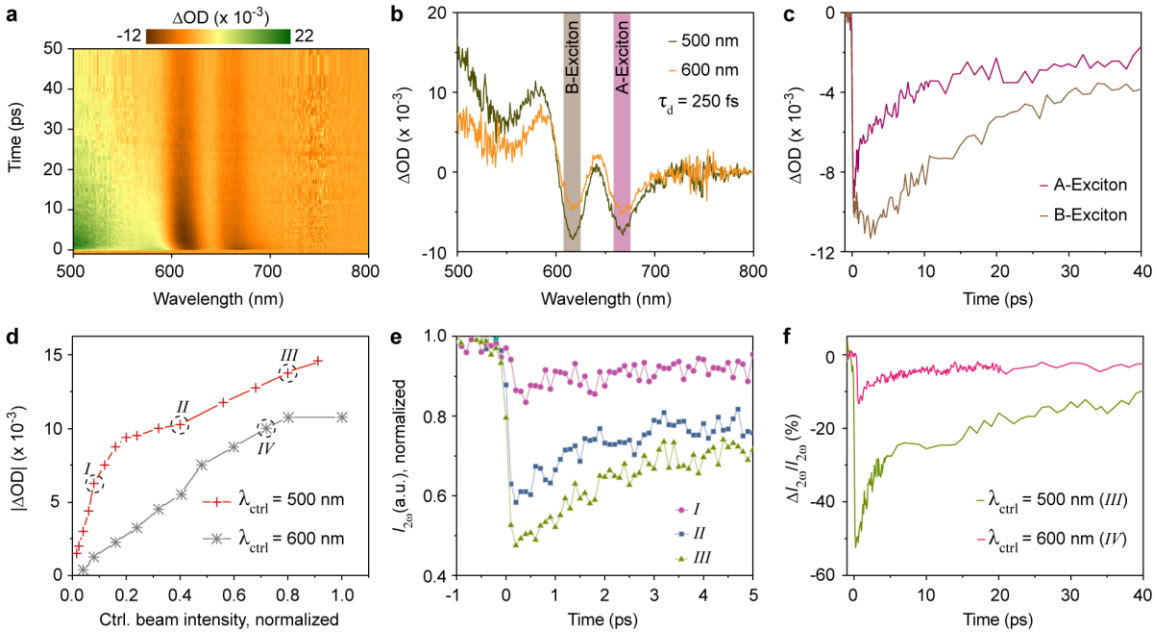

Figure 26: Kinetics of linear and nonlinear light-matter interactions in monolayer MoS_2 crystals. (a) A representative transient reflection map acquired upon the excitation of a single layer MoS_2 film with control pulses of 500 nm wavelength. The creation of photocarriers modulates the absorption of light by the MoS_2 film particularly at the spectral vicinity of A- and B exciton bands.

(b) Spectral response of ΔOD monitored at τ_d = 250 fs, induced by photocarrier generation using 500 and 600 nm control beams. Under both excitation wavelengths, bleaching of the absorption at A and B exciton levels is observed. (c) Relaxation dynamics of A and B excitons in a monolayer MoS_2 crystal for the case of λ_{ctrl} = 500 nm. (d) The induced |ΔOD| of A exciton as a function of the control beam intensity for λ_{crtl} = 500 and 600 nm, monitored at τ_d = 250 fs. (e) Temporal response of $I_{2\omega}$ at $\lambda_{2\omega}$ = 400 nm upon the illumination of the MoS_2 flake with 500 nm laser pulses of varying intensities. (f) A comparison between the transient SHG response of MoS_2 under illumination with 500 and 600 nm control light.

Although the modulated linear response of the MoS_2 crystal under both excitation wavelengths displays similar trends, the induced ΔOD signals at the excitonic energy levels (e.g., A exciton) reveal disparate correlations to the intensity of the two control signals (Figure 26d). Under the weak excitation regime, increasing the intensity of the control beams leads to a linear modulation of the excitonic photobleaching, with a stronger modulation for the case of λ_{ctrl} = 500 nm. At the intermediate excitation regime by increasing I_{ctrl}, however, the |ΔOD| signal develops a sub-linear trend for λ_{ctrl} = 500 nm, indicating the saturation of the photobleaching effect, while the saturation of ΔOD occurs at larger intensities under the λ_{ctrl} = 600 nm excitation. Such a difference between the intensity responses primarily stems from the difference between the absorption coefficients of MoS_2 at each excitation wavelength.[47] Indeed, since the static light absorption at 500 nm is stronger than that of 600 nm, the saturation of the excitonic photobleaching occurs at a smaller I_{ctrl}, for the 500 nm excitation wavelength. This explanation is consistent with the observation of the photobleaching saturation at an approximately similar |ΔOD| level (i.e., $\sim 11 \times 10^{-3}$), under both 500 and 600 nm excitations. We note that the photobleaching saturation level is limited by DOS and can be reached at a sufficiently large I_{ctrl}, the absolute value of which varies based on the photon energy in the control signal.

Interestingly, for the case of λ_{ctrl} = 500 nm, by increasing I_{ctrl} beyond the onset of the saturation level, a secondary linear trend, that is absent under λ_{ctrl} = 600 nm, comes to the picture. We assign this linear response to the optical creation of free electrons in the electronic conduction band of MoS_2 around the *K/K′* points in the momentum space. As we explained above, the photon energy of the 500 nm control beam is larger than the electronic bandgap of MoS_2 and therefore, upon the saturation of excitonic levels, increasing I_{ctrl} primarily leads to the free carrier generation rather than the formation of A or B-type excitons. It is important to mention that, during the performed time-resolved measurements we limit the intensity of the control beam close to a level that leads to the saturation of the magnitude of the photobleaching (i.e., $\sim 11 \times 10^{-3}$). Such a constraint allows us to prevent the contribution of high-field effects (e.g., bandgap renormalization) in modulating the nonlinear response of MoS_2 and therefore, safely study the impact of photocarriers on the second-order nonlinear interaction of light with a monolayer crystal.

We study the all-optical control of the frequency-doubling by characterizing the dynamics of the second-order nonlinear interaction of an 800 nm fundamental beam with an optically excited MoS_2 crystal, at various delay times before and after the formation of photocarriers. Figure 3e exhibits the temporal evolution of $I_{2\omega}$, upon the illumination of the 500 nm control beam on the monolayer MoS_2 film, with varying intensities. Indeed, the control over I_{ctrl} facilitates accurate tuning of the number of generated photocarriers, allowing to monitor the impact of photocarriers on the effective $\chi^{(2)}$ of MoS_2. As seen, in a timescale shorter than 200 fs, the transient nonlinear signal reveals a fast intensity drop, the amount of which scales with the intensity of the control beam. Subsequently, the recovery of the SHG signal towards the static response of unexcited monolayer MoS_2 is

observed, which stems from the decay of photocarriers back to ground states. As shown in Figure 26f, the creation of the photocarriers via the control beam significantly modulates the relative second-order nonlinear response of MoS_2, $\Delta I_{2\omega}/I_{2\omega}$, more than 55%, in an all-optical and ultrafast fashion. Similarly, the excitation of the MoS_2 film with λ_{ctrl} = 600 nm also causes the suppression of the SHG signal; however, in this case the maximum achievable change in the relative intensity of the SHG signal is less than 15%. Under both excitation wavelengths, induced $\Delta I_{2\omega}$ exhibits similar relaxation kinetics comprising of a fast decaying component, 3.9 ± 0.4 ps, followed by a transient tail as slow as 74.7 ± 2.8 ps. Comparing the magnitude of $\Delta I_{2\omega}$ under 500 and 600 nm excitations provides valuable insights on the microscopic correlation of photocarriers and the $\chi^{(2)}_{\mathrm{eff}}$ of MoS_2. To do so, we consider two representative intensities corresponding to points II and IV, denoted on Figure 26d, as the I_{ctrl} for 500 and 600 nm beams, respectively. Such a selection guarantees that the monolayer crystal experiences equal photobleaching, $\sim 11 \times 10^{-3}$ OD, independent of λ_{crtl}. Apparently, under 500 nm excitation the absolute value of induced $|\Delta I_{2\omega}|$ is more than three times larger than that of the 600 nm control light (Figure 26f), implying the dominant role of photoelectrons, that are difficult to create via 600 nm photons, on the modulation of $\chi^{(2)}_{\mathrm{eff}}$.

6.4 Understanding the Underlying Physics of Transient $\chi^{(2)}$ Response of MoS_2

We further substantiate the proposed mechanism for the modulation of the SHG signal by investigating the dependency of $I_{2\omega}$ on the intensities of the fundamental and control beams, at the 250 fs delay time, which corresponds to the maximum SHG intensity change. As illustrated in Figure 27a, when the intensity of the control beam (λ_{ctrl} = 500

nm) is fixed, the intensity of the frequency-doubled signal quadratically scales with that of the fundamental beam, as expected. However, the calculation of $|\Delta I_{2\omega}/I_{2\omega}|$ leads to an approximately constant relative modulation depth, ~ 13%, indicating that the optical tuning of the $\chi_{\text{eff}}^{(2)}$ of MoS_2 exclusively occurs via the formation of photocarriers upon the illumination of the control light. This observation is further corroborated through a survey of the dependence of $\Delta I_{2\omega}$ on the control light intensity (i.e., number of generated photocarriers), while I_{ω} is constant (Figure 27b). Within a weak optical excitation regime, the $\Delta I_{2\omega}$ vs I_{ctrl} curve in Figure 27b exhibits a linearly decreasing trend, however, as we increase the intensity of the control light the modulation of $I_{2\omega}$ becomes saturated. For a qualitative understanding of the observed saturation effect, we can look at the simplified version of the second-order dielectric function of a nonlinear optical material and its association with the density of photocarriers (and thus with I_{ctrl}). For the case of nonresonant ω and 2ω frequencies, which applies to our measurement condition:[48]

$$\chi_{abc}^{(2)}(-2\omega;\omega,\omega) \propto \frac{ie^3}{\hbar^2\omega^3}\sum_{\Omega=\pm\omega}\sum_{lmn}\int dk\,(f_l - f_n)\frac{v_{nl}^a v_{lm}^b v_{mn}^c}{(\omega_n - \omega_m - 2\Omega - i\eta)(\omega_n - \omega_l + \Omega - i\eta)} \qquad (1)$$

where e, $\hbar$, k, f, η, and v are the elementary electron charge, Planck's constant, wave number, occupation number, resonance broadening coefficient, and the velocity matrix elements, respectively. In this equation l, m, and n indices identify the possible energy states that may contribute into second-order nonlinear interactions, as denoted on the band diagram of MoS_2 in Figure 27c. Upon optical excitations from the l to m state, the number of available electrons in the valance band l decreases (i.e., $f_l < 1$) and, accordingly, the density of electrons in the conduction band m increases (i.e., $f_m > 0$). Based on the rate equation we can relate the number of available electrons in the valance band, N_l, to I_{ctrl}:

$$N_l = \frac{N_0}{1 + \tau_0 B_{\mathrm{lm}} I_{\mathrm{ctrl}}} \qquad (2)$$

where N_0, τ_0, and B_{lm} represent the static density of electrons, carrier lifetime, and the Einstein coefficient for optical absorption from l to m. Considering that $N_l = g(\varepsilon) f_l(\varepsilon)$, where $g(\varepsilon)$ is the density of states, the combination of Eq. (1) and Eq. (2) provides a direct correlation between the intensity of the second-harmonic signal and that of the control light:

$$I_{2\omega} \propto [1 - 2(\tau_0 B_{lm} I_{\mathrm{ctrl}}) + 3(\tau_0 B_{lm} I_{\mathrm{ctrl}})^2 + \cdots] \qquad (3)$$

This equation qualitatively shows that at small I_{ctrl}, the optically induced $\Delta I_{2\omega}$ linearly drops as we increase the intensity of the control beam. However, the quadratic term in Eq. (3) becomes stronger as the material experiences stronger excitations, which saturates the impact of the control beam on the modulation of the SHG signal. Therefore, the general nonlinear power-dependency observed in Figure 27b stems from the saturation of the photocarrier generation at high control beam intensities. In our study, we do not consider the impact of photoinduced phonon emission on the nonlinear interaction of light with MoS_2. However, Kim et al have comprehensively studied the interplay between the acoustic phonons, generated via the nonradiative decay of excitons, and the dynamics of second-order nonlinear processes in MoS_2 films.[49]

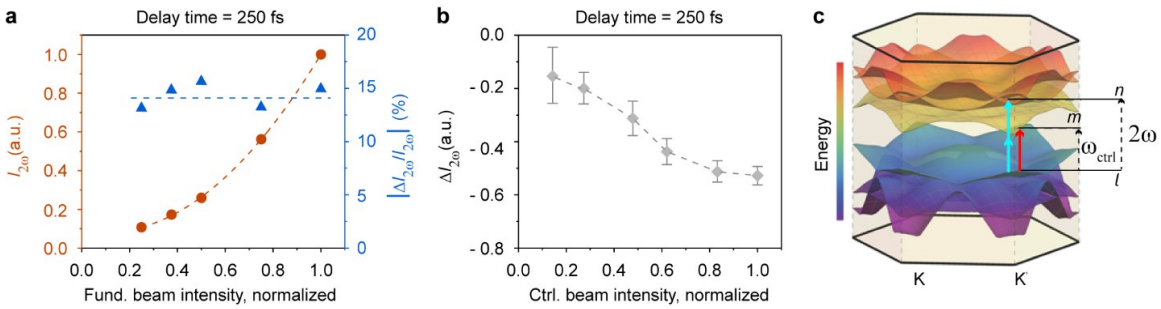

Figure 27: Dependency of the frequency doubling response of MoS_2 to the intensities of control and fundamental beams. (a) The intensity of the emitted SHG signal as a function of the fundamental beam intensity (left axis) measured at τ_d = 250 fs, while the monolayer MoS_2 crystal is illuminated with a 500 nm control light with a constant intensity. For each I_ω, the normalized change in the SHG signal $\Delta I_{2\omega}/I_{2\omega}$ is calculated and plotted on the right axis (blue triangles). (b) Modulation of the SHG signal as a function of the control beam intensity. For these measurements, the intensity of the fundamental light is fixed. The $\Delta I_{2\omega}$ vs. I_{ctrl} curve initially exhibits a linear trend and then reveals a saturation behavior as the intensity of the control beam increases. (c) Electronic band structure of monolayer MoS_2 in the first Brillouin zone. l, m, and n indices represent possible energy states participating in linear and nonlinear transitions.

The transient formation of photoelectrons has enabled a powerful scheme for the active control of the effective $\chi^{(2)}$ response of monolayer transition metal dichalcogenides. Thanks to the strong light absorption, thermodynamic decay of excited carriers to their ground states, and the correlation between $\chi^{(2)}_{eff}$ and the photocarriers density, TMDs offer a self-sustained material platform that allows for accurate control of second-order nonlinear processes such as harmonic generation and optical parametric amplification, at an atomic level. Besides switching purposes, the observed optical modulation of SHG suggests that characterizing the temporal evaluation of $\chi^{(2)}_{eff}$ can be considered as an alternative time-domain measurement approach to study the kinetics of photocarriers in atomically thin TMD crystals.

6.5 References

[1] M. Taghinejad, W. Cai, ACS Photonics 2019, 6, 1082.

[2] S. K. Sundaram, E. Mazur, Nat. Mater. 2002, 1, 217.

[3] J. R. Schaibley, H. Yu, G. Clark, P. Rivera, J. S. Ross, K. L. Seyler, W. Yao, X. Xu, Nat. Rev. Mater. 2016, 1, 16055.

[4] X. Xu, W. Yao, D. Xiao, T. F. Heinz, Nat. Phys. 2014, 10, 343.

[5] O. Reshef, I. De Leon, M. Z. Alam, R. W. Boyd, Nat. Rev. Mater. 2019, 4, 535.

[6] R. Dekker, N. Usechak, M. Forst, A. Driessen, J. Phys. D 2007, 40, R249.

[7] V. R. Almeida, C. A. Barrios, R. R. Panepucci, M. Lipson, Nature 2004, 431, 1081.

[8] M. Sheikbahae, D. C. Hutchings, D. J. Hagan, E. W. Vanstryland, IEEE J. Quantum Elect. 1991, 27, 1296.

[9] E. W. Van Stryland, M. A. Woodall, H. Vanherzeele, M. J. Soileau, Opt. Lett. 1985, 10, 490.

[10] M. Taghinejad, Z. Xu, K.-T. Lee, T. Lian, W. Cai, Transient Second-Order Nonlinear Media: Breaking the Spatial Symmetry in the Time Domain via Hot-Electron Transfer. Phys. Rev. Lett. 2019, In press.

[11] O. Hess, J. B. Pendry, S. A. Maier, R. F. Oulton, J. M. Hamm, K. L. Tsakmakidis, Nat. Mater. 2012, 11, 573.

[12] N. Del Fatti, C. Voisin, M. Achermann, S. Tzortzakis, D. Christofilos, F. Vallee, Phys. Rev. B 2000, 61, 16956.

[13] C. Voisin, N. Del Fatti, D. Christofilos, F. Vallee, J. Phys. Chem. B 2001, 105, 2264.

[14] M. Taghinejad, H. Taghinejad, Z. Xu, K. T. Lee, S. P. Rodrigues, J. Yan, A. Adibi, T. Lian, W. Cai, Nano Lett. 2018, 18, 5544.

[15] M. Taghinejad, H. Taghinejad, Z. Xu, Y. Liu, S. Rodrigues, K. Lee, T. Lian, A. Adibi, W. Cai, Adv. Mater. 2018, 30, 1704915.

[16] M. Z. Alam, I. De Leon, R. W. Boyd, Science 2016, 352, 795.

[17] P. Guo, R. D. Schaller, J. B. Ketterson, R. P. H. Chang, Nat. Photonics 2016, 10, 267.

[18] L. Caspani, R. P. Kaipurath, M. Clerici, M. Ferrera, T. Roger, J. Kim, N. Kinsey, M. Pietrzyk, A. Di Falco, V. M. Shalaev, A. Boltasseva, D. Faccio, Phys. Rev. Lett. 2016, 116, 233901.

[19] P. Guo, R. D. Schaller, L. E. Ocola, B. T. Diroll, J. B. Ketterson, R. P. H. Chang, Nat. Commun. 2016, 7, 12892.

[20] B. R. Bennett, R. A. Soref, J. A. Delalamo, IEEE J. Quantum Elect. 1990, 26, 113.

[21] M. Sheik-Bahae, D. J. Hagan, E. W. Van Stryland, Phys. Rev. Lett. 1990, 65, 96.

[22] K. Nozaki, T. Tanabe, A. Shinya, S. Matsuo, T. Sato, H. Taniyama, M. Notomi, Nat. Photonics 2010, 4, 477.

[23] M. R. Shcherbakov, S. Liu, V. V. Zubyuk, A. Vaskin, P. P. Vabishchevich, G. Keeler, T. Pertsch, T. V. Dolgova, I. Staude, I. Brener, A. A. Fedyanin, Nat. Commun. 2017, 8, 17.

[24] M. Taghinejad, H. Taghinejad, M. Abdolahad, S. Mohajerzadeh, Nano Lett. 2013, 13, 889.

[25] A. Fratalocchi, G. Assanto, Appl. Phys. Lett. 2005, 86, 051109.

[26] C. Koos, P. Vorreau, T. Vallaitis, P. Dumon, W. Bogaerts, R. Baets, B. Esembeson, I. Biaggio, T. Michinobu, F. Diederich, W. Freude, J. Leuthold, Nat. Photonics 2009, 3, 216.

[27] Gharooni, M.; Hosseini, M.; Mohajerzadeh, S.; Taghinejad, M.; Taghinejad, H.; Abdi, Y. Realization of highly crystallographic three-dimensional nanosheets by a stress-induced oriented-diffusion method. Appl. Phys. Lett. 105, 043110 (2014).

[28] Taghinejad, H.; Taghinejad, M.; Abdolahad, M.; Saeidi, A.; Mohajerzadeh, S. Fabrication and modeling of high sensitivity humidity sensors based on doped silicon nanowires. *Sensor Actuat B-Chem* **176**, 413-419 (2013).

[29] W. Li, B. Chen, C. Meng, W. Fang, Y. Xiao, X. Li, Z. Hu, Y. Xu, L. Tong, H. Wang, W. Liu, J. Bao, Y. R. Shen, Nano Lett. 2014, 14, 955.

[30] S. Yu, X. Wu, Y. Wang, X. Guo, L. Tong, Adv. Mater. 2017, 29, 1606128.

[31] Q. Bao, H. Zhang, Y. Wang, Z. Ni, Y. Yan, Z. X. Shen, K. P. Loh, D. Y. Tang, Adv. Funct. Mater. 2009, 19, 3077.

[32] H. Taghinejad, A. A. Eftekhar, A. Adibi, Opt. Mater. Express 2019, 9, 1590.

[33] H. Taghinejad, A. A. Eftekhar, P. M. Campbell, B. Beatty, M. Taghinejad, Y. Zhou, C. J. Perini, H. Moradinejad, W. E. Henderson, E. V. Woods, X. Zhang, P. Ajayan, E. J. Reed, E. M. Vogel, A. Adibi, Strain Relaxation via Formation of Cracks in Compositionally Modulated Two-Dimensional Semiconductor Alloys. Npj 2D Mater. Appl. 2018, 2, 1−8.

[34] M. Y. Tsai, A. Tarasov, Z. R. Hesabi, H. Taghinejad, P. M. Campbell, C. A. Joiner, A. Adibi, E. M. Vogel, ACS Appl. Mater. Inter. 2015, 7, 12850.

[35] G. Wang, S. Zhang, X. Zhang, L. Zhang, Y. Cheng, D. Fox, H. Zhang, J. N. Coleman, W. J. Blau, J. Wang, Photonics Res. 2015, 3, A51.

[36] H. Taghinejad, M. Taghinejad, A. A. Eftekhar, Z. Li, M. P. West, M. H. Javani, S. Abdollahramezani, X. Zhang, M. Tian, T. Johnson-Averette, P. M. Ajayan, E. M. Vogel, S.-F. Shi, W. Cai, A. Adibi, ACS Nano 2020, 14, 6323–6330.

[37] M. Claassen, C. Jia, B. Moritz, T. P. Devereaux, Nat. Commun. 2016, 7, 13074.

[38] L. M. Malard, T. V. Alencar, A. P. M. Barboza, K. F. Mak, A. M. de Paula, Phys. Rev. B 2013, 87, 201401 .

[39] D. Li, W. Xiong, L. Jiang, Z. Xiao, H. R. Golgir, M. Wang, X. Huang, Y. Zhou, Z. Lin, J. Song, S. Ducharme, L. Jiang, J. F. Silvain, Y. Lu, ACS Nano 2016, 10, 3766.

[40] Z. Sun, A. Martinez, F. Wang, Nat. Photonics 2016, 10, 227.

[41] H. Yu, D. Talukdar, W. Xu, J. B. Khurgin, Q. Xiong, Nano Lett. 2015, 15, 5653.

[42] G. Wang, X. Marie, I. Gerber, T. Amand, D. Lagarde, L. Bouet, M. Vidal, A. Balocchi, B. Urbaszek, Phys. Rev. Lett. 2015, 114.

[43] H. Shi, R. Yan, S. Bertolazzi, J. Brivio, B. Gao, A. Kis, D. Jena, H. G. Xing, L. Huang, ACS Nano 2013, 7, 1072.

[44] S. Sim, J. Park, J. G. Song, C. In, Y. S. Lee, H. Kim, H. Choi, Phys. Rev. B 2013, 88, 075434.

[45] H. Taghinejad, D. A. Rehn, C. Muccianti, A. A. Eftekhar, M. Tian, T. Fan, X. Zhang, Y. Meng, Y. Chen, T. V. Nguyen, S. F. Shi, P. M. Ajayan, J. Schaibley, E. J. Reed, A. Adibi, ACS Nano 2018, 12, 12795.

[46] H. Taghinejad, A. A. Eftekhar, P. M. Campbell, B. Beatty, M. Taghinejad, Y. Zhou, C. J. Perini, H. Moradinejad, W. E. Henderson, E. V. Woods, X. Zhang, P. Ajayan, E. J. Reed, E. M. Vogel, A. Adibi, NPJ 2D Mater. Appl. 2018, 2, 10.

[47] Taghinejad, H.; Taghinejad, M.; Tarasov, A.; Hosseinnia, A.; Moradinejad, H.; Eftekhar, A.; Vogel, E.; Adibi, A. Enhancement of light-2D material interaction envisioned for energy harvesting applications. Conf. Laser Electr, (2017).

[48] R. W. Boyd, Nonlinear Optics, 3rd Edition 2008, 1.

[49] H. Jang, K. P. Dhakal, K. Joo, W. S. Yun, S. M. Shinde, X. Chen, S. M. Jeong, S. W. Lee, Z. Lee, J. Lee, J.-H. Ahn, H. Kim, Adv. Mater. 2018, 30, 1705190.

CHAPTER 7. CONCLUDING REMARKS AND OUTLOOK

My PhD research was designed to open up an entirely new paradigm at the interface of hot-carrier physics and nonlinear optics, and advance the state-of-the-art in the design and implementation of hot-carrier plasmonics for the detection and processing of signals in photonic and quantum systems. We tried to consolidate the relaxation dynamics of hot electrons with externally induced optical nonlinearities to elucidate the generation, transport, and decay of hot carriers in hybrid plasmonic systems. Moreover, we leveraged the ultrafast dynamics of plasmonically induced hot electrons for the ultrafast all-optical control of light and the monitoring of quantum tunneling processes. Over the course of my PhD research, we explored how to best utilize the ultrafast dynamics of hot electrons in plasmonic systems, understand the underlying physics, and provide prototypical demonstrations. Some of the major achievements of my research are listed below:

- We demonstrated that the semi-instantaneous transport of hot electrons from plasmonic metals to electron-accepting materials enhances the third-order nonlinear optical response of metals and at the same time facilitates to significantly shorten the recovery time for the relaxation of optically induced changes to the refractive index of metals.
- By relying on ultrafast dynamics of hot-electron generation and transport we demonstrated sub-picosecond plasmonic switches featuring unprecedented switching performance metrics (e.g., speed, depth, and energy consumption).
- By relying on the discovered dynamics of hot-electron transport and through the design of plasmonic polarizers, we implemented a all-optical ultrafast plasmonic

switch in which the phase and polarization of light are employed as the carriers of information in a data processing platform.

- We demonstrate that the spatially asymmetric transfer of plasmonic hot electrons into an amorphous electron-accepting medium creates an ultrashort timeframe, during which the centrosymmetric host material reveals a nonzero bulk second-order susceptibility, imitating the relaxation behavior of hot electrons in the time domain. This is the first demonstration of optical symmetry breaking with the need for any material phase conversion.
- Besides optical breaking of the inversion symmetry, we showcased the possibility of optical control over the intrinsic $\chi^{(2)}$ response of the second-order nonlinear materials, for the case of monolayer MoS_2.

7.1 Ultrafast All-Optical Switches

As we briefly discussed in Chapter 4, majority of the existing reports on all-optical switching primarily propose optical methods for controlling the "intensity" of light as the primary information-carrying attribute of optical signals. Such a dedicated interest perhaps stems from the ease of managing the reflection, absorption, or transmission of light upon its interaction with optical resonators by optimizing their static and dynamic responses. While relying on the intensity switching circumvents the need for the design of intricate resonance platforms, intensity is not always the best attribute of light to be exploited for data processing, and other attributes such as polarization and phase should be considered as alternatives. For example, as we discussed under **Figure 2**d in the introduction chapter, the optical Kerr and TPA effects in dielectric structures usually work against each other, necessitating the need for increasing the power consumption to obtain a certain modulation

level for the intensity change. However, the phase content of propagating light in photonic structures can be fairly controlled by just harnessing the Kerr coefficient, and in the meantime taking the advantage of the effective propagation length. In fact, a large phase switching ratio at a low power consumption is achievable, independent of the evolution of the light intensity (due to linear or nonlinear loss) as it propagates throughout a photonic medium. In addition, encoding information into the phase and polarization of light increases the accuracy of data retrieval in low noisy environments and facilitates a denser packing of optical information onto optical waves in a multiplexed fashion.

The current portfolio of all-optical modulators lacks an in-depth and systematic investigation on feasible methods that facilitate the ultrafast optical tuning of the phase and polarization of light. The low intrinsic loss in many materials that are adopted in the mainstream of the contemporary photonic technology allows for the expansion of the effective propagation length (L_{eff}) of light, thereby optically inducing a notable phase shift that is proportional to $n_2 I_{co} L_{\text{eff}}$, without the need for significantly increasing the intensity of control light. However, this is often not the case in plasmonic platforms because the absorption loss of conventional materials along with the reduced device footprint substantially shrinks L_{eff}. Instead of relying on an increased interaction length, polarization sensitive structures exhibit promising potentials for the ultrafast control of the phase and polarization in plasmonic systems, as revealed by preliminary demonstrations presented in Chapter 4 and elsewhere, also summarized in Figure 28.(1, 2) Indeed, by the implementation of resonant structures that are exclusively accessible via specific polarization states (Figure 28b,e), only one set of input polarizations are optically modulated and the rest remain intact, leading to the modulation of the overall polarization

state following the interaction of light with the plasmonic structure. In this scenario, by tuning the real and imaginary part of the refractive index, the phase difference between various electric-field components of the input light can be controlled and simultaneously achieve phase and polarization switching (Figure 28c,f). However, since in the proposed methods an intensity-modulation step is the prerequisite for the manipulation of phase and polarization, providing an independent control over various attributes of light is still a major challenge. Exploring innovative modulation techniques that can offer autonomous control over intensity, phase, and polarization of light would be an enticing research direction for the future.

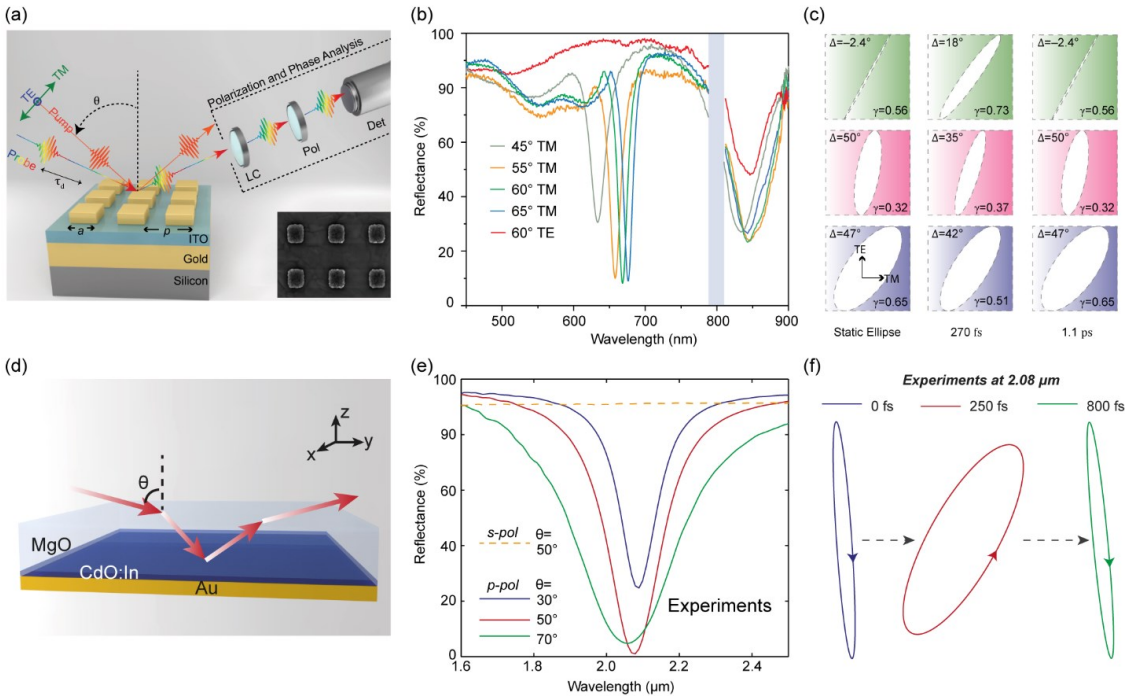

Figure 28: All-optical control of the phase and polarization of light. (a-c) Ultrafast tuning of the state of polarization in the visible spectral range upon the interaction of light with a plasmonic crystal. The polarization sensitivity of the devised structure, shown in panel b, enables all-optical tuning of the phase and polarization of light (panel c) following the generation and transfer of hot electrons, within a sub-picosecond timescale. (d-f) Exploiting ENZ materials for the

implementation of an all-optical reflective polarizer within the near-infrared regime. The giant third-order nonlinearity around the ENZ wavelength of an indium-doped CdO layer allows for the ultrafast modulation of the polarization state upon the reflection of light from the device. Panels (a)-(c) are from reference (1). Panels (d)-(f) are from reference (2). This figure is from a paper that we have published in ACS Photonics (3).

Besides the device-level exploration, a material-level investigation for the discovery of novel active photonic materials seems to be necessary to bridge the existing gap between fundamental science studies and industrial demands in the field of all-optical switching. The importance of the material study becomes more evident once we remember that many existing challenges towards the implementation of applied all-optical switches take roots from the intrinsic properties of active materials. For instance, in most active materials, the vicinity of spectral windows within which the Kerr and TPA effects are strongest, imposes the simultaneous modulation of the intensity and phase, increases the power consumption per modulation events, and increases the required spectral clearance between the adjacent bits of information. In addition, addressing the trade-off issue between the energy consumption and the switching speed is another critical area that optical switches can further benefit from novel active materials. Indeed, utilizing new optical media with large Kerr coefficients releases the need for increasing the Q of resonant structures, and therefore enables a large modulation depth, by consuming a low amount of energy, without constraining the switching speed to the photon lifetime of high-Q resonators. The collection of fascinating physical phenomena to explore and the technological barriers to overcome, will keep the field of all-optical switches at hot frontiers of nanophotonics in the years to come with the hope for implementing on-chip, all-optical data processors.

7.2 Coherent Control of Second-Order Optical Nonlinearities

As we discussed throughout Chapter 5 and Chapter 6 this thesis, optical nonlinearities of second-order type play major roles in various frontiers of active and ultrafast photonics. For instance, majority of tunable coherent light sources rely of sum/difference frequency generation, optical parametric amplification, and optical rectification of available light sources in the market. However, not every important optical material (e.g., silicon) has the advantage of having a noncentrosymmetric crystal structure, therefore, all the fascinating functionalities described above should be demonstrated by only relying on a limited number of optical materials. Such a fundamental constraint reveals the importance of discovering reliable techniques, particularly optical ones, for inducing $\chi^{(2)}$-based responses in, arguably, any material of interest, despite of its crystal symmetry. The proposed technique in Chapter 5 of this PhD thesis, indeed offers an initial, yet promising optical approach for breaking the inversion symmetry in a wide range of optical materials, even if the material of choice is transparent and not capable of linearly interacting with light. In our proposed technique, the only requirement to be satisfied is to find an appropriate pair of metal/dielectric material that support the interfacial charge transport upon the illumination of an optical control signal. The proposed technique in this thesis not only introduces an optical method for breaking the crystal symmetry, but also offers a time-dependent induced $\chi^{(2)}$ response. The transient nature of hot-electron induced $\chi^{(2)}$ adds an element of time dependency to second-order nonlinear optical processes, and therefore, enables a unique opportunity for ultrafast optical data processing.

Besides the importance of the proposed technique for nonlinear frequency mixing, our hot-electron symmetry breaking method could find valuable application in studying the carrier dynamics, exploring quantum transport, and tunneling of charge carriers at surfaces

and interfaces of a wide range of materials. In other words, the induced nonlinear effect (e.i., emitted SHG signal in the presented case in Chapter 5) can be considered as a nonlinear optical probe to characterize the dynamics of electron transport in hybrid material systems. Although NIR linear measurements have been traditionally employed for such purposes, employing a nonlinear optical probe provides unprecedented capabilities. When a NIR beam probes a hybrid plasmonic metal/dielectric material system, not only does it monitor the carrier transport, but its results are also blended with features from the dynamics of intraband transitions inside the metal. Consequently, this technique fails to distinguish such parallel transient processes. However, to address this long-standing issue in hot-electron physics and unambiguously quantify the dynamics of plasmonically-induced hot carriers, a viable solution would be to look at the dynamics of the induced SHG signal. Considering that the emitted SHG signal primarily stems from the transport of hot electrons, independent of the inra-material transient processes, dynamics of this second-order nonlinear process would provide a clean and unique way studying transport kinetic.

7.3 High-Speed Hybrid Opto-Electronic I/O Units

The ever-increasing demand for bandwidth scalability and high-speed operation is the driving force for the discovery of ultrafast switches. As electronics approaches its intrinsic limitations, pursuing new computational schemes seems to be inevitable to comply with the increasing demand for bandwidth scalability in data processing units. In recent years, there has been a great surge of research to discover new methods for implementing high-speed electronic components and such a need has pushed scientists to explore fundamentally new classes of electronic switches that do not suffer from the

conventional capacitive limitations on the switching speed. In a recent discovery, an on-chip nanoplasma electronic switch has been proposed that is capable of picosecond switching of electric signals with a broad range of electric power.(4) In addition, recently optical computing –replacing electrons with photons– has been introduced as a powerful alternative to boost computational skills beyond that of solid-state electronics. Up to date, however, the primary role of optical technologies in data processors is limited to the realization of communication links through the incorporation of optical fibers and, more recently, photonic waveguides between electronic blocks. To extend the role of optics beyond being a convenient pipe for ultrafast data transmission, it is essential to implement CMOS integrable optical switches. This goal is achievable through nonlinear optical effects; Indeed, by enabling active modulation of light waves and on-demand generation of new spectral components, nonlinear optics potentially has the capability to deliver advanced optical I/O segments to realize an all-optical computer. Although “speed” is the biggest promise of optics, relying on electronic components to control light sources at I/O end facets is the major setback towards unlocking the ultimate potential of optical data processors. We believe that hot carrier electronics could have a strong impact on the future developments of high-speed opto-electronic I/O units. This belief stems from the fact that the generation/transport of hot (energetic) electrons are the natural products of light-matter interaction in plasmonics and occur inherently ultrafast (i.e., shorter than a few hundreds of femtoseconds). Therefore, employing electrically enabled plasmonic platforms allows for the conversion of injected hot carrier to electrical signals, enjoying the sub-picosecond creation of electric pulses independent of the capacitive response of the device. Therefore, exploring feasible methods for the implementation of hot-carrier based hybrid opto-

electronic switches would a fascinating future research direction that will have far reaching technological benefit in a long perspective.

7.4 References

1. Taghinejad, M.; Taghinejad, H.; Xu, Z.; Lee, K. T.; Rodrigues, S. P.; Yan, J. H.; Adibi, A.; Lian, T.; Cai, W. Ultrafast control of phase and polarization of light expedited by hot-electron transfer. Nano Lett. 2018, 18, 5544-5551.

2. Yang, Y. M.; Kelley, K.; Sachet, E.; Campione, S.; Luk, T. S.; Maria, J. P.; Sinclair, M. B.; Brener, I. Femtosecond optical polarization switching using a cadmium oxide-based perfect absorber. Nat. Photonics 2017, 11, 390-396.

3. M. Taghinejad, W. Cai, All-optical control of light in micro- and nanophotonics. *ACS Photonics* **6**, 1082-1093 (2019).

4. M. S. Nikoo, A. Jafari, N. Perera, M. Zhu, G. Santoruvo, E. Matioli, anoplasma-enabled picosecond switches for ultrafast electronics. *Nature* **580**, E8(2020). https://doi.org/10.1038/s41586-020-2118-y.